AD-A237 536

PL-TR-91-2084

PHASE SCREEN SIMULATIONS OF SEISMIC WAVE SCATTERING
RELATED TO MONITORING UNDERGROUND NUCLEAR EXPLOSIONS

M. D. Fisk
G. D. McCartor
W. R. Wortman

Mission Research Corporation
P. O. Drawer 719
Santa Barbara, CA 93102-0719

23 April 1991

Final Report
23 February 1989–23 April 1991

APPROVED FOR PUBLIC RELEASE; DISTRIBUTION UNLIMITED

PHILLIPS LABORATORY
AIR FORCE SYSTEMS COMMAND
HANSCOM AIR FORCE BASE, MASSACHUSETTS 01731-5000
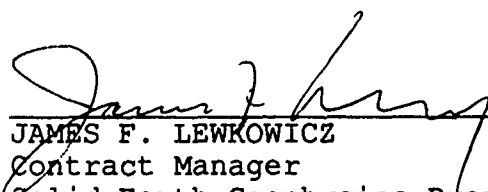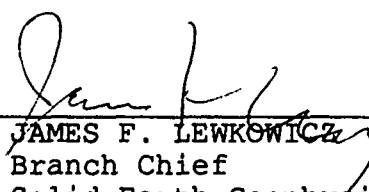
91 7 02 020

91-03934

This technical report has been reviewed and is approved for publication.

_____   _____
JAMES F. LEWKOWICZ   JAMES F. LEWKOWICZ
Contract Manager   Branch Chief
Solid Earth Geophysics Branch   Solid Earth Geophysics Branch
Earth Sciences Division   Earth Sciences Division

_____
DONALD H. ECKHARDT, Director
Earth Sciences Division

REPORT DOCUMENTATION PAGE

Public reporting burden for this collection of information is estimated to average 1 hour per response, including the time for reviewing instructions, searching existing data sources, gathering and maintaining the data needed, and completing and reviewing the collection of information. Send comments regarding this burden estimate or any other aspect of the collection of information, including suggestions for reducing this burden, to Washington Headquarters Services, Directorate for Information Operations and Reports, 1215 Jefferson Davis Highway, Suite 1204, Arlington, VA 22202-4302, and to the Office of Management and Budget, Paperwork Reduction Project (0704-0188), Washington, DC 20503.

1. AGENCY USE ONLY *(Leave blank)*	2. REPORT DATE 910423	3. REPORT TYPE AND DATES COVERED Final 890223 – 910423

4. TITLE AND SUBTITLE Phase Screen Simulations of Seismic Wave Scattering Related to Monitoring Underground Nuclear Explosions	5. FUNDING NUMBERS PE 62714E PR 9A10 TADA WUBE Contract F19628-89-C-0040
6. AUTHOR(s) M.D. Fisk, G.D. McCartor* and W.R. Wortman	

7. PERFORMING ORGANIZATION NAME(S) AND ADDRESS(ES) Mission Research Corporation P.O. Drawer 719 Santa Barbara, CA 93102-0719	8. PERFORMING ORGANIZATION REPORT NUMBER MRC-R-1357

9. SPONSORING/MONITORING AGENCY NAME(S) AND ADDRESS(ES) Phillips Laboratory Hanscom Air Force Base Massachusetts 01731-5000 Contract Manager: James Lewkowicz/LWH	10. SPONSORING/MONITORING AGENCY REPORT NUMBER PL-TR-91-2084

11. SUPPLEMENTARY NOTES
*Southern Methodist University, Dallas, TX.

12a. DISTRIBUTION/AVAILABILITY STATEMENT Approved for Public Release; Distribution Unlimited.	12b. DISTRIBUTION CODE

13. ABSTRACT *(Maximum 200 words)*

The objective of this project was to investigate seismic wave scattering effects, and to assess the existence and impact of mild nonlinear contributions to the attenuation of seismic signals, for purposes of monitoring underground nuclear explosions. We developed an efficient propagation algorithm, and applied it to the problems of understanding conversion of regional phases, coherence of waveforms measured by seismic arrays, and the accuracy of direct versus scattered phases. Experiments related to mild nonlinear attenuation were also reviewed. This final report consists of preprints of three papers which will be submitted for open publication.

In the first paper, the accuracy and efficiency of the phase screen method for elastic waves are assessed by comparing with finite difference calculations of elastic wave propagation in 2-D random media. The phase screen method is a forward propagation algorithm which depends only on the local S and P wave velocities. Both methods are used to generate synthetic seismograms for a suite of 2-D random media characterized by exponential and von Karman (self-similar) autocorrelation functions of varying strength and correlation length.

14. SUBJECT TERMS Phase Screen Method Random Media Transmission Fluctuations Seismic Wave Scattering		15. NUMBER OF PAGES 144
		16. PRICE CODE

17. Security CLASSIFICATION OF REPORT UNCLASSIFIED	18. Security CLASSIFICATION OF THIS PAGE UNCLASSIFIED	19. Security CLASSIFICATION OF ABSTRACT UNCLASSIFIED	20. LIMITATION OF ABSTRACT SAR

CLASSIFIED BY:

DECLASSIFY ON:

13.   ABSTRACT (continued)

Constant and varying Poisson ratio are considered. The results compare quite favorably. Execution times are compared for simulations on a SUN 4/330, an ELXSI 6400, a CRAY-2, and an nCUBE parallel computer. The phase screen algorithm is roughly two orders of magnitude faster than the finite difference algorithm for 2-D problems. A naive estimate, suggests that the phase screen method may be three orders of magnitude faster for 3-D problems.

In the second paper, phase screen simulations of vector wave propagation in elastic random media are applied to two studies relevant to monitoring underground nuclear explosions. The first study concerns the analysis of transmission fluctuations of incident P waves propagated through a two-dimensional version of Flatté and Wu's two-layer model of the crust and upper mantle under NORSAR. Simulated coherence functions for vector waves are compared to analytic and simulated results based on the parabolic approximation to the scalar wave equation; the analytic results also assume the Rytov approximation. We demonstrate the usefulness of the phase screen simulations for analyzing moderately strong scattering and three-component data. In the second study, we investigate the effect of random structure on the variances of the direct peak-to-peak P wave amplitude, and the rms amplitude of the transverse component in the velocity window between the P and S wave speeds. This study shows that the relative variance of the scattered phase is far less dependent on the structure than the direct phase. The variance of the forward scattered P wave depends greatly on the strength of the large-scale heterogeneities.

In the third paper, experiments which reflect the attenuation of propagating pulses in salt in the moderate strain regime of 10^{-3} to 10^{-6}, corresponding to ranges of 100 to 10,000 meters from an explosion with yield of 1-kt, are reviewed. A transition from nonlinear to linear behavior occurs in this interval. This regime is important for monitoring of nuclear test treaties since models for linear source functions are normally defined inside it. Salt is of interest since it can be readily mined to produced decoupling cavities. Data from explosive sources, nuclear and chemical field and small scale laboratory tests, resonant bars and ultrasonic pulse methods are summarized. The experiments are diverse in their character and frequency and no single experiment covers the nonlinear-linear transition. However, the totality suggests that attenuation in salt does decrease dramatically over the moderate strain regime. A full physical description does not exist although shear failure or yielding can account for some effects.

Table of Contents

Bibliography of Publications Sponsored by Contract

In addition to the papers contained in this report, the following published papers have been sponsored by this contract:

Fisk, M. D., and G. D. McCartor, "The Phase-Screen Method for Elastic Waves and Seismic Discrimination", GL-TR-89-0330, ADA220771, Mission Research Corp., 1989.

Fisk, M. D., and G. D. McCartor, "A Phase-Screen Method for Elastic Waves". *Papers presented at the 12th Annual DARPA/AFGL Seismic Res. Symp.*, 35–41, 1990.

Fisk, M. D., and G. D. McCartor, "Applications of the Phase-Screen Method for Elastic Waves". *Papers presented at the 12th Annual DARPA/AFGL Seismic Res. Symp.*, 42–48, 1990.

Fisk, M. D., and G. D. McCartor, The phase-screen method for vector elastic waves, *J. Geophys. Res.*, 96, 5985–6010, 1991.

McCartor, G. D., and W. R. Wortman, "Nonlinear attenuation in Salt at Moderate Strain". *Papers presented at the 11th Annual DARPA/AFGL Seismic Res. Symp.*, 356–363, 1989.

A COMPARISON OF PHASE SCREEN AND FINITE DIFFERENCE METHODS FOR ELASTIC WAVES IN RANDOM MEDIA

M. D. Fisk
Mission Research Corporation
Santa Barbara, California 93102

E. E. Charrette
nCUBE Corporation, Geophysical Center for Parallel Processing
Earth Resources Laboratory
Department of Earth, Atmospheric,and Planetary Sciences
Massachusetts Institute of Technology, Cambridge, MA 02139

G. D. McCartor
Department of Physics
Southern Methodist University
Dallas, TX 75275-0175

Abstract

Phase screen calculations of elastic wave propagation in 2-D random media are compared with finite difference results to assess the accuracy and efficiency of the former method. The phase screen method is a forward propagation algorithm which depends only on the local S and P wave velocities. It differs from similar methods for scalar waves by treating P/S conversion. Both methods are used to generate synthetic seismograms at 640 evenly spaced gridpoints for identical realizations of 512×2750 grids. Comparisons are made for a suite of 2-D random media characterized by exponential and zeroth order von Karman (self-similar) autocorrelation functions of varying strength and correlation length. Constant and varying Poisson ratio are considered. Early arrivals compare more favorably since the phase screen method does not include backscatter. The waveforms are compared by computing relative differences and cross correlations as a function of time offset. Temporal energy centroids of bandpass filtered synthetic seismograms are also computed. Execution times are compared for simulations on a SUN 4/330, an ELXSI 6400, a CRAY-2, and an nCUBE parallel computer. The phase screen algorithm is roughly two orders of magnitude faster than the finite difference algorithm for 2-D grids. A naive estimate, based on the number of operations in each algorithm, suggests that the phase screen method may be three orders of magnitude faster for 3-D problems.

1

1. INTRODUCTION

The purpose of this study was to assess the accuracy and relative speed of a multiple phase screen method for propagating elastic waves in highly heterogeneous media. The complexity of such media makes analytic solutions infeasible. Thus we have no choice but to compare the phase screen calculations to some other form of modeled data. For this comparison, we chose to use synthetic data calculated via the finite difference method.

The finite difference technique is attractive because it produces a full solution to the elastic wave equation. Thus all direct, converted, diffracted and guided waves are accurately modeled. Unlike various high frequency approximations, there is no limitation in principle on the ratio of scatterer size to wavelength. Also, synthetic seismograms may be generated at any point on a discretized grid. The method is limited however by the speed of the computer, the memory available and the cost of CPU time. With very few exceptions, the published studies based on this method have been performed for 2-D media (Frankel, 1989).

The phase screen method, developed by Fisk and McCartor (1989,1991), is an algorithm to rapidly forward propagate vector elastic waves. Phase screen methods for scalar waves have been used in previous propagation studies of starlight through the atmosphere (Ratcliffe, 1956; Mercier, 1962; Filice, 1984), radio signals through the ionosphere (Buckley, 1975; Bramley, 1977; Knepp, 1983), acoustic waves in the ocean (Flatté; 1979), and P waves in the earth (Haddon and Husebye, 1978). Simulations for scalar waves in three dimensions have been performed by Filice (1984) and Martin and Flatté (1988). The method used here treats both S and P waves, including their conversion, and allows for simulation of seismic wave propagation in 3-D heterogeneous media. Like the finite difference method, this method may be used to generate synthetic seismograms at any gridpoint.

The phase screen method may be applied to media described by a mixture of deterministic and stochastic structure. In a previous study, Fisk and McCartor (1991) compared the results of the phase screen method with an "exact solution" of an elastic wave in a 2-D laterally-layered structure. (By "exact" we mean that there were no fundamental approximations made to solve the equation of motion and satisfy the boundary conditions. The solution cannot be written in closed form, however, but may be numerically determined to any desired precision.) Even for wavelengths on the order of the length scale of the layers and velocity variations of 5%, the comparison was excellent.

2

Common to ray theory methods (e.g., Karal and Keller, 1959; Aki and Richards, p. 90, 1980; Ansell, 1981), the phase screen method makes use of the following facts: (1) To first order at high frequency the P and S wave displacements, expressed as the curl-free and divergence-free portions of the total displacement respectively, decouple; and (2) to first order the propagation of the waves depend only on the local P and S wave velocities, which act to distort the wavefronts. For applicable problems, the heterogeneous medium depicted in figure 1(a) may be replaced with a homogeneous medium and a set of phase screens, as shown in figure 1(b). Based on the first fact, the initial P and S waves at $z = 0$ are independently propagated to $z = \Delta z$ according to the uniform elastodynamic equation, using the average wave velocities. The affect of variations in the local velocities is treated by multiplying the S and P waves by position dependent phase factors at screen 2. In general, the distorted wavefronts no longer satisfy the curl-free and divergence-free conditions. Hence, if these waves are decomposed onto a complete set of forward propagating P and S plane waves that do satisfy these conditions, P/S conversion is obtained. The procedure may now be repeated, inserting phase screens for larger values of z, to propagate the displacement further.

The spacing of the screens is determined such that geometric optics applies for propagation between them. Martin and Flatté (1988) have pointed out that diffraction effects are accumulated from propagation through many screens. By including diffraction effects, as Hudson (1980) has noted, the results are valid to a much greater range than those of simple ray theory. The phase screen method is limited, however, to particular scattering strengths and length scales of the structure for a given wavelength. Thus this method does not have the versatility of the finite difference method. We believe, however, that it may be used to treat a significant range of problems in seismology that finite difference currently cannot due to CPU time considerations.

Conversion, as Levin and Rytov (1957) have noted, is a second order effect at high frequency, and is treated as such in the phase screen method. Karal and Keller (1959), Richards (1974) and Ansell (1981) have also pointed out that there are second order contributions to the P and S wave displacements that are not purely longitudinal and transverse motion. These terms depend on spatial derivatives of the density and the Lamé constants. Thus treating P/S conversion while ignoring these contributions is not entirely consistent to second order. We have found, by comparison with exact solutions for the laterally-layered problem with constant Poisson ratio, that the results are considerably more accurate by treating conversion in this manner than ignoring it altogether. Efforts to improve the P and S wave decomposition are currently being made.

3

Aside from treating both P and S waves in our analysis, our method differs from previous phase screen methods used in seismology by treating wide-angle scatter. Although wide-angle scatter has been treated before in the context of phase screen methods for acoustic waves (Thomson and Chapman, 1983), and for light waves (Feit and Fleck, 1978), the typical starting point in the formulation of the method is to assume the parabolic approximation which treats only small-angle scatter. This approximation is valid for either scalar or vector waves provided the wavelength is much smaller than the structure size. In a previous study, Fisk and McCartor (1991) found that the treatment of wide-angle scatter allows for propagation in smaller structures to be computed more accurately. Certainly larger structures will lead to better results since waves propagating at large oblique angles are apt to induce backscattering. For large enough structures, our expressions may be expanded to recover the standard parabolic approximation.

A study by McLaughlin and Anderson (1987) has shown that methods that do not include wide-angle scattering and conversion, such as simple ray theory, Rytov theory of a forward propagating scalar wave, and Gaussian beam synthesis, are incapable of modelling systematic delays of high frequencies (4-5 Hz) relative to lower frequencies (1-2 Hz) as has been observed at NORSAR in P-waves from Eastern Kazakh explosions. They referred to this effect as "stochastic dispersion" of the P-wave, and quantified the time delay by computing the temporal energy centroids of bandpass filtered seismograms. They found that of the methods they studied, only finite difference calculations for media with multiple length scales were able to reproduce this effect. We computed the temporal energy centroids of bandpass filtered finite difference and phase screen synthetics to determine the affects of including multiple wide-angle scattering, but neglecting backscatter, in the phase screen method.

The remainder of the paper is organized as follows. Section 2 provides descriptions of the two algorithms used. Execution times are compared for simulations on a SUN 4/330, an ELXSI 6400, a CRAY-2, and an nCUBE parallel computer. Due to CPU time considerations, the finite difference simulations were only performed on the last two computers. Section 3 contains the details of modeling the random fluctuations. To directly compare the results of the two methods, identical realizations of the random fluctuations were used by both routines. Section 4 contains comparisons of the results. Synthetics were computed at 640 evenly distributed points. We investigate how the accuracy of the phase screen method depends on the autocorrelation function, the magnitude of the velocity fluctuations, the correlation length of the medium, and whether the medium was described by constant or varying Poisson ratio. We compute the cross correlations of the time series and relative differences of the waveforms for each component, and average over the receivers in the x-direction.

4

We also compare the temporal energy centroids of the vertical component waveforms. In section 5 we draw some conclusions about the applicability and usefulness of the phase screen method. Appendix A contains detailed formulas of the phase screen method for vector elastic waves, and Appendix B addresses the accuracy of the finite difference method.

2. NUMERICAL ALGORITHMS

Finite Difference Method

The equation of motion for the displacement vector u in a heterogeneous linear source-free medium is

$$\rho(\mathbf{x})\frac{\partial^2 u_i}{\partial t^2} = \frac{\partial}{\partial x_j}\left[\lambda(\mathbf{x})(\nabla \cdot \mathbf{u})\delta_{ij} + \mu(\mathbf{x})\left(\frac{\partial u_i}{\partial x_j} + \frac{\partial u_j}{\partial x_i}\right)\right] \tag{1}$$

where $\lambda(\mathbf{x})$ and $\mu(\mathbf{x})$ are the Lamé constants, and $\rho(\mathbf{x})$ is the density. For propagation in a two dimensions, the equations of motion for the horizontal (u) and vertical (v) particle displacements are

$$\rho\frac{\partial^2 u}{\partial t^2} = \frac{\partial}{\partial x}\left[(\lambda + 2\mu)\frac{\partial u}{\partial x} + \lambda\frac{\partial v}{\partial z}\right] + \frac{\partial}{\partial z}\left[\mu(\frac{\partial u}{\partial z} + \frac{\partial v}{\partial x})\right] \tag{2}$$

$$\rho\frac{\partial^2 v}{\partial t^2} = \frac{\partial}{\partial x}\left[\mu(\frac{\partial u}{\partial z} + \frac{\partial v}{\partial x})\right] + \frac{\partial}{\partial z}\left[(\lambda + 2\mu)\frac{\partial v}{\partial z} + \lambda\frac{\partial u}{\partial x}\right]. \tag{3}$$

Throughout this work, we have assumed a two dimensional cartesian geometry, and that density is constant throughout the medium. In addition, we have assumed the medium is horizontally periodic and bounded by absorbing boundaries in the vertical direction. (The latter boundary condition is irrelevant to the phase screen method, since backscatter is ignored.) The finite difference method solves these coupled differential equations numerically by replacing the partial derivatives in space and time by finite-difference approximations. The parameters λ, μ, ρ, and the components of the wavefield become functions of discrete 2-D cartesian coordinates.

Various finite difference approximations have been used to solve the wave equation (e.g., Boore, 1972; Alford, 1974; Kelly et al., 1976; Virieux, 1986; Fornberg, 1987; Witte, 1989). For this work, we have made use of the simple explicit second-order scheme proposed by Kelly et al. (1976). Second-order schemes are preferred in

5

highly heterogeneous media since they more accurately resolve rapid variations in the wavefield and the medium (e.g., Fornberg, 1987; Daudt, 1989; Charrette, 1991). Also, we favored a non-staggered formulation because it is easier to implement the second-order absorbing boundary conditions proposed by Clayton and Engquist (1977).

Phase Screen Method

The linearity of eq. (1) allows the solution to be written in terms of P and S wave displacements as $u = u_P + u_S$, which are chosen to satisfy the constraints $\nabla \times u_P = 0$ and $\nabla \cdot u_S = 0$. To first order at high frequency this decomposition results in the decoupling of the equation of motion into two simple wave equations of the form

$$\left(\nabla^2 + \frac{w^2}{\alpha(\mathbf{x})^2}\right) u_P = 0, \qquad \left(\nabla^2 + \frac{w^2}{\beta(\mathbf{x})^2}\right) u_S = 0, \tag{4}$$

where a time dependence of e^{-iwt} is assumed for now. The local propagation velocities for the respective waves are given in terms of the density and Lamé constants by $\alpha(\mathbf{x}) = \sqrt{(\lambda(\mathbf{x}) + 2\mu(\mathbf{x}))/\rho(\mathbf{x})}$ and $\beta(\mathbf{x}) = \sqrt{\mu(\mathbf{x})/\rho(\mathbf{x})}$.

The phase screen algorithm for vector waves may be summarized as follows. (A more detailed discussion is provided in Appendix A.) Given a realization of the 2-D grid, it is divided into equal intervals of length Δz by planes of constant z. Starting with the initial displacement, u_P and u_S are uniformly and independently propagated to a distance Δz. The affect of the velocity perturbations is treated by multiplying the S and P waves by position dependent phase factors, $\exp(i\Delta^{(P)})$ and $\exp(i\Delta^{(S)})$. The P-wave phase factor for the perturbations between $z = 0$ and $z = \Delta z$ is given by the geometrical optics expression

$$\Delta^{(P)}(x, \Delta z) = k_P \int_0^{\Delta z} dz \, \frac{\delta\alpha(x, z)}{\bar{\alpha}}, \tag{5}$$

where $k_P = w/\bar{\alpha}$, $\bar{\alpha}$ is the average P wave velocity, and $\delta\alpha$ is the velocity perturbation. There is an analogous expression for the S-wave phase factor. Similar expressions are computed for the fluctuations between the other screens.

The wavefronts, distorted by the phases, no longer satisfy the curl-free and divergence-free conditions. Using standard Fourier and vector analysis, these waves are decomposed onto a complete set of forward propagating P and S plane waves that do satisfy these conditions. The procedure is repeated, inserting phase screens

6

for larger values of z, to propagate the displacement further. Synthetic seismograms are produced by computing the single-frequency results at a discrete set of positive frequencies. Using an FFT, the product of single-frequency results and the Fourier spectrum of the time source function is transformed to the time domain. The real part of the transformed expression is then taken.

3. CONSTRUCTING RANDOM VELOCITY PERTURBATIONS

The autocorrelation function is commonly used to characterize random fields and is a measure for quantifying the similarity between neighboring points in a random medium. It has the property that it is the Fourier transform of the power spectrum (Tatarski, 1961). This relationship allows us to build realizations from a desired correlation function in the wavenumber domain. Throughout this study, realizations were constructed by convolving the square root of the power spectrum with a phase term of the form $e^{i\theta}$, where θ is a random number drawn from a uniform distribution over the range $0 \leq \theta < 2\pi$. Since the norm of the phase term is one, the shape of the power spectrum and the total power within that spectrum are unchanged.

Three correlation functions have received a great deal of attention in the scattering literature; the Gaussian, the exponential and the von Karman functions (e.g. Chernov, 1960; Tatarski, 1961; Dainty, 1984; Frankel and Clayton, 1986; Wu and Aki, 1990). The commonly used form of these functions and their power spectra are given in Table 1, and shown graphically in Figure 2.

In the exponential function, the correlation length a marks the lag where the correlation function has the value e^{-1} (Figure 2). In the wavenumber domain, both spectra are flat out to a corner wavenumber which is approximately equal to $1/a$. At higher wavenumbers, the exponential falls off as $k^{-(N+1)}$, where N is the number of space dimensions. The fall off rate of the spectra controls the amount of roughness in the realization. Spectra with more energy at high wavenumbers are expected to show more roughness (Figure 3) than those which are localized near zero wavenumber.

The von Karman function was first introduced to characterize the random velocity field of a turbulent medium (von Karman, 1948). In the spatial domain, the von Karman function is peaked about the origin. The peak is especially severe when $\nu = 0$, since then the modified Bessel function K_ν goes to infinity as r/a goes to zero. Although the parameter ν can take on any value in the range 0 to 1, it has some special properties at 0, 0.3, 0.5 and 1. When $\nu = 0$ the spectrum defines a multi-dimensional Markov field (Goff, 1988), $\nu = 0.3$ defines Kolmogorov's turbulence (Wu and Aki, 1990), while for $\nu = 0.5$ the von Karman function simplifies to an exponential and when $\nu = 1.0$ to an autoregressive field.

7

Table 1.   Correlation Functions and Power Spectra.

	Gaussian	Exponential	von Karman
Correlation Function	e^{-r^2/a^2}	$e^{-r/a}$	$\frac{1}{2^{\nu-1}\Gamma(\nu)}\left[\frac{r}{a}\right]^\nu K_\nu(r/a)$
1-D Power Spectrum	$a\sqrt{\pi}e^{-k_r^2 a^2/4}$	$\frac{2a}{1+k_r^2 a^2}$	$\frac{\Gamma(\nu+1/2)}{\Gamma(\nu)}\frac{2\pi^{1/2}a}{\left(1+k_r^2 a^2\right)^{\nu+1/2}}$
2-D Power Spectrum	$\frac{a^2}{2}e^{-k_r^2 a^2/4}$	$\frac{a^2}{(1+k_r^2 a^2)^{3/2}}$	$\frac{\Gamma(\nu+1)}{\Gamma(\nu)}\frac{4\pi a^2}{\left(1+k_r^2 a^2\right)^{\nu+1}}$
3-D Power Spectrum	$(a\sqrt{\pi})^3 e^{-k_r^2 a^2/4}$	$\frac{8\pi a^3}{(1+k_r^2 a^2)^2}$	$\frac{\Gamma(\nu+3/2)}{\Gamma(\nu)}\frac{8\pi^{3/2}a^3}{\left(1+k_r^2 a^2\right)^{\nu+3/2}}$

The peakedness of the von Karman correlation function leads to a wide spectral representation, indicating that these media contain a significant amount of roughness (Figure 4). As in the exponential function, the power spectrum of the von Karman function is flat up to a corner wavenumber roughly equal to $1/a$. The difference is that at higher wavenumbers the spectrum falls off as $k^{-(N+2\nu)}$, considerably slower than the exponential function. Thus for both functions, $1/a$ defines a corner wavenumber and the parameter ν controls the rate of decay of the power spectrum (Figure 2).

The von Karman function has an additional property that its slope is discontinuous at zero lag. This property qualifies the von Karman function as a fractal (Mandelbrot, 1977). Fractals are unique and of interest because they contain variations on all wavelengths. Since many physical characteristics in the crust also display variation on a wide variety of length scales, this autocorrelation function may be well suited to crustal applications. The self-similar nature of fractals can be easily seen by examining the variance as a function of wavenumber. Figure 5 shows a series of 1-D realizations taken from the three *ACFs* described above. All three realizations have the same correlation length ($a = 20$ m) and were generated by the same random seed. At low wavenumbers there is little variation in shape and variance between the

traces. This is consistent with the power spectra (Figure 2), which are flat at low wavenumber for all three functions. At high wavenumbers, there is no variance in the Gaussian trace, and the variance in the exponential trace is smaller than it was at low wavenumber. Thus, for these media, the variance over equal logarithmic intervals of wavelength decreases as the wavelength decreases (Frankel, 1989). This is not so for the 0th order von Karman function. The variance for that function is roughly constant over length scales smaller than $2\pi a$ (Figure 5).

3. COMPARISONS

Details of the Models

Since the most important differences between the finite difference and phase screen solutions were expected late in the wavetrain, it was necessary to simulate wave propagation over a large enough region that the scattered field could include a considerable amount of forward and backscattered energy. This requirement led to the use of a relatively large grid (512 nodes by 2750 nodes). A schematic of the grid is shown in Figure 6. The spacing between the gridpoints was $dx = dz = 0.05$ km. The lowest 250 gridpoints in the z-direction were homogeneous to allow for the pulse to be "initialized" in the finite difference code. The spatial form of the source was a plane P-wave located initially at a depth of 127.5 km within the homogeneous segment. Arrays of 64 receivers were located every 250 gridpoints in the z-direction. The phase screens were uniformly spaced every 50 gridpoints in the z-direction for the heterogeneous portion of the grid.

The initial time source function used in our study was a Ricker wavelet defined by

$$F(t) = \left(1 - (2\pi f_0(t - t_0))^2/2\right) \exp\left(-(2\pi f_0(t - t_0))^2/4\right), \qquad (6)$$

where f_0 is the peak frequency and t_0 defines the origin of time. The value $f_0 = 2$ Hz was used for all of the simulations. The finite difference simulations used 10000 timesteps, however, only 1500 of these points were included in the output. The same timestep $\Delta t = 0.025$s was used for the phase screen method, however, only 256 frequencies were sampled; the remaining frequency data were zero padded to minimize wrap-around effects.

Table 2 lists the details of the models, which were chosen to explore how the accuracy depends on the correlation function, the wavelength to correlation length ratio, and the magnitude of the velocity perturbations. A constant Poisson ratio

9

was assumed for the first four models. The last four models assumed λ constant; thus the Poisson ratio was allowed to vary over the grid. The average velocities used throughout this study were $\bar{\alpha} = 5.5$ km/s and $\bar{\beta} = \bar{\alpha}/\sqrt{3}$. Correlation lengths of 5 km and 2 km were used. The combination ka, relevant to the scattering regime (Wu, 1990), is given in Table 2, where k is used here to denote the P-wave wavenumber at peak frequency. Although the phase screen method is expected to provide the most favorable results for media with only density fluctuations, we chose to consider only variations in the Lamé constants to avoid making significant alterations in the finite difference program.

Table 2. List of Models.

Model	ACF	$(\delta\alpha/\alpha)_{rms}$	$(\delta\beta/\beta)_{rms}$	ka
1	Exponential	2.0%	2.0%	11.4
2	Self-Similar	2.0%	2.0%	11.4
3	Exponential	5.0%	5.0%	11.4
4	Self-Similar	5.0%	5.0%	11.4
5	Self-Similar	1.3%	2.0%	11.4
6	Self-Similar	1.3%	2.0%	4.6
7	Self-Similar	3.3%	5.0%	11.4
8	Self-Similar	3.3%	5.0%	4.6

Comparison of Execution Time

Although the finite difference program had to be modified to use the nCUBE parallel computer, the reduced execution time more than compensated for the conversion of the code. To take advantage of the independent processors on the nCUBE, the large finite difference grid was split into a series of separate subgrids, each residing on a separate nCUBE processor. At each timestep, the independent subgrids were solved simultaneously, the data along the edges are exchanged and the process is repeated. For reference, a finite difference simulation like those presented here would take more than 12 days to complete on a fully dedicated workstation (SUN 4/330). The same problem could be run on a traditional supercomputer (CRAY-2) in 3.2 hrs. On a 128-node nCUBE parallel computer the simulation took only 1.8 hrs. to run, and on a 1024-node nCUBE parallel computer the run time was less than 1/2 hour.

10

Originally the phase screen code was developed on an ELXSI 6400. This version was run on the ELXSI 6400, SUN 4/330, and CRAY-2. To exploit the independent processors on the nCUBE, minor modifications were made to distribute the single-frequency calculations among the processors. Table 3 lists the run times for the phase screen simulations. The relative execution speeds of the phase screen and finite difference simulations are roughly factors of 125 for the SUN 4/330, 52 for the CRAY-2, and 63 for the 128-node nCUBE parallel computer. (The phase screen code was not run on the 1024-node nCUBE machine.) A naive estimate of the relative speed, based on the number of operations in each algorithm, suggests that the phase screen method may be roughly three orders of magnitude faster for 3-D problems. Further efforts to optimize the phase screen code on a particular machine would likely lead to even more significant reductions in run times. Martin and Flatté (1988) have shown that vectorizing a phase screen algorithm for scalar waves to run on a CRAY led to a speedup factor of nearly 800 as compared with the run time on a VAX-11/750.

Table 3.   Execution Times For The Phase Screen Method.

Machine	Number of Processors							
	1	2	4	8	16	32	64	128
SUN 4/330	8254 s							
ELXSI 6400	1771 s							
CRAY-2	223 s							
nCUBE	7964 s	3954 s	1997 s	1002 s	510 s	288 s	166 s	103 s

Comparison of Synthetics

Synthetic seismograms for the eight models are recorded for receivers located at the midpoint in the x-direction, and for various depths (Figures 7-14). Figures 15-22 show comparisons of the synthetics at every sixteenth receiver at a depth of $z = 12.5$ km ($NZ = 251$). (This array of receivers was chosen since the absorbing boundary condition at $z = 0$ only partially absorbs obliquely incident waves (cf. Appendix B). Spurious reflected signals are expected to propagate backward into the grid in the finite difference solution, however, they should have smaller amplitudes than the spurious signals directly at the boundary.) In all of these figures the solid and dotted curves represent the finite difference and phase screen results, respectively. It is immediately apparent that there is excellent agreement between the waveforms at early times, which is degraded at later times.

11

To quantify the comparison, relative differences in the wavefields were computed. The relative difference in the peak-to-peak amplitudes of the first vertical arrivals were between 3% − 6% for the set of models. Figures 23,24 show the relative differences in each component of the time series for the eight models. We have defined the relative difference to be the absolute difference of the phase screen and finite difference traces at each point in the x-direction and time for $z = 12.5$ km, divided by the envelope of the finite difference amplitudes for each component. The results are averaged over the 64 receivers in the x-direction and smoothed over a running time window of $T = 2/f_0 = 1$s. The difference is particularly small for the early arrivals. At later times the waves become out of phase with each other and the pointwise comparison worsens. Because the waveforms oscillate fairly rapidly, even slight offsets in phase can lead to substantial differences. The power in the coda agrees well even though there are differences in the relative phase.

The cross correlation of the wavefields provides a measure of the similarity of the solutions as a function of time offset. The cross correlation is defined by $\langle s(t)s(t + \tau)\rangle$ for a time series $s(t)$, where τ is the time lag. The angled brackets denote a statistical average, in this case over the receivers in the x-direction and also over t. The cross correlations are normalized by the autocorrelation at zero time lag of the finite difference results. The cross correlation for the models are shown in Figures 25,26. The numbers in the figures adjacent to the model numbers correspond to the maximum values. The wavefields are highly correlated at zero time lag, which indicates that the arrival times computed by the two methods are consistent.

Figures 23-26 provide a measure of which types of media the phase screen method treats most accurately. Weaker media (2%) are treated better than the moderately strong media (5%). Also, the results compare more favorably for exponential rather than self-similar media. Backscatter clearly plays a more significant in the latter cases. Figure 24 shows that the media with $a = 2$ km result in only a slight increase in relative error as compared with the media with $a = 5$ km. (The similarity in the curves is a result of using the same random seed to generate the media.) Also, the horizontal components are more accurate for media with constant rather than varying Poisson ratio. This is apparently a result of the particular P and S wave decomposition employed in the phase screen method.

Comparison of Temporal Energy Centroids

To measure the differences in the treatment of conversion and wide-angle scattering, including backscattering, the 64 synthetics generated at $z = 0$ in each model were bandpass filtered using a zero-phase shift Gaussian bandpass filter as in the study by McLaughlin and Anderson (1987). The filters were centered at integer

12

frequency between 1 - 7 Hz with full-width at half-maximum of 1 Hz. The temporal energy centroids of the unfiltered and filtered synthetics were then computed. The centroid for a time series $s(t)$ is defined as

$$T_c = \frac{\int s(t)^2 \, t \, dt}{\int s(t)^2 \, dt}.$$

(7)

The centroids were then averaged over the 64 receivers and plotted in Figures 27-34 for the eight models. The solid and dashed lines in the figures correspond to the averaged centroids of the unfiltered synthetics. The error bars represent ± one standard deviation about the mean. For models 1,2,5,6 with 2% velocity variations, the comparison is quite good. There is virtually no difference between the centroids of the unfiltered finite difference and phase screen synthetics. The time delay of the 4-5 Hz frequencies relative to the 1-2 Hz frequencies is exhibited by both methods. As expected, the phase screen results do not show quite as much delay, particularly for models 3,4,7,8 where backscatter is more significant. Note that for model 3, where the centroids do not monotonically increase with frequency, the phase screen centroids follow the same curve as the finite difference centroids, with a slight offset due to backscatter. McLaughlin and Anderson (1987) attributed similar patterns in their results to scattering resonances. In general, the amount of dispersion increases with the magnitude of the velocity fluctuations and with the presence of more small-scale structure; the self-similar medium leads to greater dispersion than does the exponential. There is also an overall delay of nearly 1 second of the waveforms in the media with 5% fluctuations relative to the media with 2%.

4. CONCLUSIONS

The random media we have considered in this study were not intended to model any particular portion of the crust, however, they are quite reasonable. Studies of the crust under the Montana LASA (Aki, 1973; Capon, 1974; Bertreussen et al., 1975) have used a single layer isotropic Gaussian medium model. The estimated thickness of the layer 60 km, correlation length $a = 10$ km and rms P wave velocity perturbation between 1.9% − 4% are well within the limits of our study. A realistic model of the crust and upper mantle under NORSAR has been proposed by Wu and Flatté (1990). The model consists of overlapping exponential and self-similar layers. (Actually, truncated power spectra corresponding to these correlation functions were used.) The estimated total thickness ∼ 250 km, correlation length $a > 20$ km and rms P wave velocity perturbation between 0.5% − 2.2% are also characteristic of our study.

13

It is evident that the phase screen method is most accurate over the first portion of the seismograms where the arrivals have undergone only small-angle scattering; at later times backscatter becomes more significant. Figures 7-22 demonstrate the range of accuracy of the phase screen method, depending on the model. Although the grid has been sufficiently sampled such that propagation errors in the finite difference solution are negligible, large-amplitude spurious boundary reflections are present in the finite difference synthetics. Thus, differences in the solutions at intermediate to late times can only partially be attributed to errors in the phase screen method (cf. Appendix B).

We believe that there are a significant number of problems in seismology that may necessitate the use of the phase screen method. It provides the flexibility to perform simulations on a variety of machines, from work stations to supercomputers. The substantial reduction in execution time, relative to the finite difference method, allows for substantially longer propagation distances, more extensive parametric studies, ensemble averaging over realizations, and 3-D simulations to be considered. Simulations in 3-D media are of particular interest if data from three-component stations, located above highly heterogeneous media, are to be analyzed.

Appendix A. The Phase Screen Formulation

Starting with the decoupled wave equations in expression (4), the solution in three dimensions, between any consecutive pair of phase screens, may be expressed as

$$\mathbf{u}(\mathbf{x}) = \int \frac{d^2 k_\perp}{(2\pi)^2} \left\{ \hat{e}_P(\mathbf{k}_\perp) A(\mathbf{k}_\perp) e^{i\mathbf{k}_P \cdot \mathbf{x}} + \hat{e}_S^I(\mathbf{k}_\perp) B_I(\mathbf{k}_\perp) e^{i\mathbf{k}_S \cdot \mathbf{x}} \right\}, \qquad \text{(A.1)}$$

where A and B_I are Fourier coefficients of the P and S waves, respectively. Adopting a standard convention of summing over repeated indices, there is an implicit sum over I which labels the two polarizations of the S wave. Our notation for the wave vectors is as follows:

$$\mathbf{k}_\perp = (k_x, k_y), \qquad \text{(A.2)}$$

$$\mathbf{k}_P = (\mathbf{k}_\perp, k_\alpha), \qquad \mathbf{k}_S = (\mathbf{k}_\perp, k_\beta), \qquad \text{(A.3)}$$

14

$$k_\alpha = \sqrt{k_P^2 - k_\perp^2}, \qquad k_\beta = \sqrt{k_S^2 - k_\perp^2}, \tag{A.4}$$

where $k_P = |\mathbf{k}_P| = w/\bar{\alpha}$, $k_S = |\mathbf{k}_S| = w/\bar{\beta}$, and $\bar{\alpha}$ and $\bar{\beta}$ are the average propagation speeds. The unit vectors $\hat{e}_P$ and $\hat{e}_S^I$ are defined such that the curl and divergence constraints are satisfied, i.e. $\mathbf{k}_P \times \hat{e}_P = 0$ and $\mathbf{k}_S \cdot \hat{e}_S^I = 0$, $I = 1, 2$. Unit vectors satisfying these conditions are

$$\hat{e}_P = \hat{k}_P = \mathbf{k}_P/k_P \tag{A.5}$$

$$\hat{e}_S^1 = \frac{\hat{j} \times \hat{k}_S}{|\hat{j} \times \hat{k}_S|} = (k_S^2 - k_y^2)^{-1/2}(k_\beta, 0, -k_x) \tag{A.6}$$

$$\hat{e}_S^2 = \frac{\hat{k}_S \times \hat{e}_S^1}{|\hat{k}_S \times \hat{e}_S^1|} = (k_S^2 - k_y^2)^{-1/2} k_S^{-1}(-k_x k_y, k_S^2 - k_y^2, -k_y k_\beta). \tag{A.7}$$

Given an initial value of the displacement $\mathbf{u}^{(0)}$ at $z = 0$, the Fourier coefficients $A^{(0)}$ and $B_I^{(0)}$ may be determined by standard Fourier and vector projections. Once these coefficients are known, eq. (A.1) may be used to propagate the displacement to $z = \Delta z$. Accounting for the local variations, the P and S wave terms are multiplied by phase factors of the form in eq. (5) to obtain

$$\begin{aligned}
\mathbf{u}^{(0)}(\mathbf{x})|_{z=\Delta z} = \int \frac{d^2 k_\perp}{(2\pi)^2} \Big\{ &\hat{e}_P\, A^{(0)}(k_x, k_y)\, e^{ik_\alpha \Delta z}\, e^{i\Delta^{(P)}(x,y,\Delta z)} \\
&+ \hat{e}_S^I\, B_I^{(0)}(k_x, k_y)\, e^{ik_\beta \Delta z}\, e^{i\Delta^{(S)}(x,y,\Delta z)} \Big\}\, e^{ik_x x + ik_y y}.
\end{aligned} \tag{A.8}$$

In a previous application where the medium was invariant under translations in the z-direction, the accumulated phase depended on the wavenumber as well. Here we find that it is adequate and more expedient to use phase factors of the form computed in eq. (5).

Now setting the initial value of $\mathbf{u}^{(1)}$ at $z = \Delta z$ equal to the expression on the RHS of eq. (A.8), the new Fourier coefficients $A^{(1)}$ and $B_I^{(1)}$ may be determined in terms of $A^{(0)}$ and $B_I^{(0)}$ and the phase factors. The general form of these relations is

$$A^{(N)}(k_x, k_y) = \frac{1}{\hat{k}_S \cdot \hat{k}_P} \int dx\, dy \int d^2k'\, e^{i(k'_x - k_x)x + i(k'_y - k_y)y}$$

$$\cdot \left\{ \hat{k}_S \cdot \hat{e}_P(k'_x, k'_y)\, A^{(N-1)}(k'_x, k'_y)\, e^{ik'_\alpha \Delta z}\, e^{i\Delta^{(P)}(x,y,N\Delta z)} \right.$$

$$\left. + \; \hat{k}_S \cdot \hat{e}_S^I(k'_x, k'_y)\, B_I^{(N-1)}(k'_x, k'_y)\, e^{ik'_\beta \Delta z}\, e^{i\Delta^{(S)}(x,y,N\Delta z)} \right\} \qquad (A.9)$$

$$B_I^{(N)}(k_x, k_y) = \frac{1}{\hat{k}_S \cdot \hat{k}_P} \int dx\, dy \int d^2k'\, e^{i(k'_x - k_x)x + i(k'_y - k_y)y}\, (\hat{k}_S \times \hat{e}_S^I(k_x, k_y)) \cdot$$

$$\cdot \left\{ (\hat{k}_P \times \hat{e}_P(k'_x, k'_y))\, A^{(N-1)}(k'_x, k'_y)\, e^{ik'_\alpha \Delta z}\, e^{i\Delta^{(P)}(x,y,N\Delta z)} \right.$$

$$\left. + \; (\hat{k}_P \times \hat{e}_S^J(k'_x, k'_y))\, B_J^{(N-1)}(k'_x, k'_y)\, e^{ik'_\beta \Delta z}\, e^{i\Delta^{(S)}(x,y,N\Delta z)} \right\}. \qquad (A.10)$$

The P/S coupling is evident in these equations. If the phase factors are constant, it is straightforward to show that the waves decouple. Thus conversion is caused by the local velocities distorting the wavefronts.

For the purposes of this paper, we shall now consider only two dimensions, which is recovered as a special case by setting $k_y = 0$. If $k_y = 0$, the coefficients $B_2^{(N)}$ decouple from $A^{(N)}$ and $B_1^{(N)}$ in the recursion relations, and hence will be set to zero. For computational purposes, the continuous Fourier expansions used to express the displacement are replaced with discrete versions. Let $k_x \rightarrow k_m = 2\pi m/L$, $A^{(N)}(k_x, k_y) \rightarrow A_m^{(N)}$, and $B_1^{(N)}(k_x, k_y) \rightarrow B_m^{(N)}$, where m is an integer and L is the length of the screen. The displacement after N phase screens becomes

$$\mathbf{u}^{(N)}(\mathbf{x}) = \sum_m A_m^{(N)} \hat{e}_{Pm}\, e^{ik_{\alpha,m}z + ik_m x} + \sum_\mu B_\mu^{(N)} \hat{e}_{S\mu}\, e^{ik_{\beta,\mu}z + ik_\mu x}, \qquad (A.11)$$

Now define the vector of Fourier coefficients in block form as

$$\begin{pmatrix} A_m^{(N)} \\[2mm] B_\mu^{(N)} \end{pmatrix} = \left(A_{-M_P}^{(N)}, ..., A_0^{(N)}, ..., A_{M_P}^{(N)}, B_{-M_S}^{(N)}, ..., B_0^{(N)}, ..., B_{M_S}^{(N)} \right)^{\mathrm{T}}. \qquad (A.12)$$

16

M_P and M_S are the greatest integers less than $wL/2\pi\bar{\alpha}$ and $wL/2\pi\bar{\beta}$ respectively, and T denotes the transpose of the row vector. Only the modes with harmonic z-dependence are included since we are interested in propagation distances for which the evanescent modes would be exponentially damped away. The recursion relations for the Fourier coefficients may now be expressed as

$$
\begin{pmatrix} A_m^{(N)} \\ B_\mu^{(N)} \end{pmatrix} = \begin{pmatrix} U_{mn}^{PP} & U_{m\nu}^{PS} \\ U_{\mu n}^{SP} & U_{\mu\nu}^{SS} \end{pmatrix} \begin{pmatrix} A_n^{(N-1)} \\ B_\nu^{(N-1)} \end{pmatrix}.
\tag{A.13}
$$

The integers m, n range from $-M_P$ to $+M_P$, and the integers μ, ν range from $-M_S$ to $+M_S$, and there are implicit sums over n, ν in this expression. In addition, the Δ-phases may be Fourier expanded as

$$
e^{i\Delta^{(P)}(z)} = \sum_n D_n^{(P)} e^{2\pi i n z/L},
\tag{A.14}
$$

and a similar expression with $P \to S$. Combining this information with eqs. (A.9,A.10) yields

$$
U_{mn}^{PP} = \frac{k_{\beta,m} k_{\alpha,n} + k_m k_n}{k_{\beta,m} k_{\alpha,m} + k_m^2} D_{m-n}^{(P)}
\tag{A.15}
$$

$$
U_{m\nu}^{PS} = \frac{\bar{\beta}}{\bar{\alpha}} \frac{k_m k_{\beta,\nu} - k_\nu k_{\beta,m}}{k_{\beta,m} k_{\alpha,m} + k_m^2} D_{m-\nu}^{(S)}
\tag{A.16}
$$

$$
U_{\mu n}^{SP} = \frac{\bar{\alpha}}{\bar{\beta}} \frac{k_n k_{\alpha,\mu} - k_\mu k_{\alpha,n}}{k_{\beta,\mu} k_{\alpha,\mu} + k_\mu^2} D_{\mu-n}^{(P)}
\tag{A.17}
$$

$$
U_{\mu\nu}^{SS} = \frac{k_{\alpha,\mu} k_{\beta,\nu} + k_\mu k_\nu}{k_{\beta,\mu} k_{\alpha,\mu} + k_\mu^2} D_{\mu-\nu}^{(S)}.
\tag{A.18}
$$

The phase screen algorithm for vector waves may now be summarized as follows. Starting with the initial displacement at $z = 0$, the initial vector of coefficients are obtained. Given a realization of the 2-D grid, it may be divided into equal intervals of length Δz by planes of constant z. The phase factors for each interval are computed via a discrete version of eq. (5); an inverse FFT is used to obtain the

17

Fourier coefficients $D_n^{(P)}$ and $D_n^{(S)}$, which are inserted into the matrix above. These relations are successively applied to the initial vector of coefficients until the final vector is obtained. The displacement in eq. (A.11) is evaluated using an FFT.

Appendix B. Accuracy of the Finite Difference Technique

The accuracy of the finite difference formulation used here was investigated by Charrette (1991). In that study it was shown that the finite difference solution converges to the exact solution as the discretization of the medium increases. In particular, for the spatial and temporal sampling rates used in this note, it was shown that the error in phase and group velocities are less than a few percent. The accuracy tests described in Charrette (1991) assume the medium is largely homogeneous. When the medium is highly heterogeneous, errors in calculating the velocity gradients will also effect the solution. The behavior of the finite difference technique is these situations is not well understood and is likely to depend greatly on the nature of the medium. Due to the complexity of the problem, the only tractable way to estimate these errors is to exploit the fact that in the continuum limit the finite difference solution converges to the true solution.

To illustrate this, we ran one simulation at twice the spatial and temporal sampling rate used throughout this study. This resulted in a sampling rate of 55 points per wavelength for the shortest wavelength P-wave (110 points per wavelength for the center frequency) and a sampling rate of 30 points per wavelength for the shortest wavelength S-wave (60 points per wavelength for the center frequency). Figures 31 and 32 show that the difference between the two solutions is negligible.

Additional errors are induced into the finite difference solution from the boundary conditions at the ends of the grid. Randall (1988) has noted that paraxial boundary conditions, such as the one proposed by Clayton and Engquist (1977), perfectly absorb elastic waves normally incident, but only partially absorb obliquely incident waves. He further stated that portions of the wave incident at angles between about 30° and 45° may lead to unacceptable boundary reflections. The horizontal displacement is apt to contain more large-amplitude spurious reflections (e.g., Fig. 10, Frankel and Clayton, 1986; Fig. 6, Randall, 1988). Also, stronger scattering media are more likely to produce spurious signals since there will typically be more wide-angle scatter incident on the boundary.

ACKNOWLEDGEMENTS

REFERENCES

Aki, K., Scattering of P waves under the Montana Lasa, *J. Geophys. Res.*, *78*, 1334–1246, 1973.

Aki, K., and P. G. Richards, *Quantitative Seismology: Theory and Methods*, Vols. 1 and 2, W. H. Freeman, San Francisco, Calif., 1980.

Alford, R. M., K. R. Kelly, and D. M. Boore, Accuracy of finite difference modeling of the acoustic wave equation, *Geophysics*, 39, 834–842, 1974.

Ansell, J. H., The decoupling of P and S waves in inhomogeneous media, *Physics of the Earth and Planetary Interiors*, 26, 246–249, 1981.

Bertreussen, K. A., A. Christoffersson, E. S. Husebye, and A. Dahle, Wave scattering theory in analysis of P wave anomalies at NORSAR and LASA, *Geophys. J. R. Astr. Soc.*, 42, 402–417, 1975.

Boore, D. M., *Finite difference methods for seismic wave propagation in heterogeneous materials*, pp. 1–37, vol. 11 of *Methods in Computational Physics*, Academic Press, New York, 1972.

Bramley, E. N., The accuracy of computing ionospheric radio-wave scintillation by the thin-phase screen approximation, *J. Atmos. Terr. Phys.*, 39, 367–373, 1977.

Buckley, R., Diffraction by a random phase-changing screen: A numerical experiment, *J. Atmos. Terr. Phys.*, 37, 1431–1446, 1975.

Capon, J., Characterization of crust and upper mantle structure under LASA as a random medium, *Bull. Seismol. Soc. Am.*, *64*, 235–266, 1974.

Charrette, E. E., *Elastic Wave Scattering in Random Media*, Ph.D. Thesis, Massachusetts Institute of Technology, Cambridge, MA, 1991.

Chernov, L. A., *Wave Propagation in a Random Medium*, McGraw-Hill, New York, 1960.

Clayton, R. and B. Engquist, Absorbing boundary conditions for acoustic and elastic wave equations, *Bull. Seismol. Soc. Am.*, *67*, 1529–1540, 1977.

Dainty, A. M., High-frequency acoustic backscattering and seismic attenuation, *J. Geophys. Res.*, *89*, 3172–3176, 1984.

Daudt, C. R., L. W. Braile, R. L. Nowack, and C. S. Chiang, A comparison of finite-difference methods, *Bull. Seismol. Soc. Am.*, *79*, 1210–1230, 1989.

Feit, M. D. and J. A. Fleck, Jr., Light propagation in graded-index optical fibers, *Applied Optics*, vol. 17, no. 24, 3990–3998, 1978.

Filice, J. P., *Studies of the Microscale Density Fluctuations in the Solar Wind using the Power Law Phase Screen Model*, U. Calif., San Diego, Ph.D. Thesis, 1984.

Fisk, M. D., and G. D. McCartor, "The Phase-Screen Method for Elastic Waves and Seismic Discrimination", GL-TR-89-0330, ADA220771, Mission Research Corp., 1989.

Fisk, M. D., and G. D. McCartor, The phase-screen method for vector elastic waves, *J. Geophys. Res.*, 96, 5985–6010, 1991.

Flatté, S. M. (Editor), *Sound Transmission Through A Fluctuating Ocean*, Cambridge University Press, 1979.

Fornberg, B., The pseudospectral method: Comparisons with finite differences for the elastic wave equation, *Geophysics*, *52*, 483–501, 1987.

Frankel, A., A review of numerical experiments on seismic wave scattering, *Pure Appl. Geophys.*, 131, 639–685, 1989.

Frankel, A., and R. W. Clayton, Finite difference simulations of seismic scattering: Implications for the propagation of short-period seismic waves in the crust and models of crustal heterogeneity, *J. Geophys. Res.*, 91, 6465–6489, 1986.

Goff, J. A. and T. H. Jordan, Stochastic modeling of seafloor morphology: inversion of sea beam data for second order statistics, *J. Geophys. Res.*, *93*, 13589–13608, 1988.

Haddon, R. A. W. and E. S. Husebye, Joint interpretation of P-wave time and amplitude anomalies in terms of lithospheric heterogeneities, *Geophys. J. R. Astr. Soc.*, 55, 19–43, 1978.

Hudson, J. A., A parabolic approximation for elastic waves, *Wave Motion*, 2, 207–214, 1980.

Karal, F. C., and J. B. Keller, Elastic wave propagation in homogeneous and inhomogeneous media, *J. Acoust. Soc. Am.*, 31, 694–705, 1959.

Kelly, K. R., R. W. Ward, S. Treitel, and R. M. Alford, Synthetic seismograms: A finite difference approach, *Geophysics*, 41, 2–27, 1976.

Knepp, D. L., Multiple phase screen calculation of the temporal behavior of stochastic waves, *Proc. IEEE*, 71, 722–737, 1983.

Levin, M. K., and S. M. Rytov, Transitions to geometrical approximations in elasticity theory, *Sov. Phys. Acoust.*, 2, 179–184, 1957.

Mandelbrot, B. B., *Fractals*, W. H. Freeman, San Francisco, 1977.

McLaughlin, K. L., and L. M. Anderson, Stochastic dispersion of short-period P-waves due to scattering and multipathing, *Geophys. J. R. Astr. Soc.*, 89, 933–963, 1987.

Martin, J. M. and S. M. Flatté, Intensity images and statistics from numerical simulation of wave propagation in 3-D random media, *Applied Optics*, 27, 2111–2125, 1988.

Mercier, R. P., Diffraction by a screen causing large random phase fluctuations, *Proc. Cambridge Phil. Soc.*, 58, 382–400, 1962.

Randall, C. J., Absorbing boundary conditions for the elastic wave equation, *Geophysics,* 53, 611–624, 1988.

Ratcliffe, J. A., Reports on Progress in Physics, XIX, 190–263, 1956.

Richards, P. G., Weakly coupled potentials for high-frequency elastic waves in continuously stratified media, *Bull. Seismol. Soc. Am.*, 64, 1575–1588, 1974.

Tatarski, V. I., *Wave Propagation in a Turbulent Medium*, McGraw-Hill, New York, 1961.

Thomson, D. J. and N. R. Chapman, A wide-angle split-step algorithm for the parabolic equation, *J. Acoust. Soc. Am.*, 74, 1848–1854, 1983.

Virieux, J., P-SV wave propagation in heterogeneous media: velocity-stress finite-difference method, *Geophysics, 51*, 889–901, 1986.

von Karman, T., Progress in the statistical theory of turbulence, *J. Mar. Res., 7*, 252–264, 1948.

Witte, D., *The Pseudospectral Method for Simulating Wave Propagation*, Ph.D. Thesis, Columbia University, Palisades, NY, 1989.

Wu, R. S. and K. Aki, The perturbation method in elastic wave scattering, *Pure Appl. Geophys., 131,* 605–637, 1990.

Wu, R. S. and S. M. Flatté, Transmission fluctuations across an array and heterogeneities in the crust and upper mantle, *Pure Appl. Geophys., 132,* 175–196, 1990.

Wu, R. S., Seismic wave scattering, in *Encyclopedia of Geophysics*, D. E. James, ed. Van Nostrand Reinhold, 1988.

Figure 1. The multiple phase-screen method replaces (a) each segment of the heterogeneous medium with (b) a uniform segment and a phase screen. The accumulated position-dependent phase is projected onto screen 2.

23

Autocovariance Functions
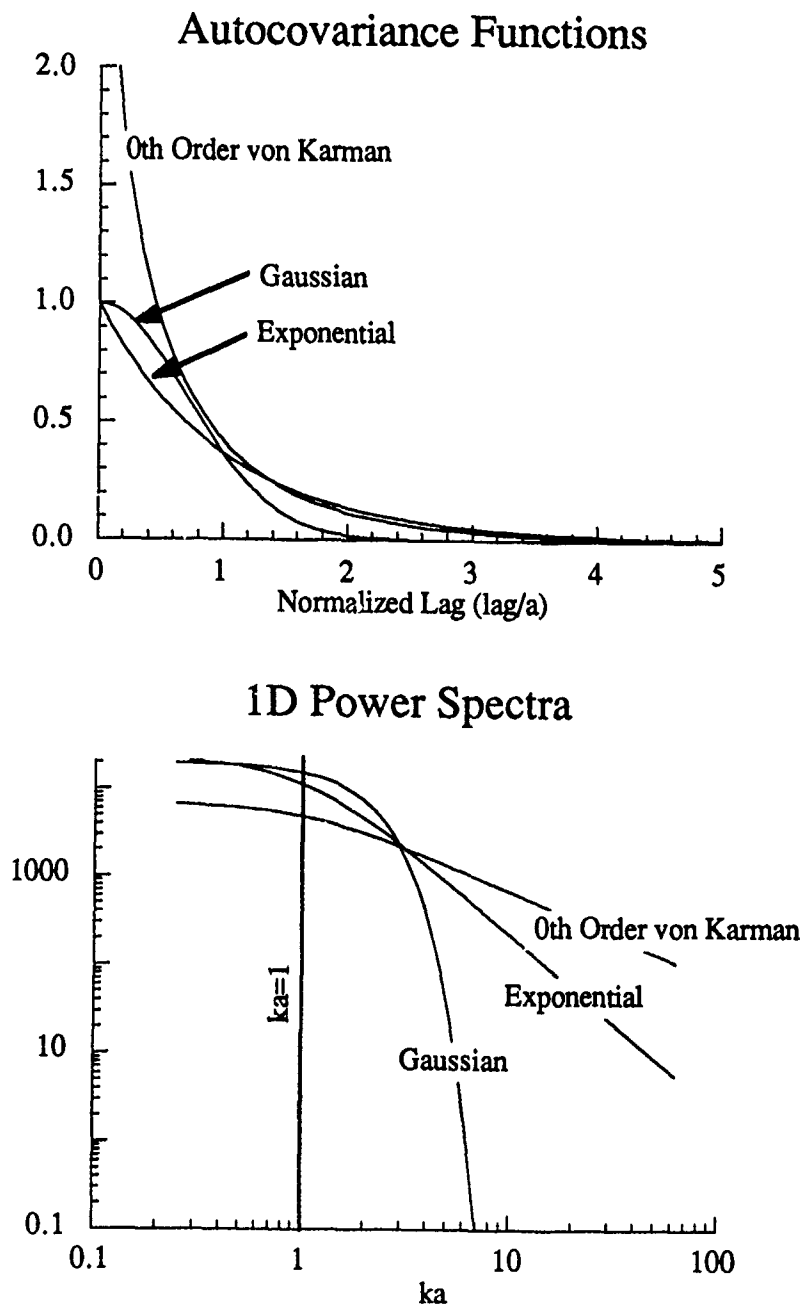
1D Power Spectra

Figure 2. The model autocovariance functions (top) and their 1-D power spectra (bottom). The spectra and normalized so that they have the same power.

24

ACF=Exponential

Offset (m)
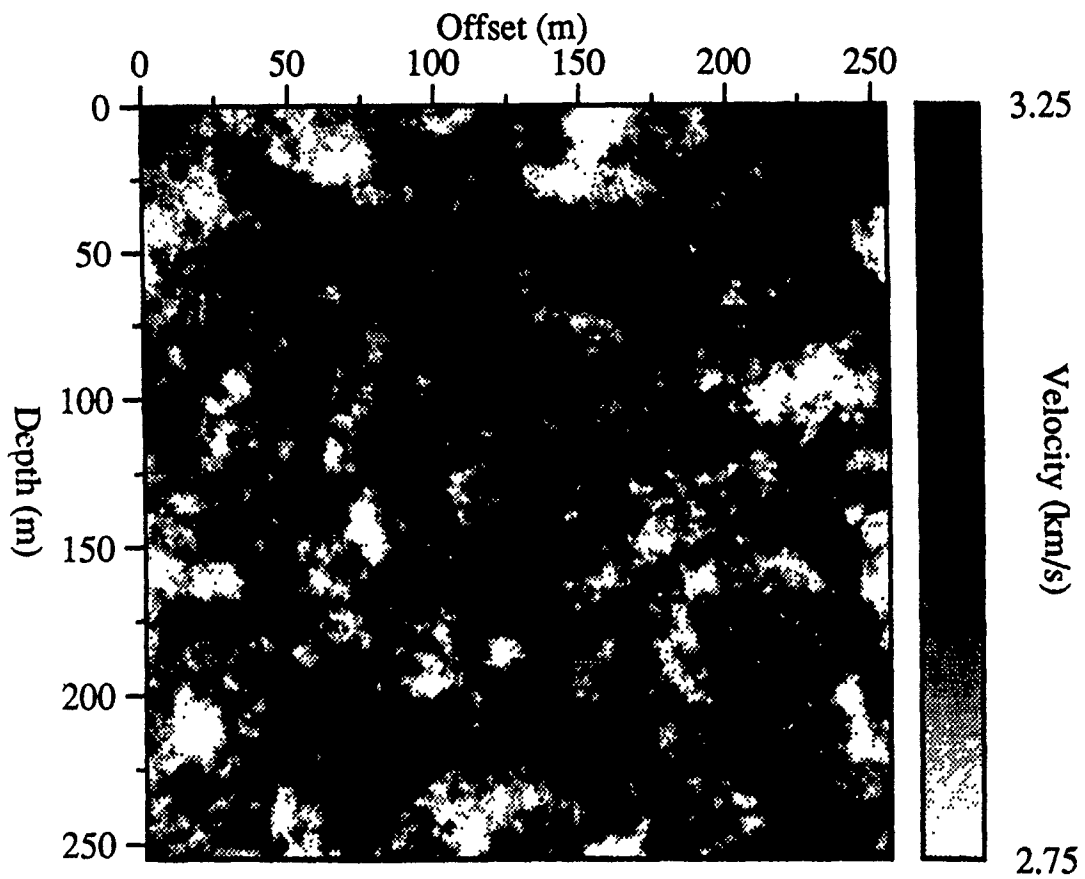
Figure 3.   A 2-D realization of a random medium with an exponential autocorrelation function. The correlation length in this realization is 20m, and there is 5% RMS deviation in the velocity.

25

ACF=0th Order von Karman
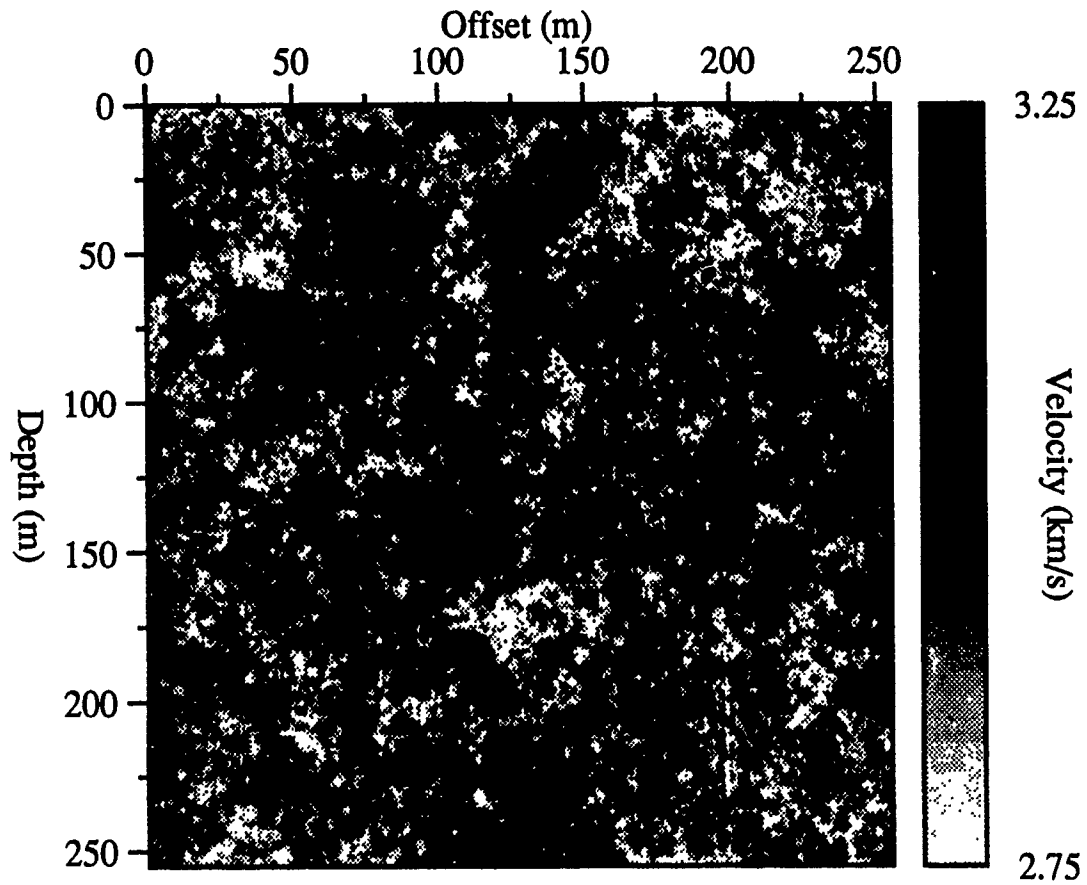
Figure 4. Same as Figure 2, b with a 0th order von Karman auto-correlation function (Charrette, 1991).
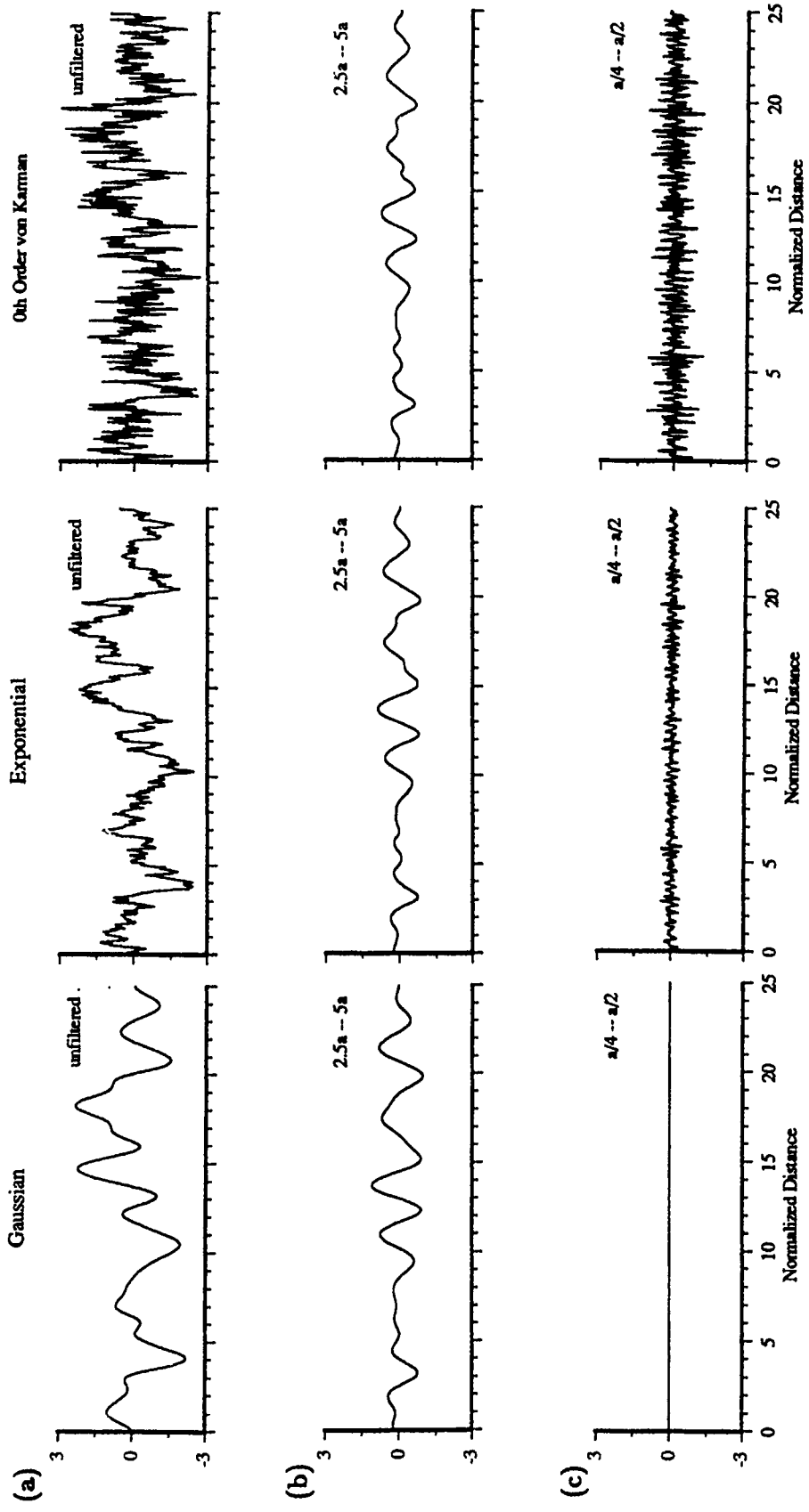
Figure 5. Random realizations from the 1-D Gaussian, exponential, and 0th order von Karman autocorrelation functions. a) unfiltered, b) bandpass filtered allowing wavelengths 2.5a-5a, c) bandpass filtered allowing wavelengths, a/4-a/2. All realizations were constructed with the same random seed, and are plotted at constant scale (After (Frankel, 1989)).

27
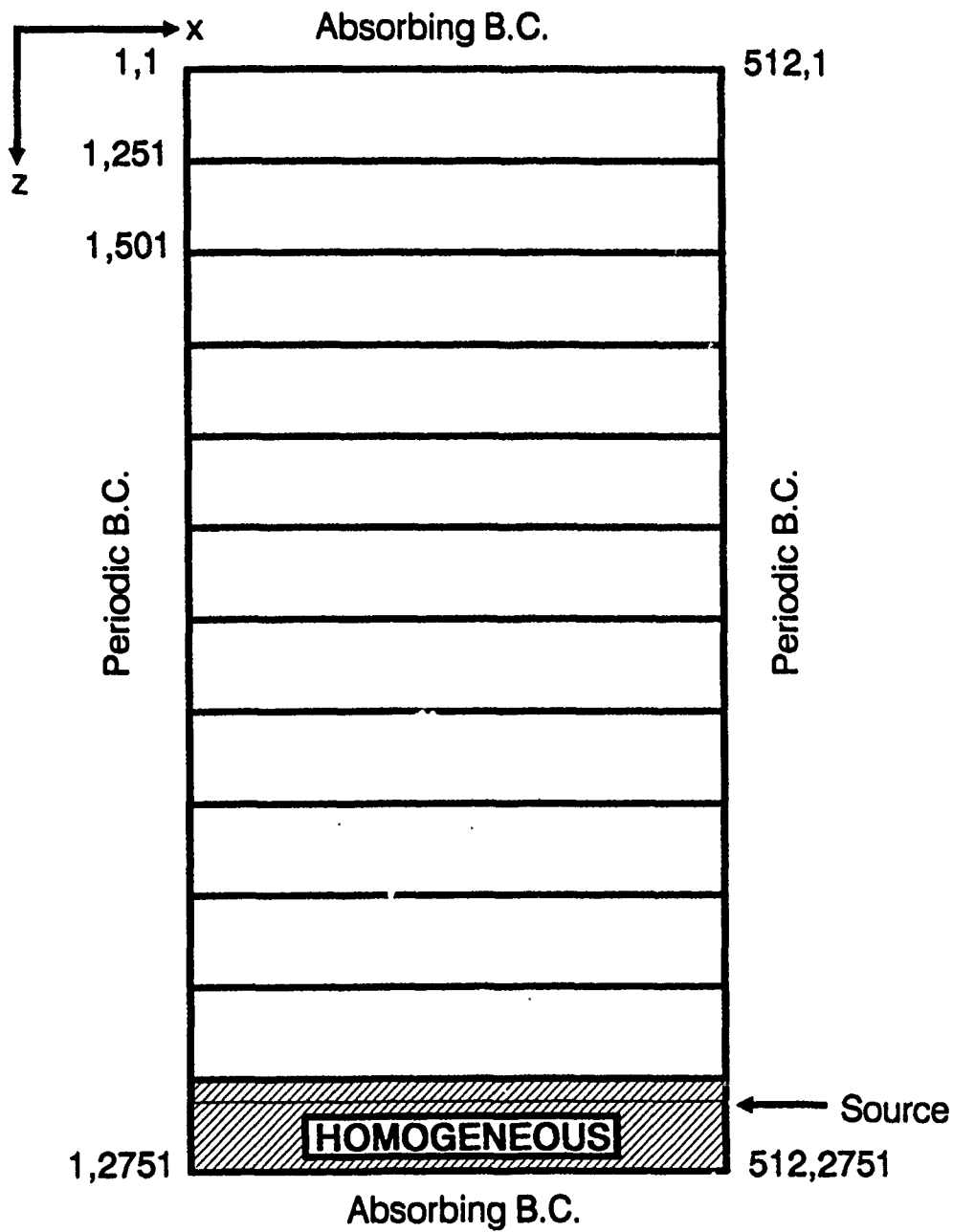
Figure 6. Schematic of the 2-D grid. Arrays of 64 receivers were located every 250 gridpoints in the z-direction.

MODEL #1

COORD
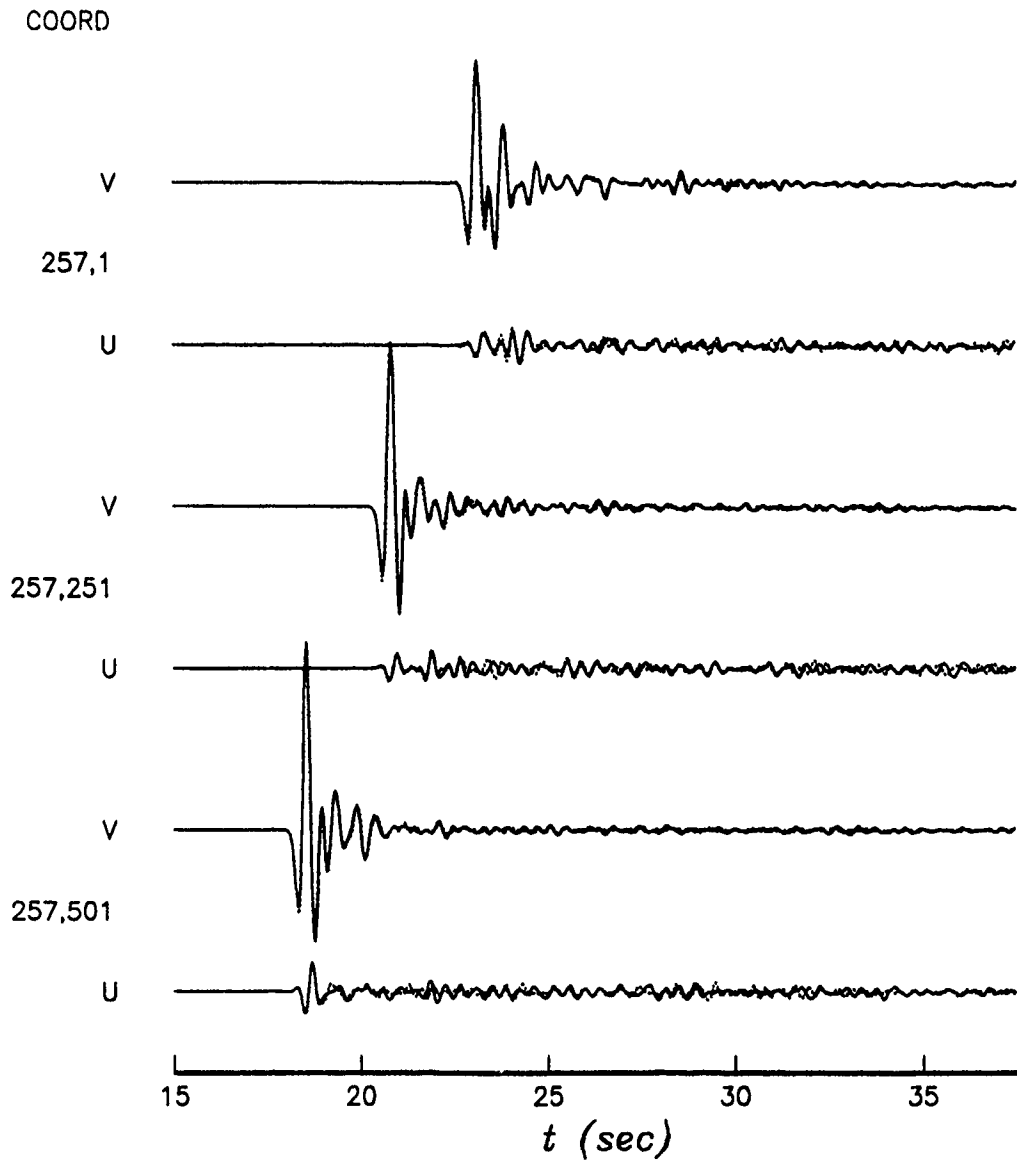
Figure 7. Model 1 synthetics of the vert:cal (V) and horizontal (U) components of the displacement. Receiver locations were at the x-direction midpoint for three depths.
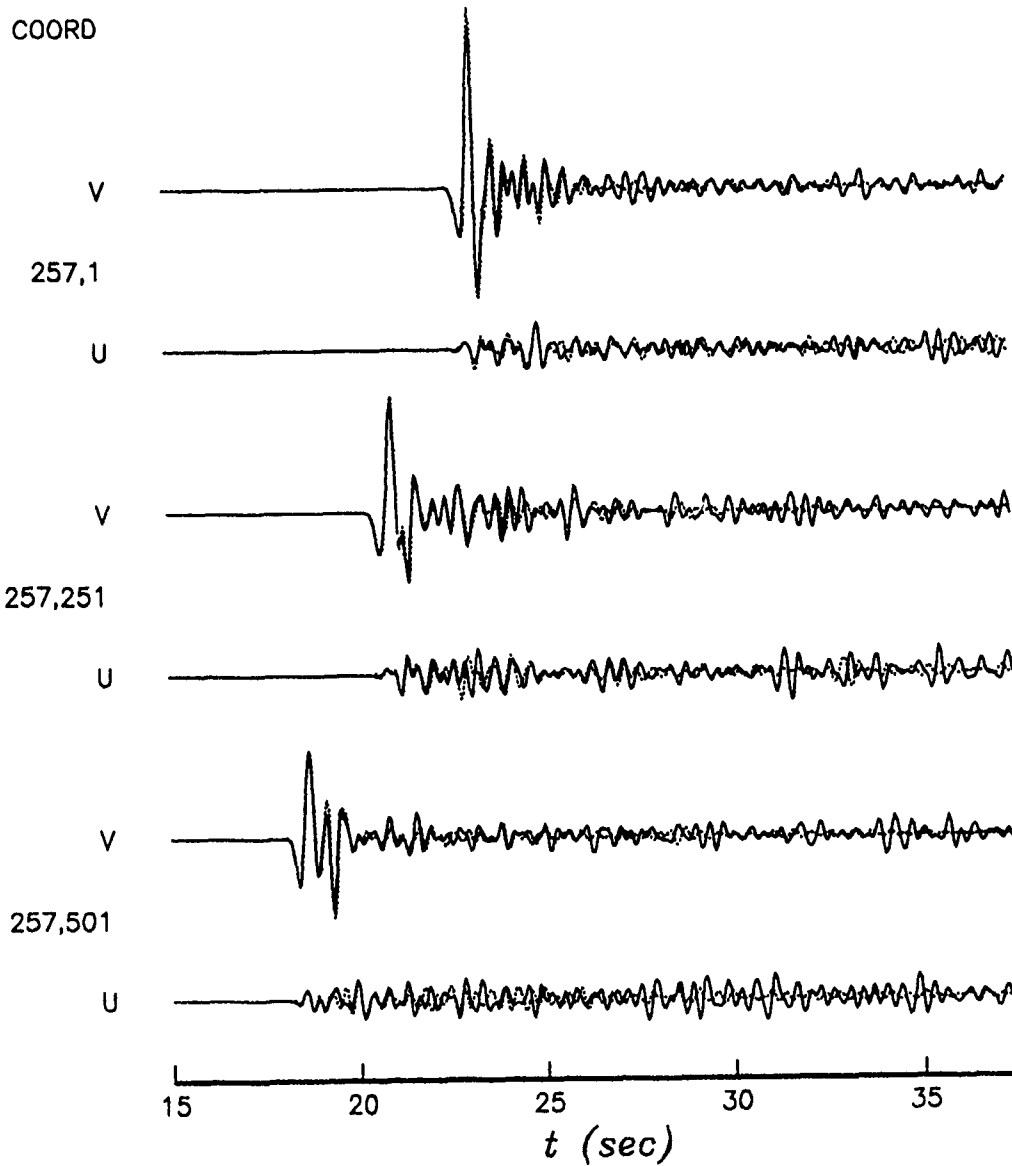
MODEL #2
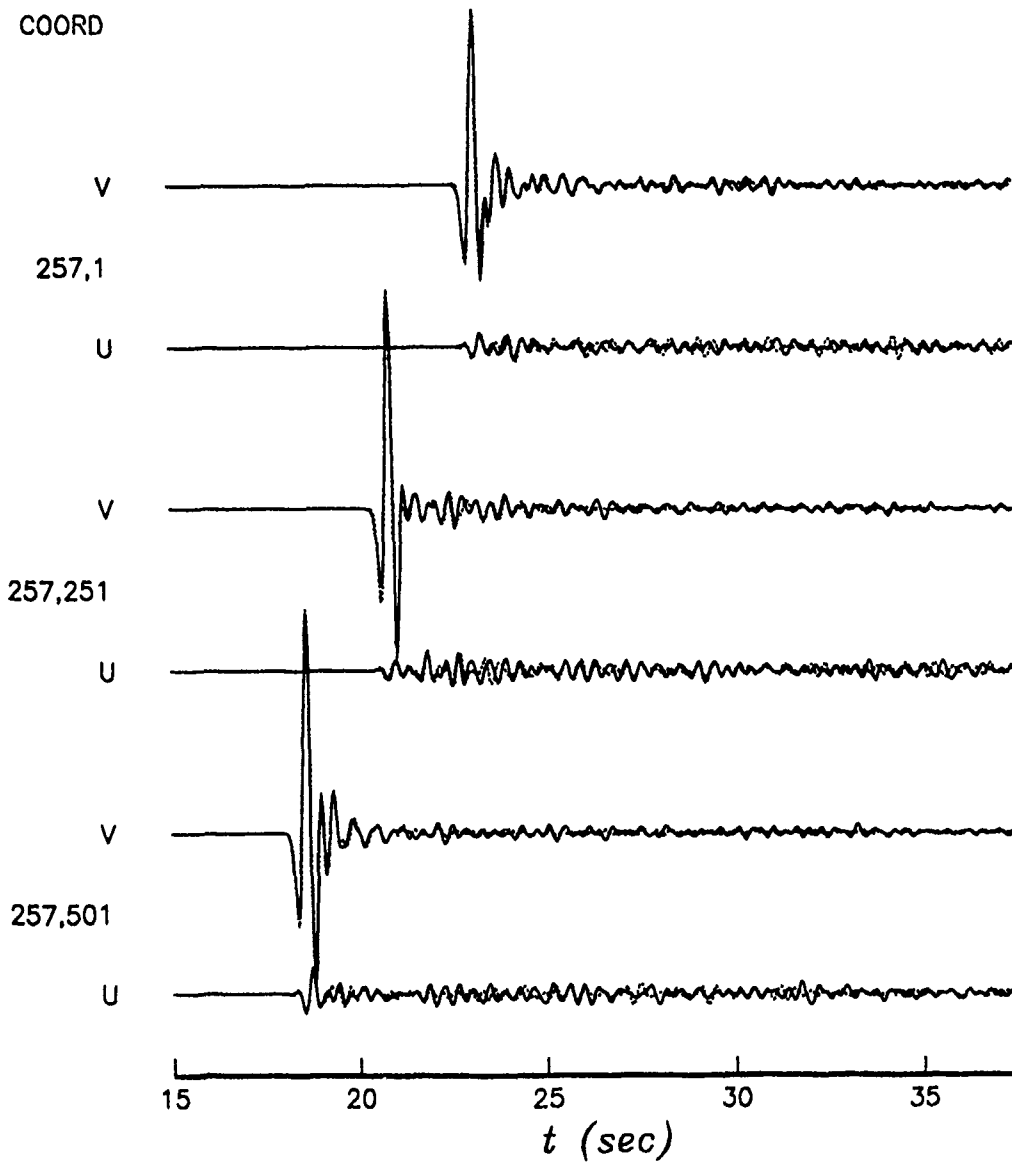
Figure 8. Model 2 synthetics of the vertical (V) and horizontal (U) components of the displacement. Receiver locations were at the x-direction midpoint for three depths.
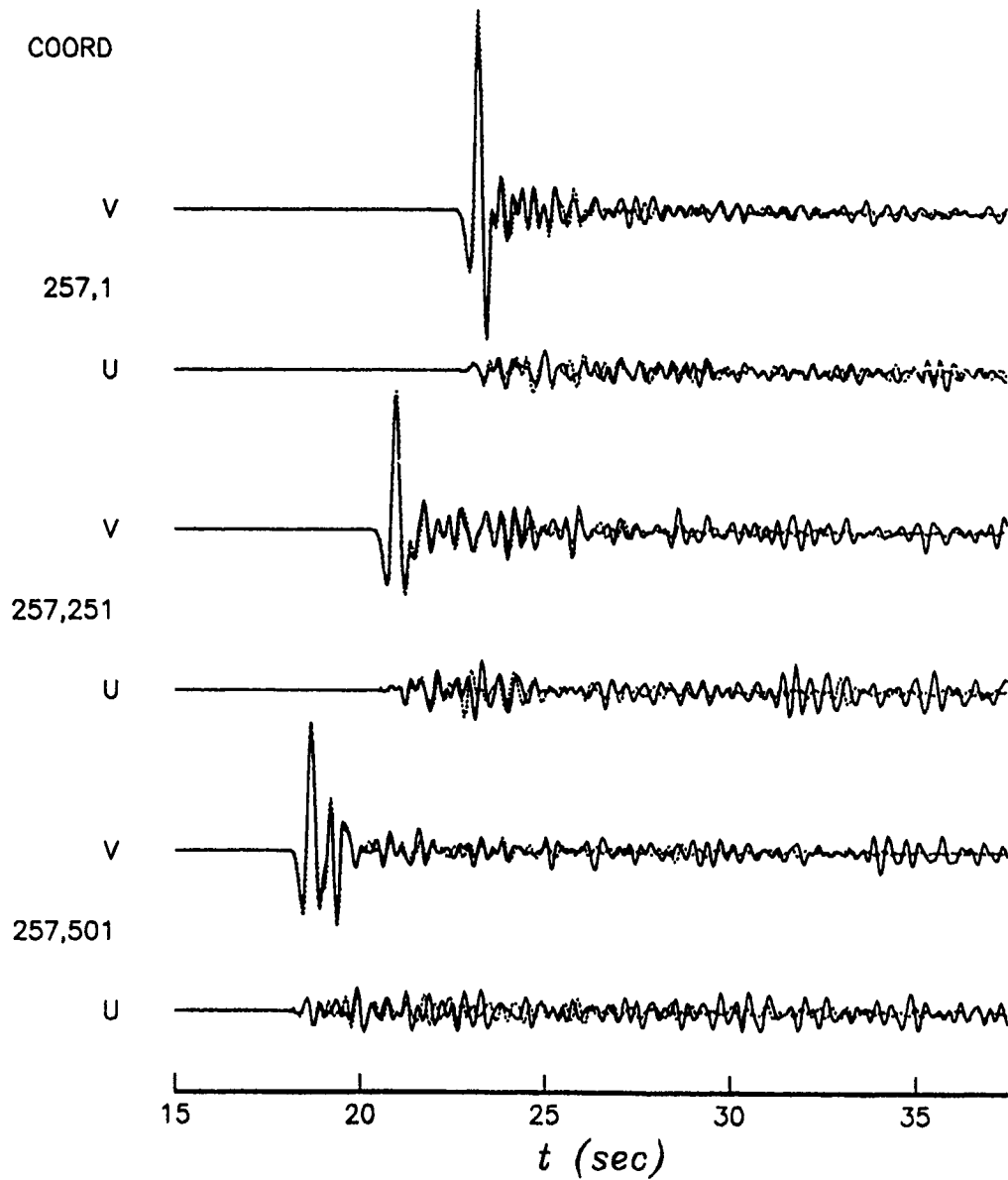
30
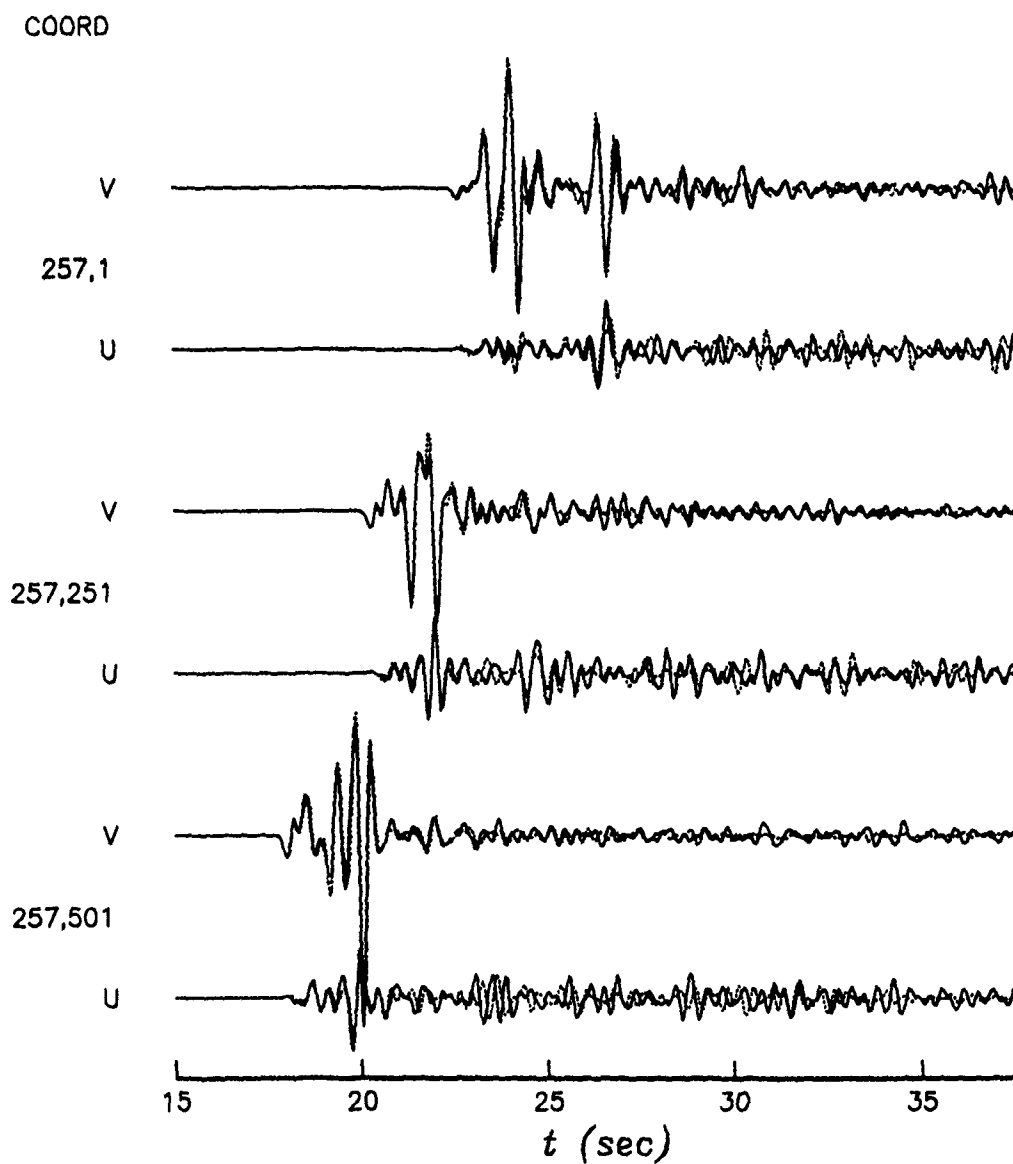
MODEL #3

Figure 9. Model 3 synthetics of the vertical (V) and horizontal (U) components of the displacement. Receiver locations were at the x-direction midpoint for three depths.

31

MODEL #4

COORD
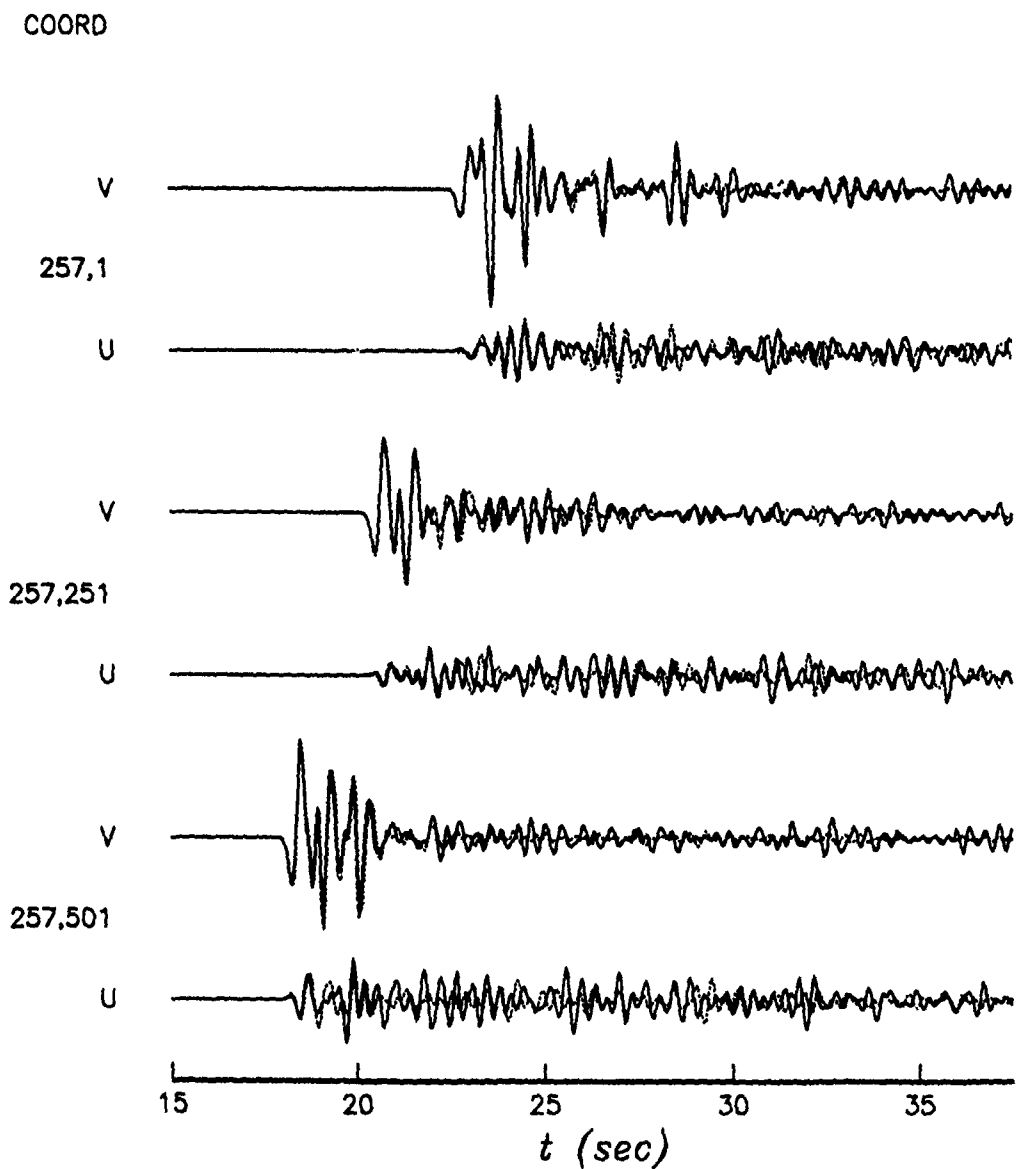
Figure 10. Model 4 synthetics of the vertical (V) and horizontal (U) components of the displacement. Receiver locations were at the x-direction midpoint for three depths.

MODEL #5
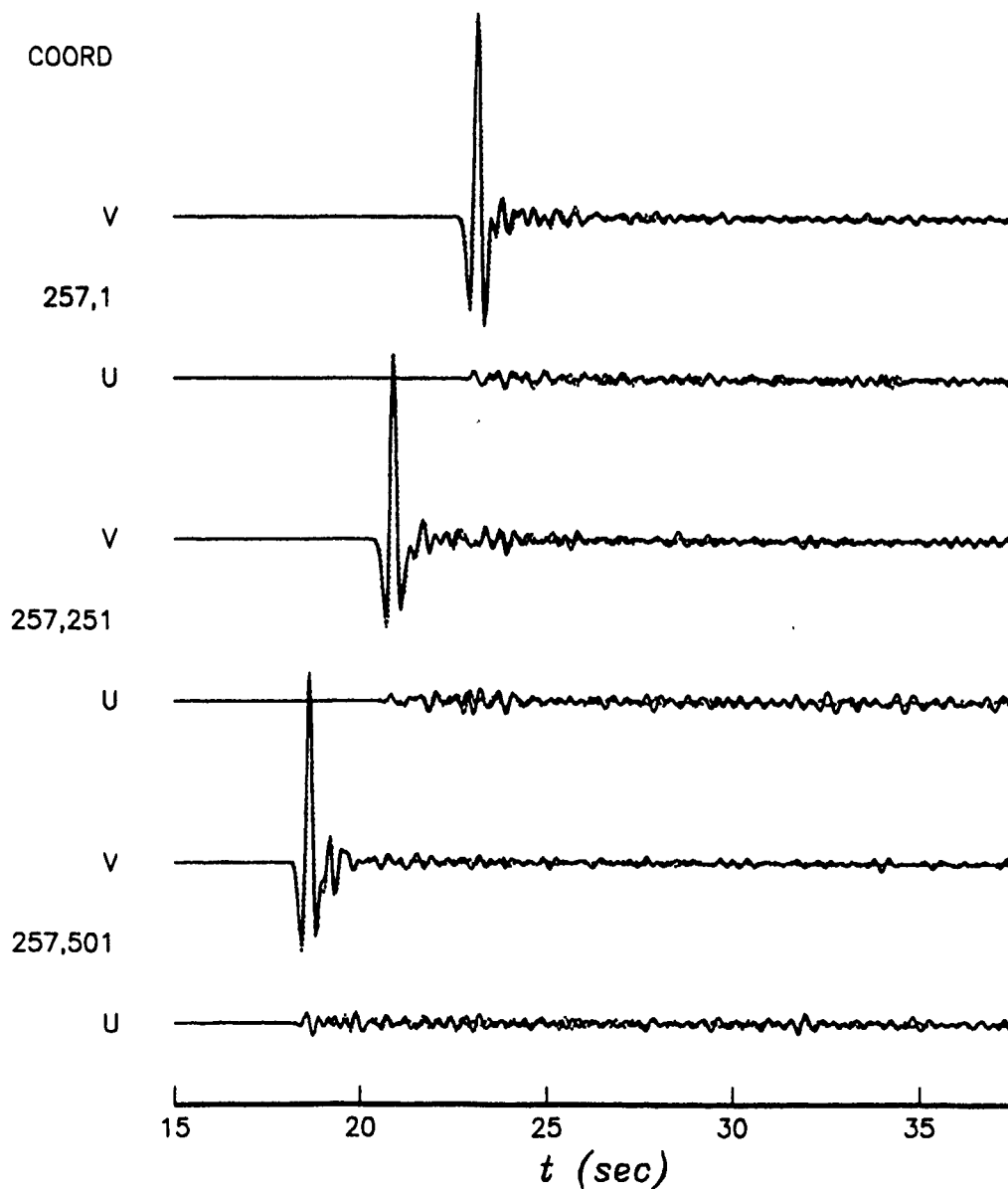
Figure 11. Model 5 synthetics of the vertical (V) and horizontal (U) components of the displacement. Receiver locations were at the x-direction midpoint for three depths.

33
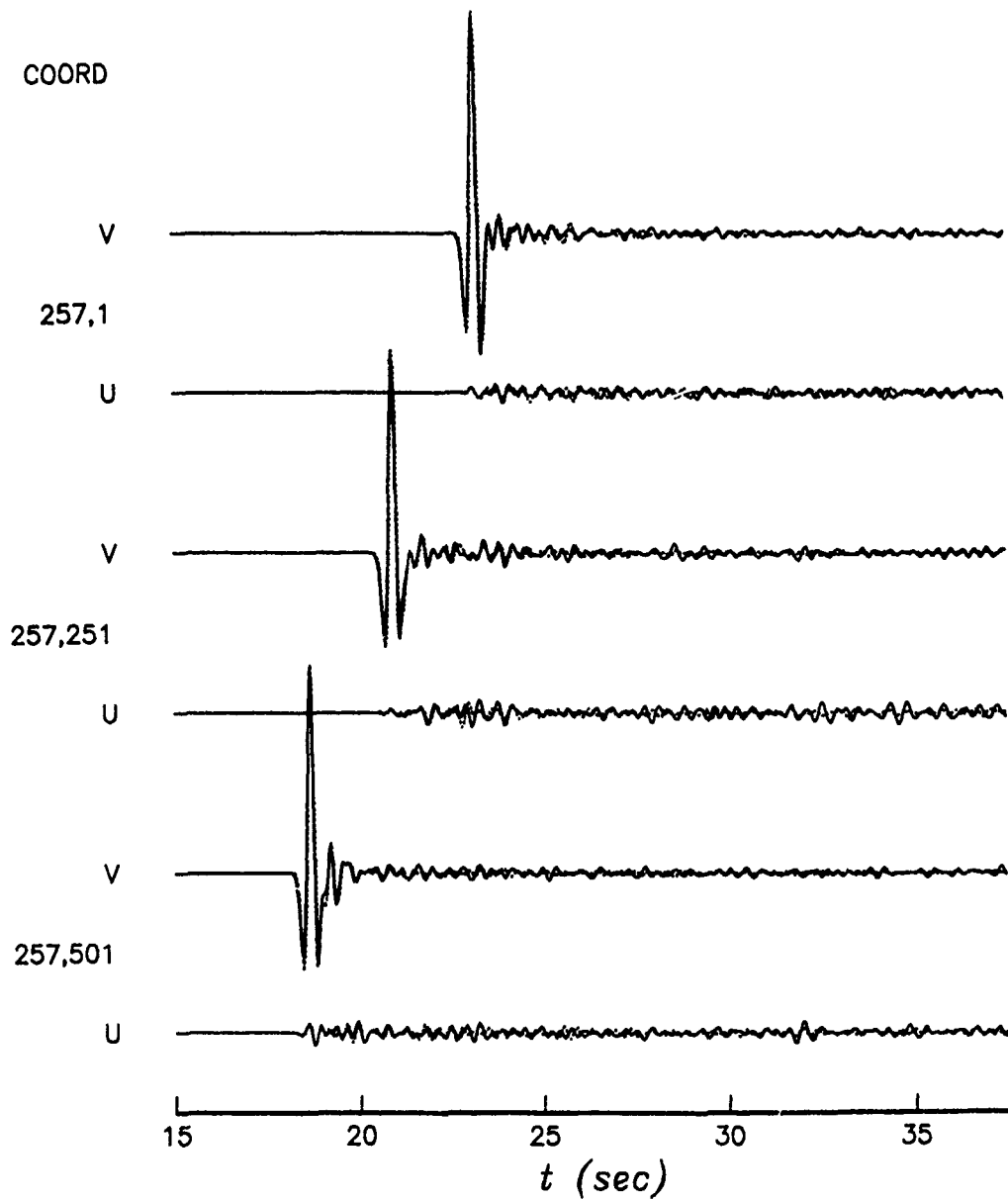
MODEL #6

Figure 12. Model 6 synthetics of the vertical (V) and horizontal (U) components of the displacement. Receiver locations were at the x-direction midpoint for three depths.

34

MODEL #7

COORD

V

257,1

U

V

257,251

U

V

257,501

U

15   20   25   30   35

$t\ (sec)$

Figure 13. Model 7 synthetics of the vertical (V) and horizontal (U) components of the displacement. Receiver locations were at the x-direction midpoint for three depths.

MODEL #8

COORD

V

257,1

U

V

257,251

U

V

257,501

U

15   20   25   30   35

t (sec)

Figure 14.   Model 8 synthetics of the vertical (V) and horizontal (U) components of the displacement. Receiver locations were at the x-direction midpoint for three depths.
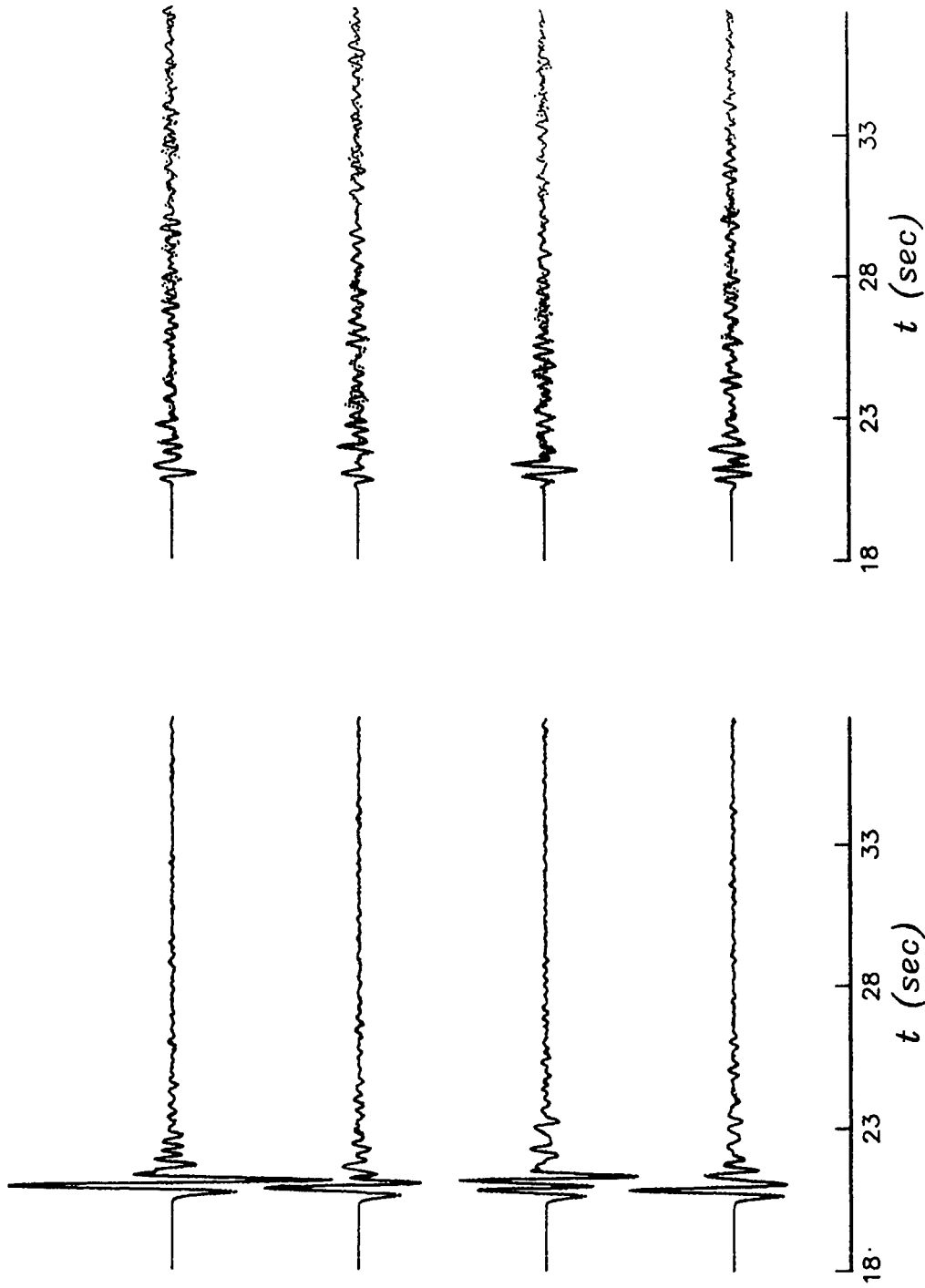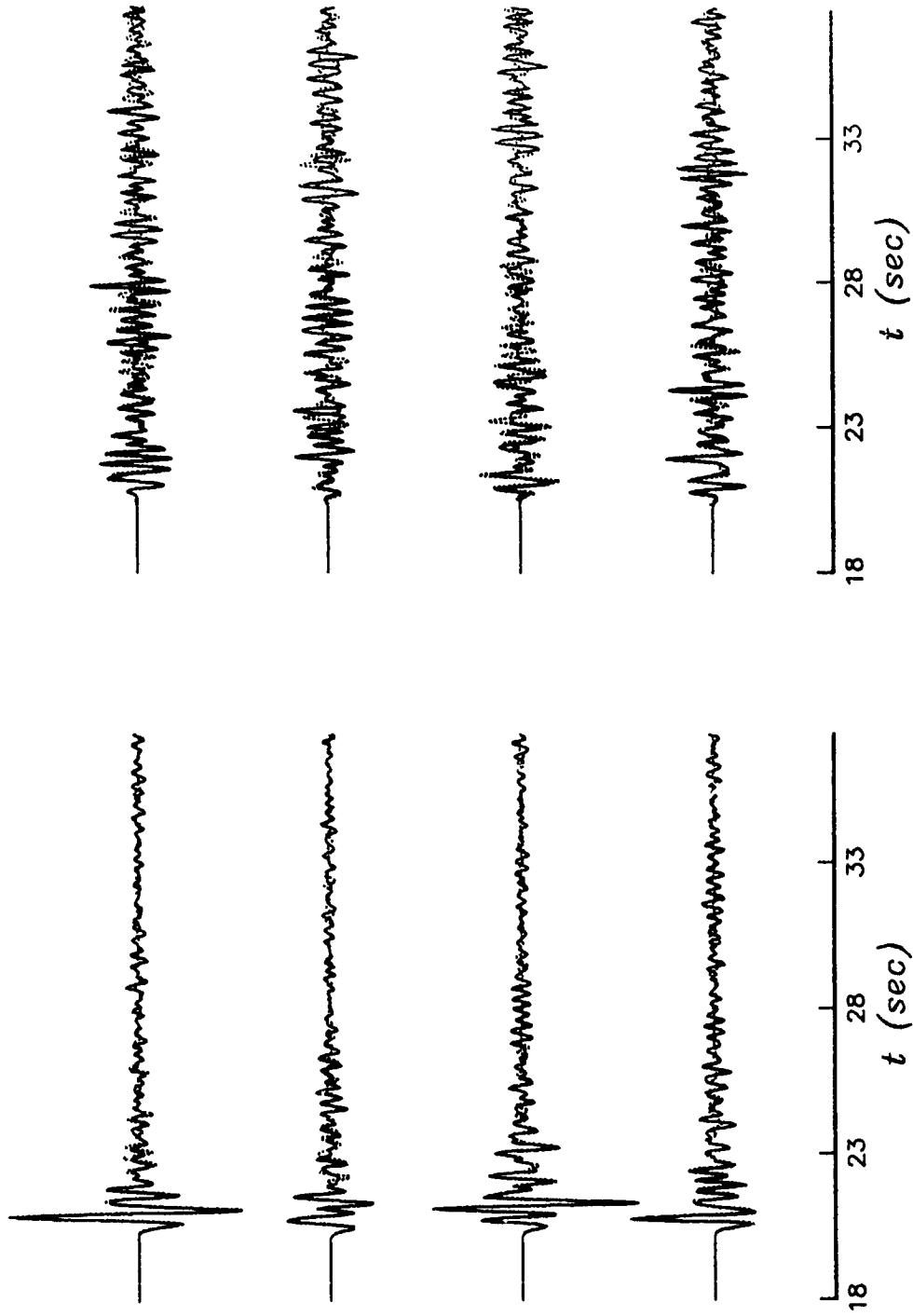
Figure 15. Model 1 synthetics for 4 evenly spaced receivers at a depth of 12.5 km.

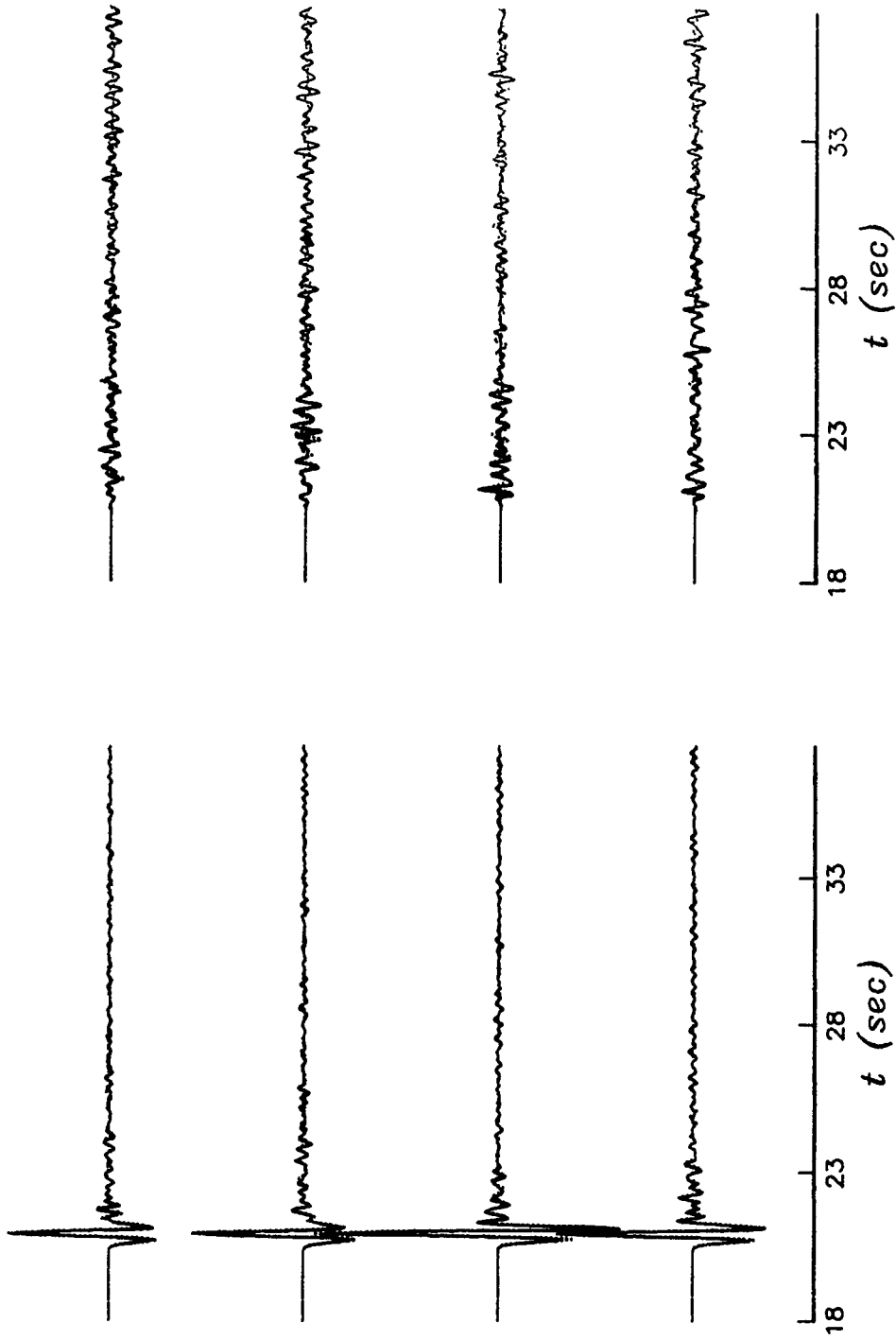Figure 16. Model 2 sythetics for 4 evenly spaced receivers at a depth of 12.5 km.

Figure 17. Model 3 sythetics for 4 evenly spaced receivers at a depth of 12.5 km.

MODEL #4

VERTICAL

HORIZONTAL

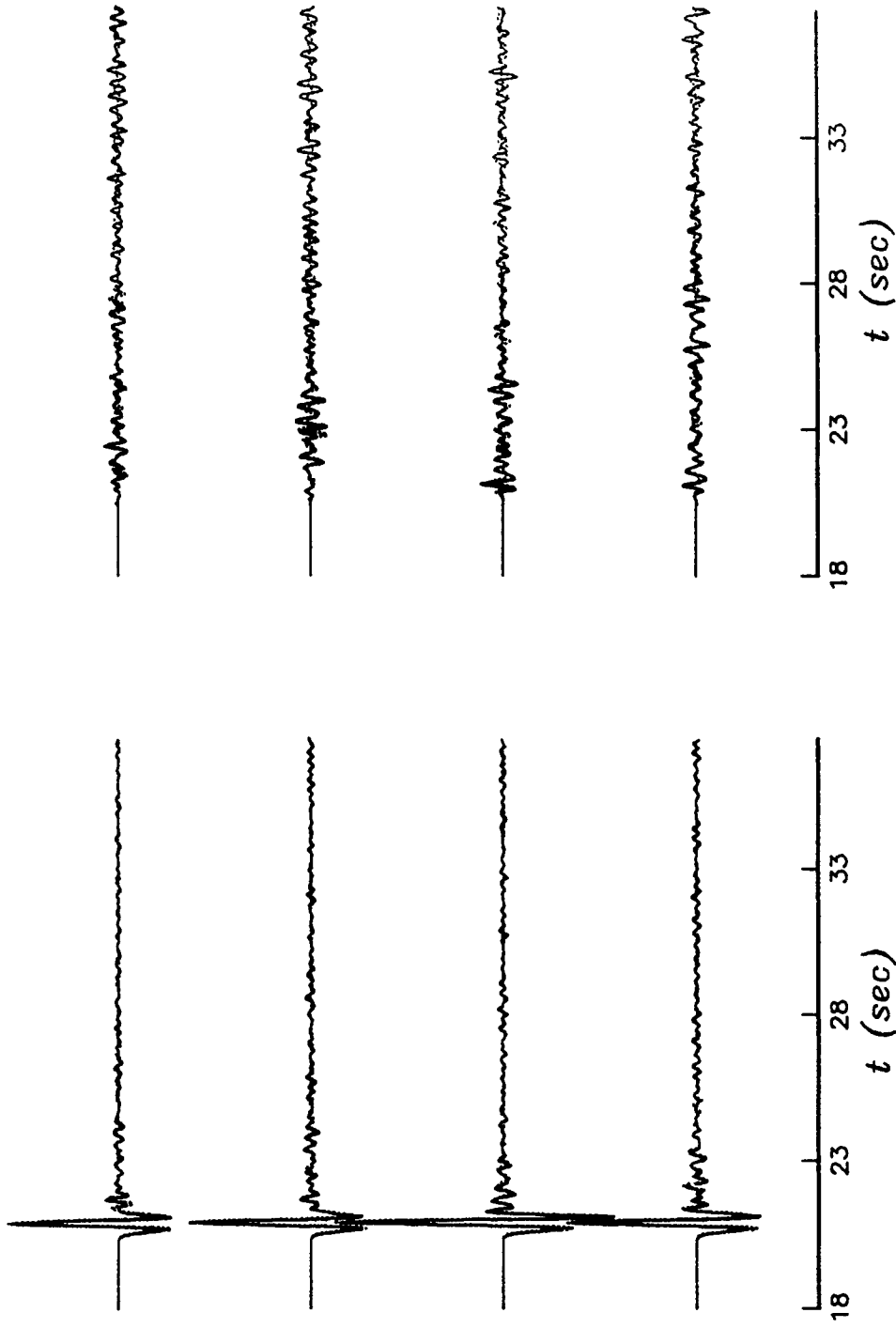t (sec)

Figure 18. Model 4 sythetics for 4 evenly spaced receivers at a depth of 12.5 km.

40

MODEL #5

VERTICAL   HORIZONTAL

Figure 19.   Model 5 sythetics for 4 evenly spaced receivers at a depth of 12.5 km.

Figure 20. Model 6 sythetics for 4 evenly spaced receivers at a depth of 12.5 km.
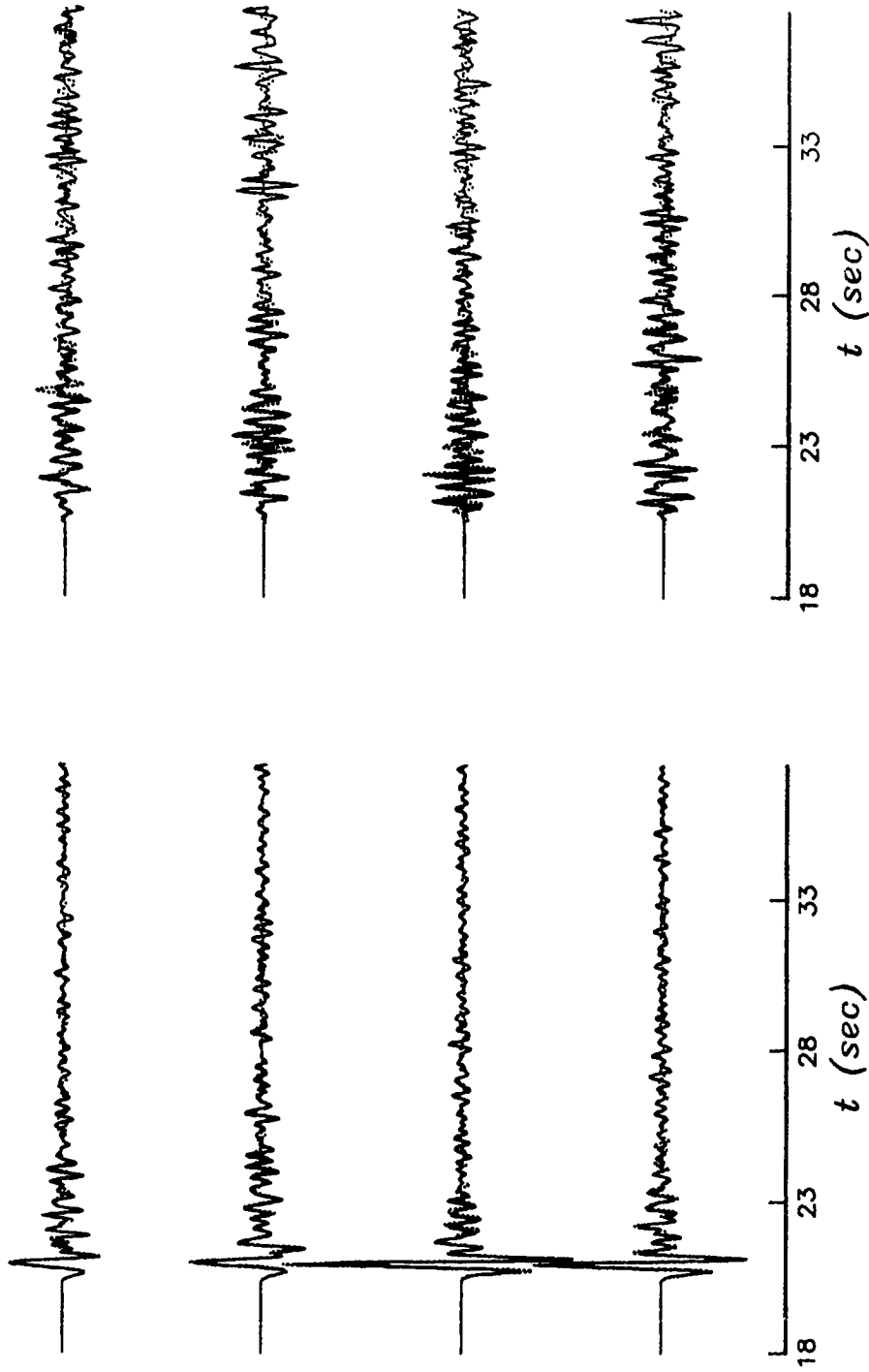
Figure 21.   Model 7 sythetics for 4 evenly spaced receivers at a depth of 12.5 km.

43

MODEL #8

VERTICAL

HORIZONTAL

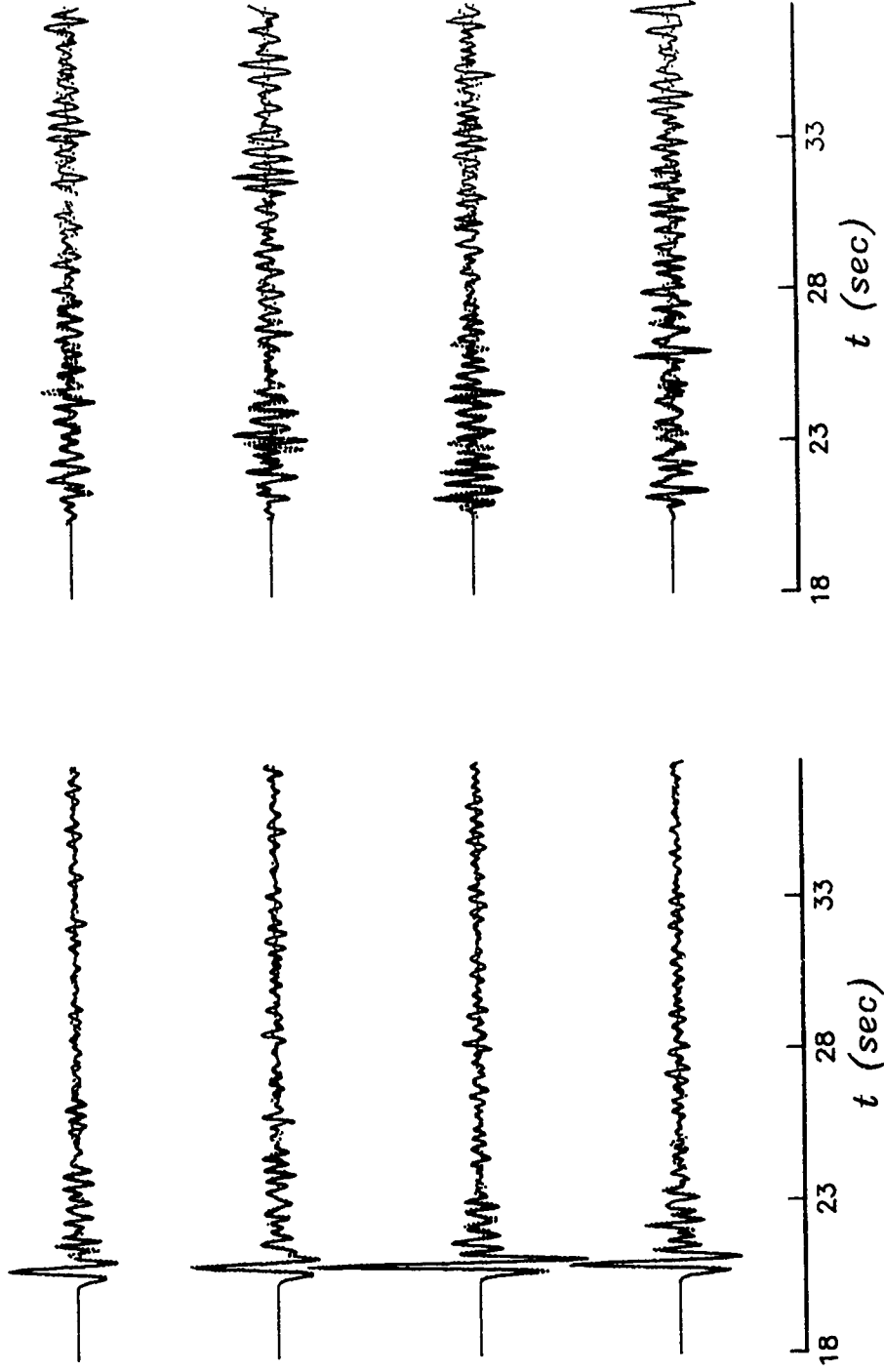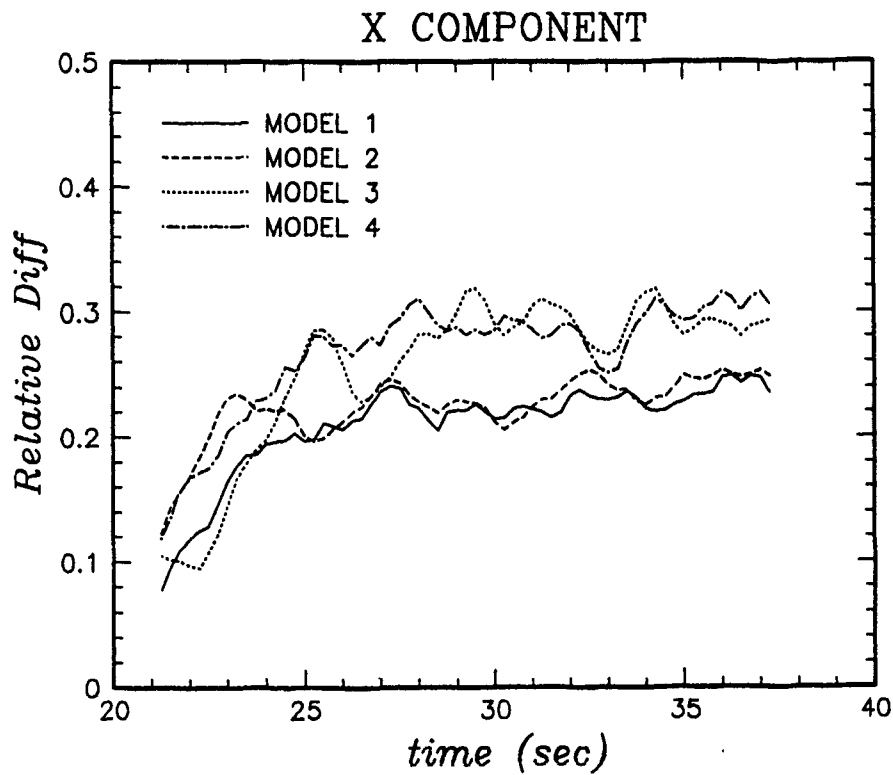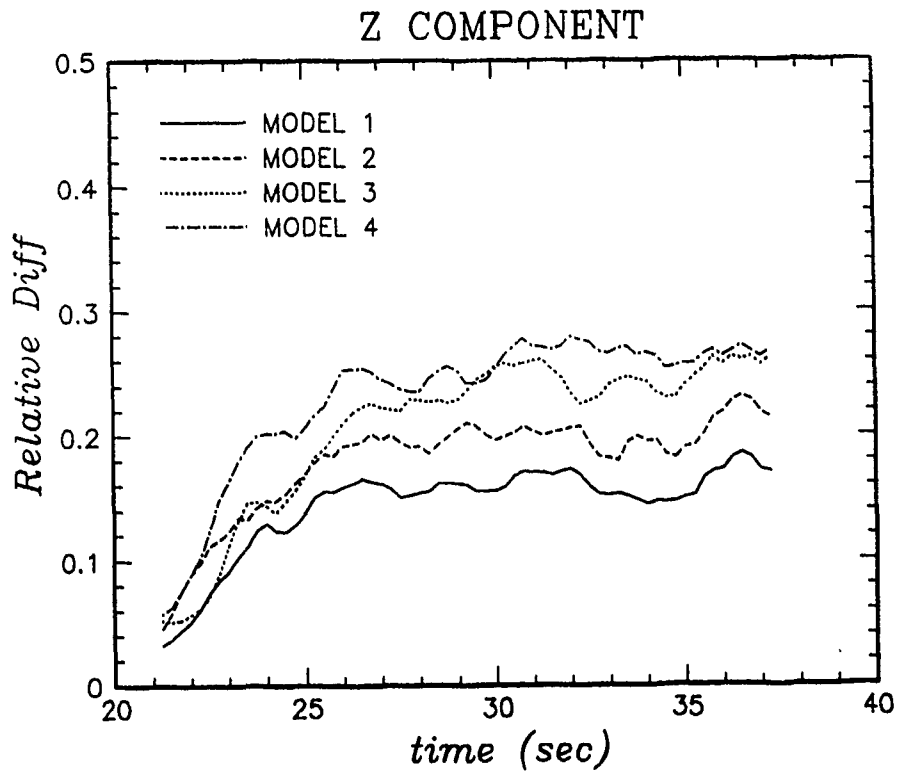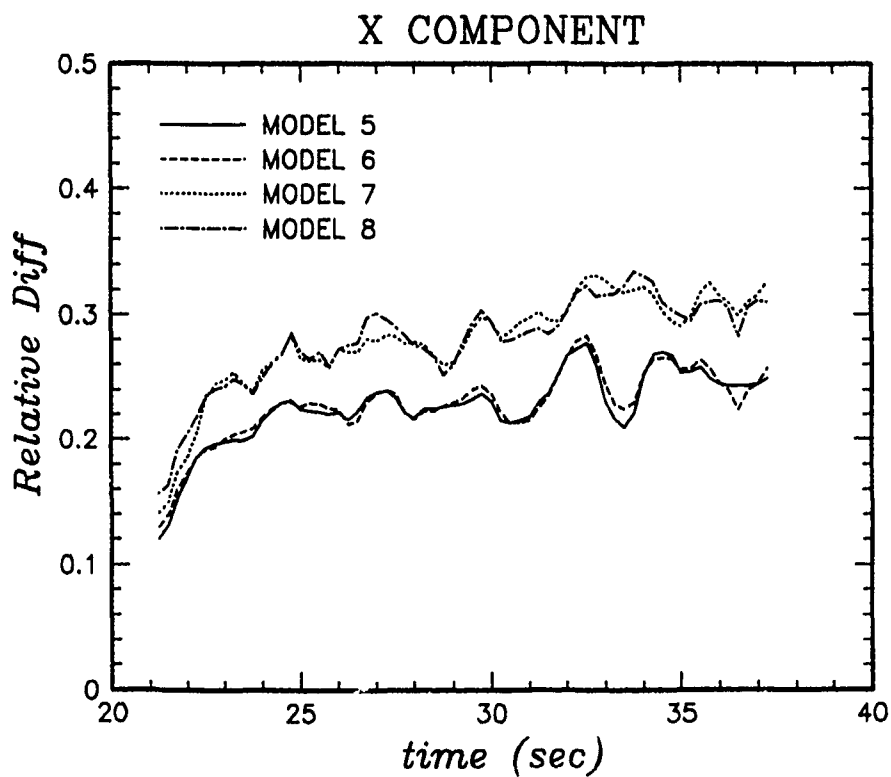Figure 22.   Model 8 sythetics for 4 evenly spaced receivers at a depth of 12.5 km.

44

Figure 23. Relative differences in the phase screen and finite difference synthetics for models 1-4.

Z COMPONENT

X COMPONENT
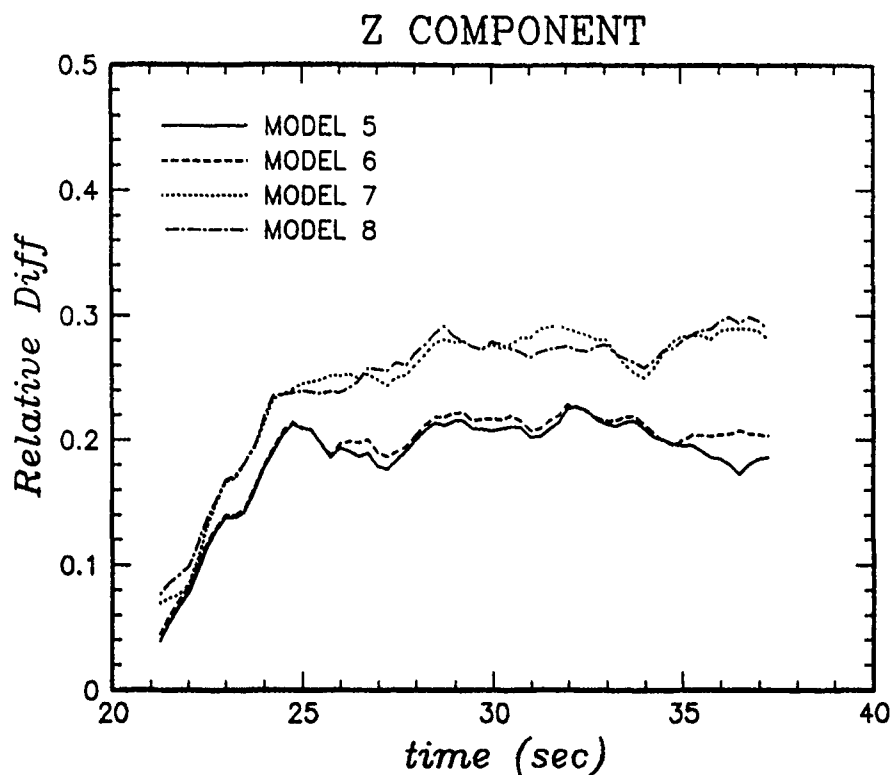
Figure 24.   **Relative differences in the phase screen and finite difference synthetics for models 5-8.**

46
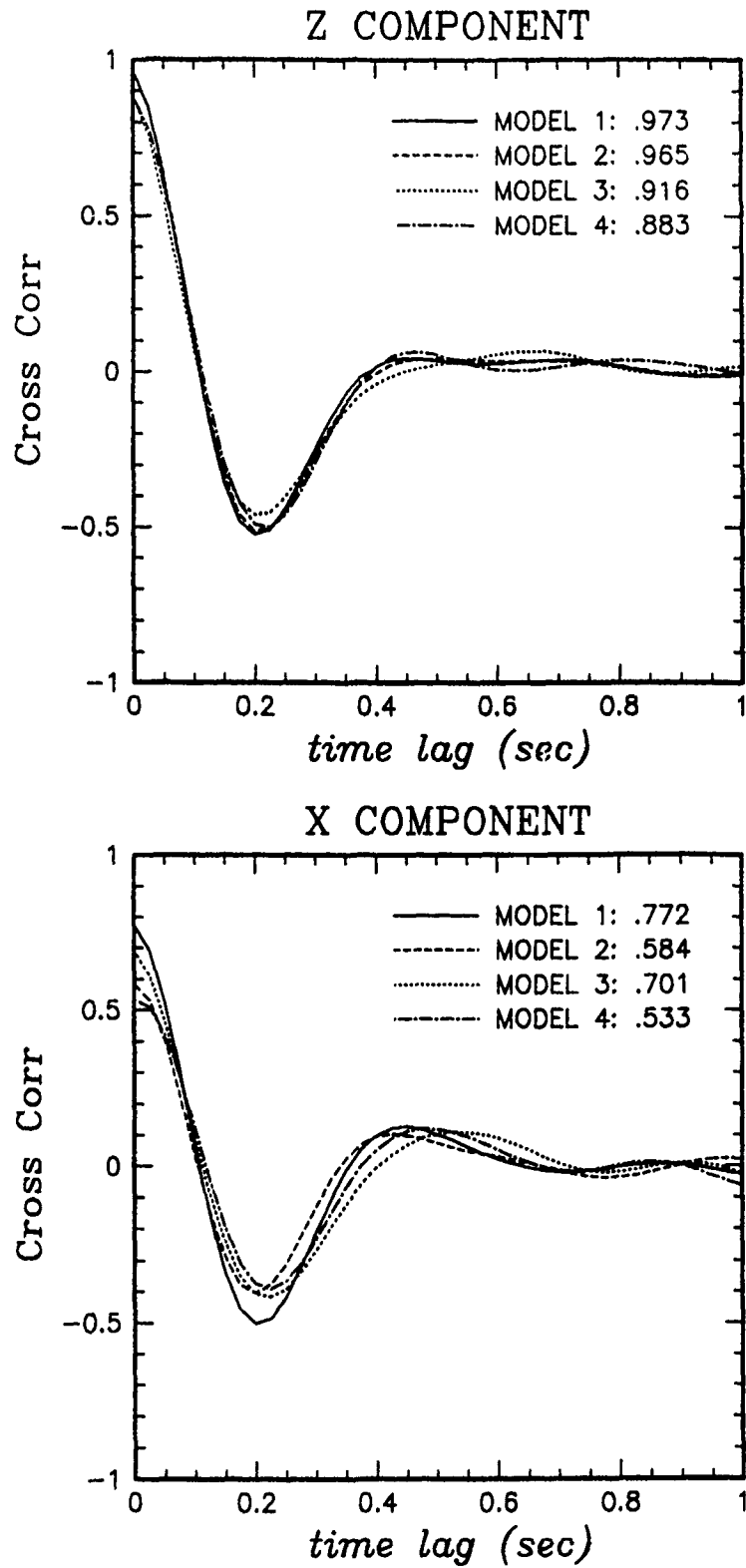
Figure 25. Cross correlations as a function of time lag between the phase screen and finite difference synthetics for models 1-4.

Z COMPONENT

MODEL 5: .983
MODEL 6: .982
MODEL 7: .897
MODEL 8: .903

X COMPONENT

MODEL 5: .408
MODEL 6: .364
MODEL 7: .367
MODEL 8: .308
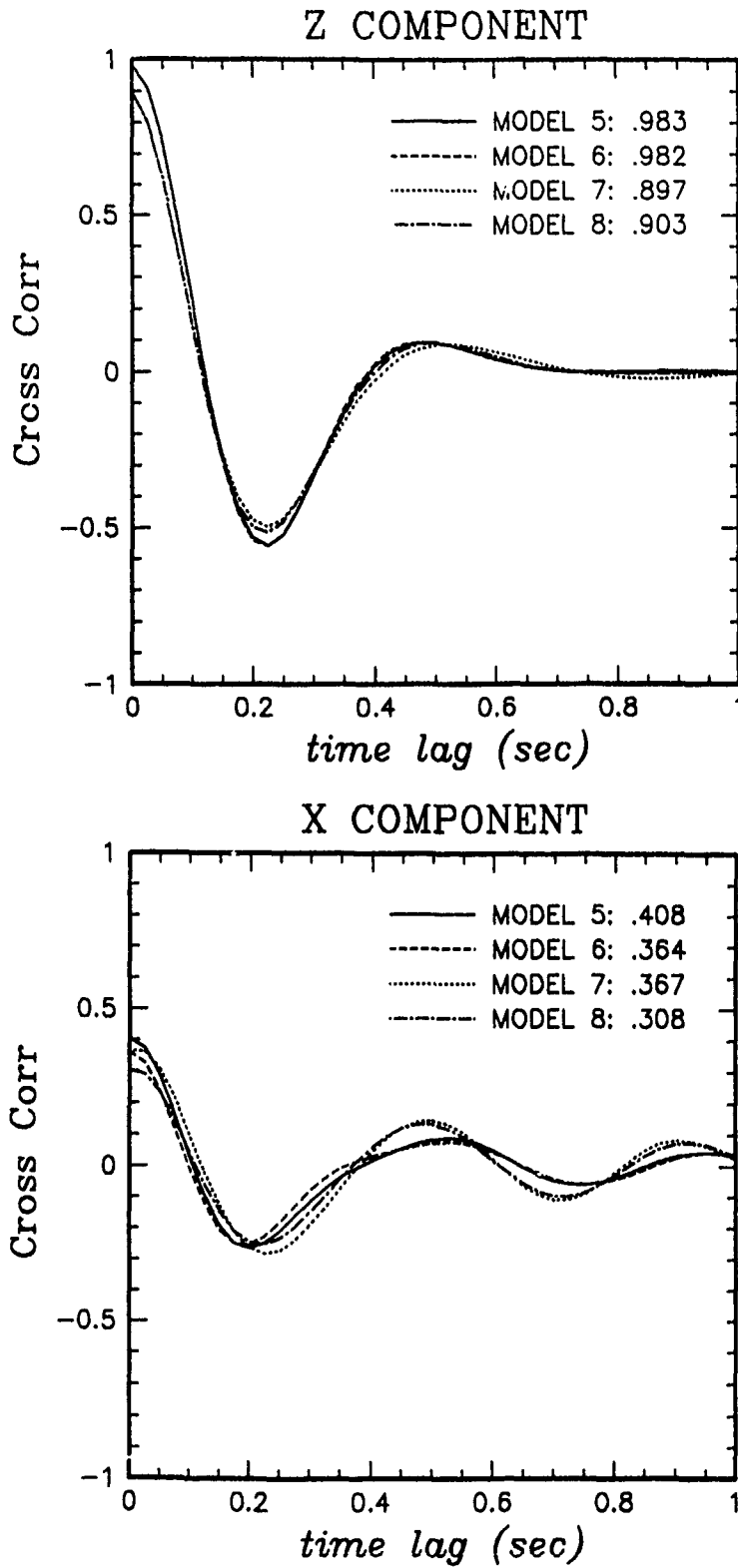
Figure 26. Cross correlations as a function of time lag between the phase screen and finite difference synthetics for models 5-8.
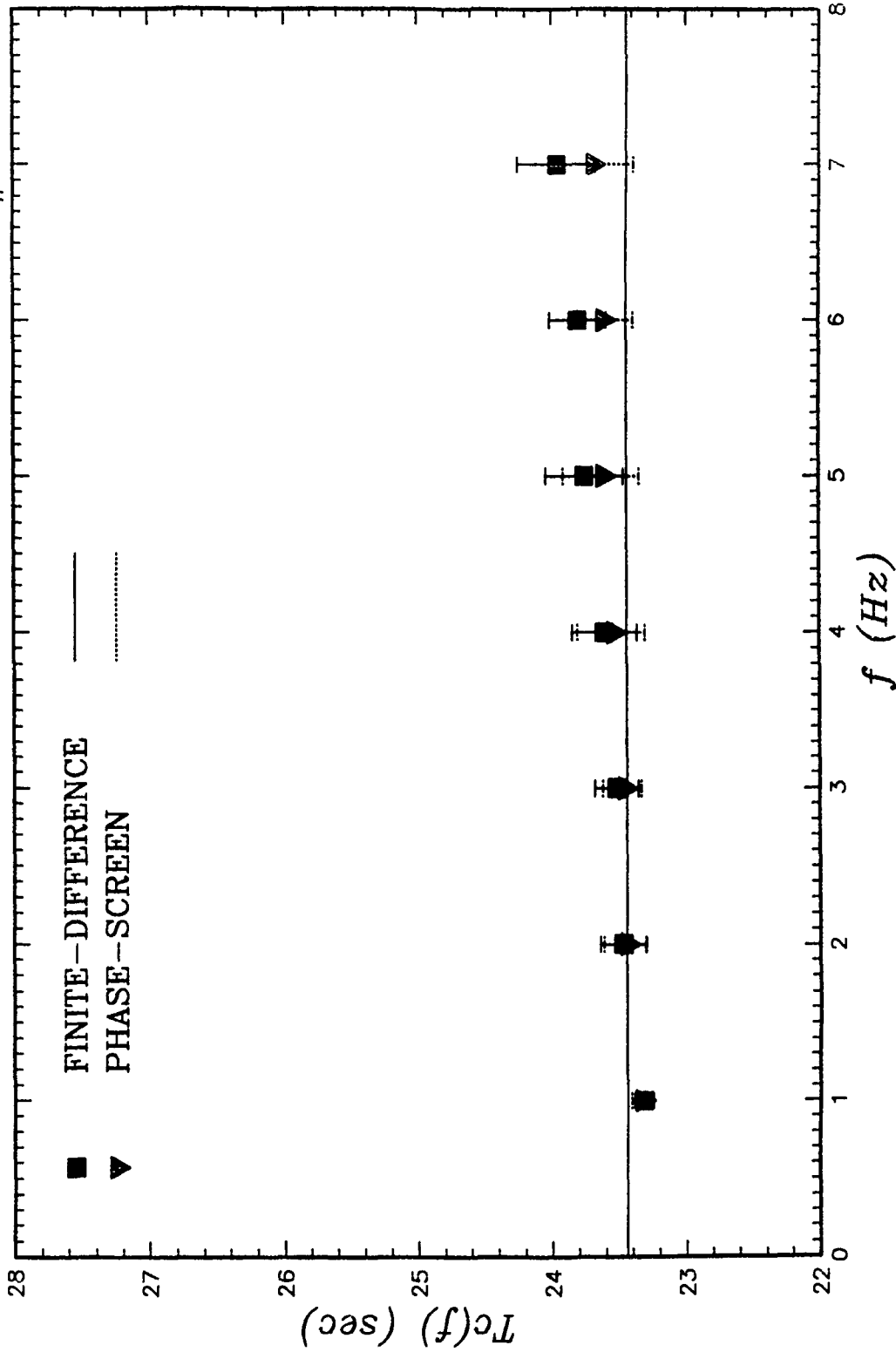
Figure 27. Average temporal energy centroids of bandpass filtered synthetics at $z = 0$ for model 1. The solid and dashed lines correspond to the averaged centroids of the unfiltered finite difference and phase screen synthetics, respectively.

Figure 28. Average temporal energy centroids of bandpass filtered synthetics at $z = 0$ for model 2.

50
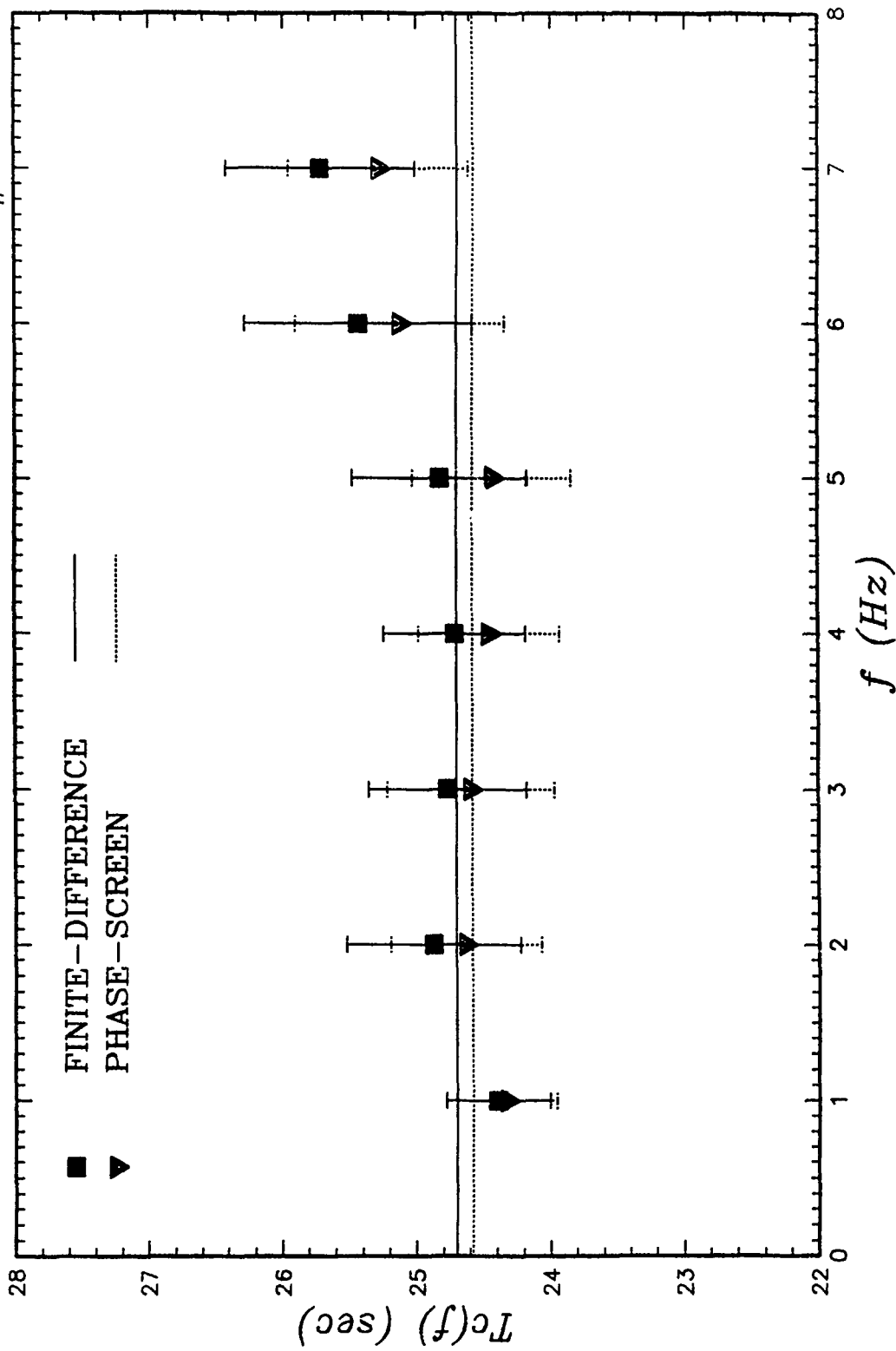
Figure 29. Average temporal energy centroids of bandpass filtered synthetics at $z = 0$ for model 3.
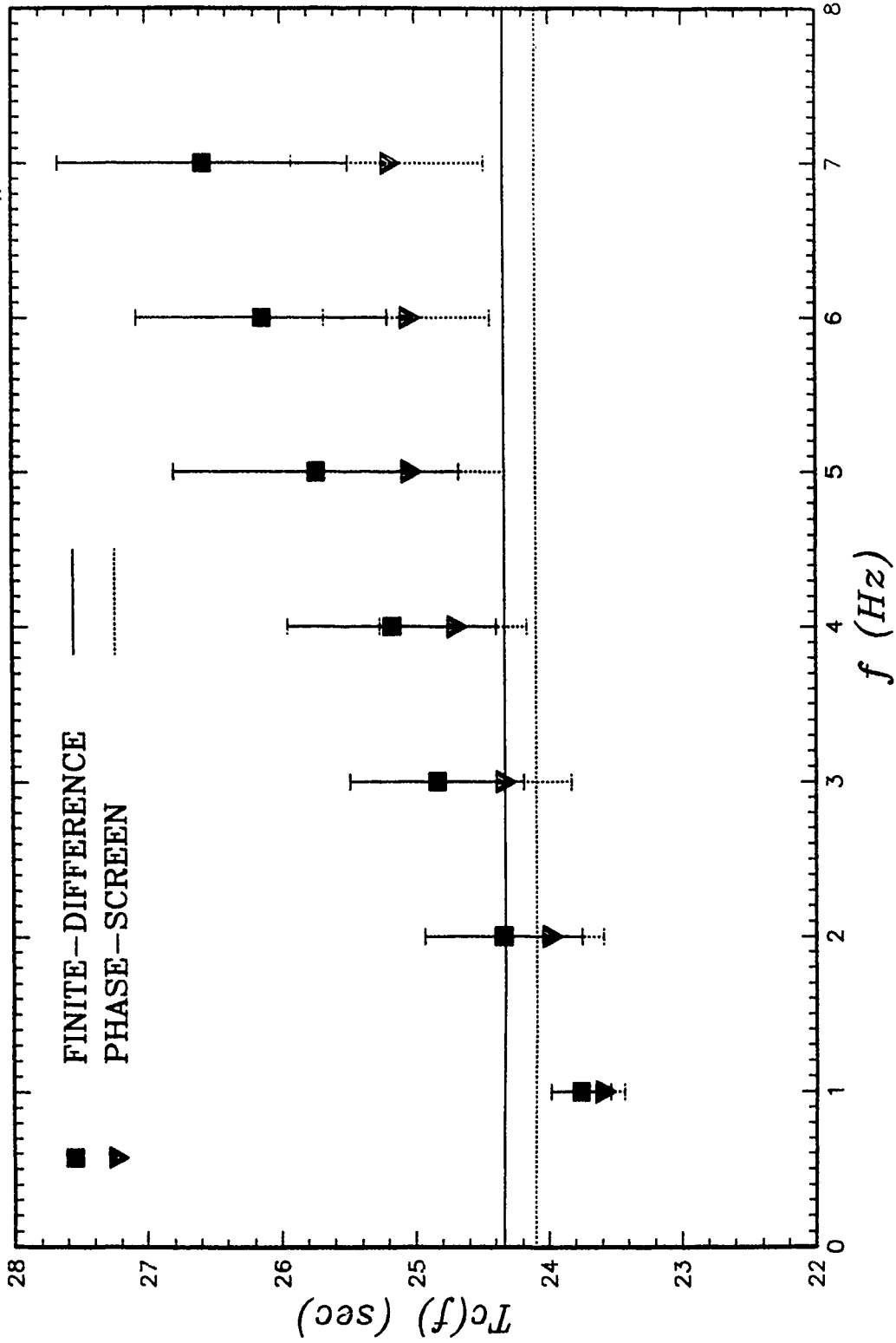
Figure 30. Average temporal energy centroids of bandpass filtered synthetics at $z = 0$ for model 4.

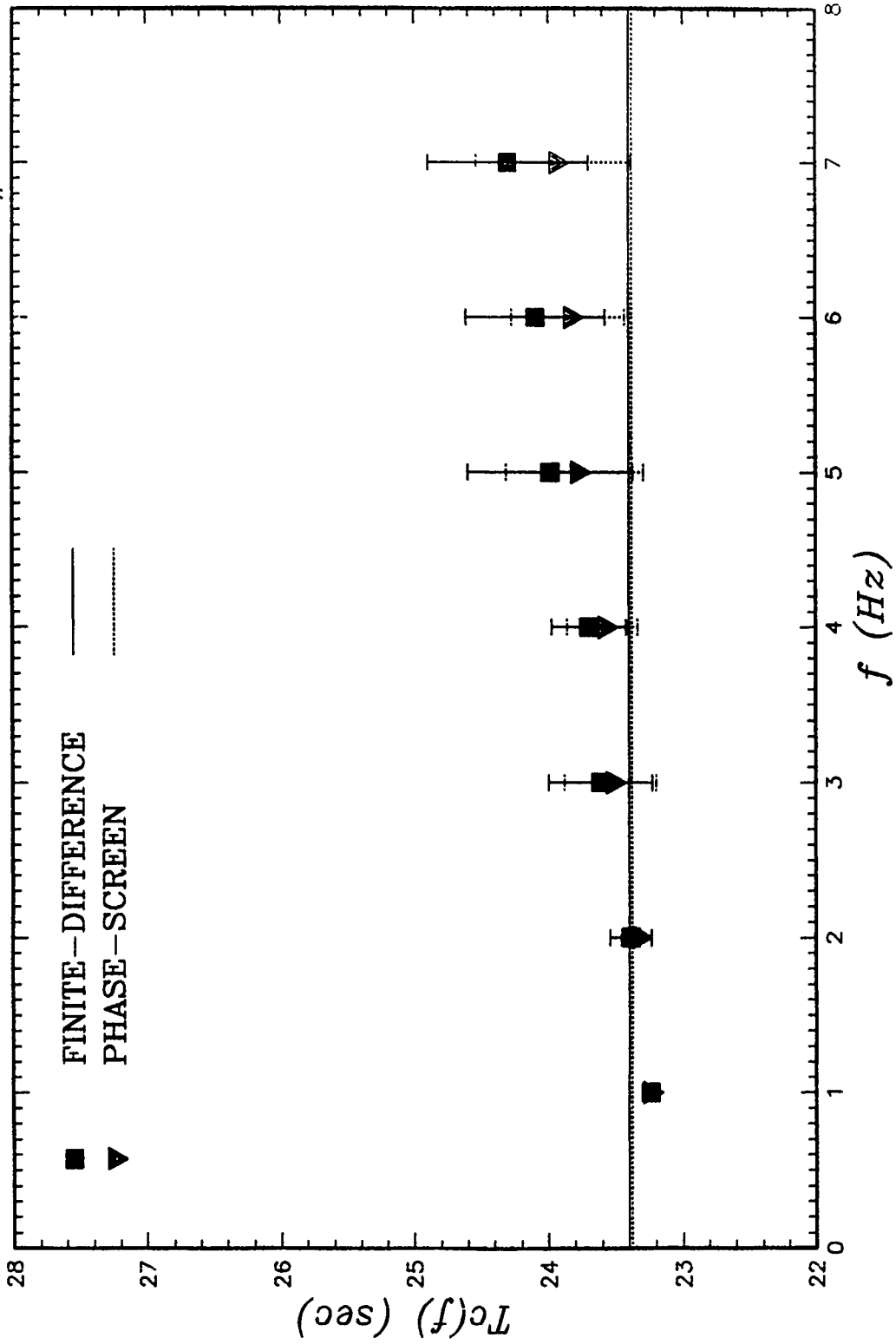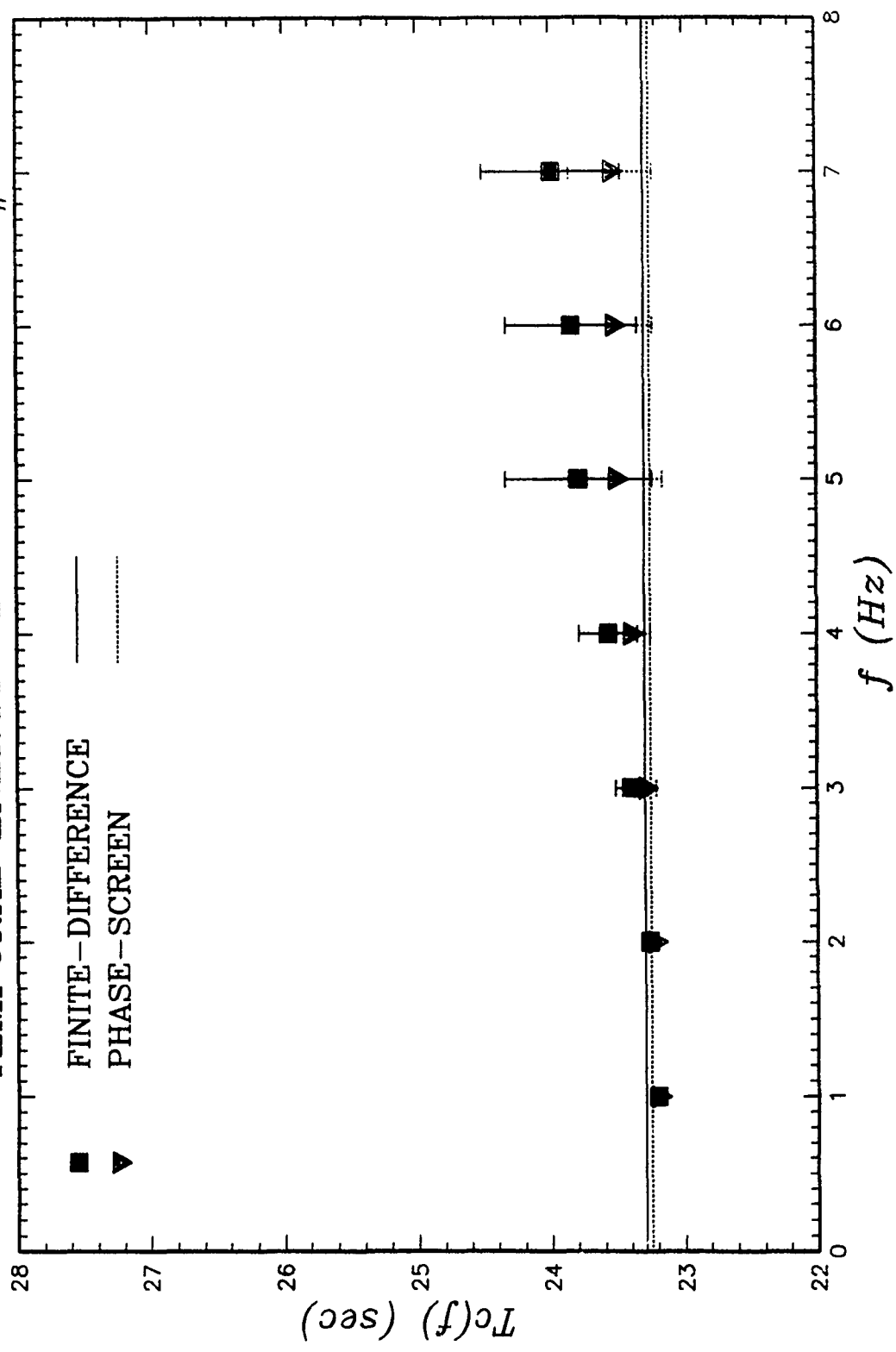**Figure 31.** Average temporal energy centroids of bandpass filtered synthetics at $z = 0$ for model 5.
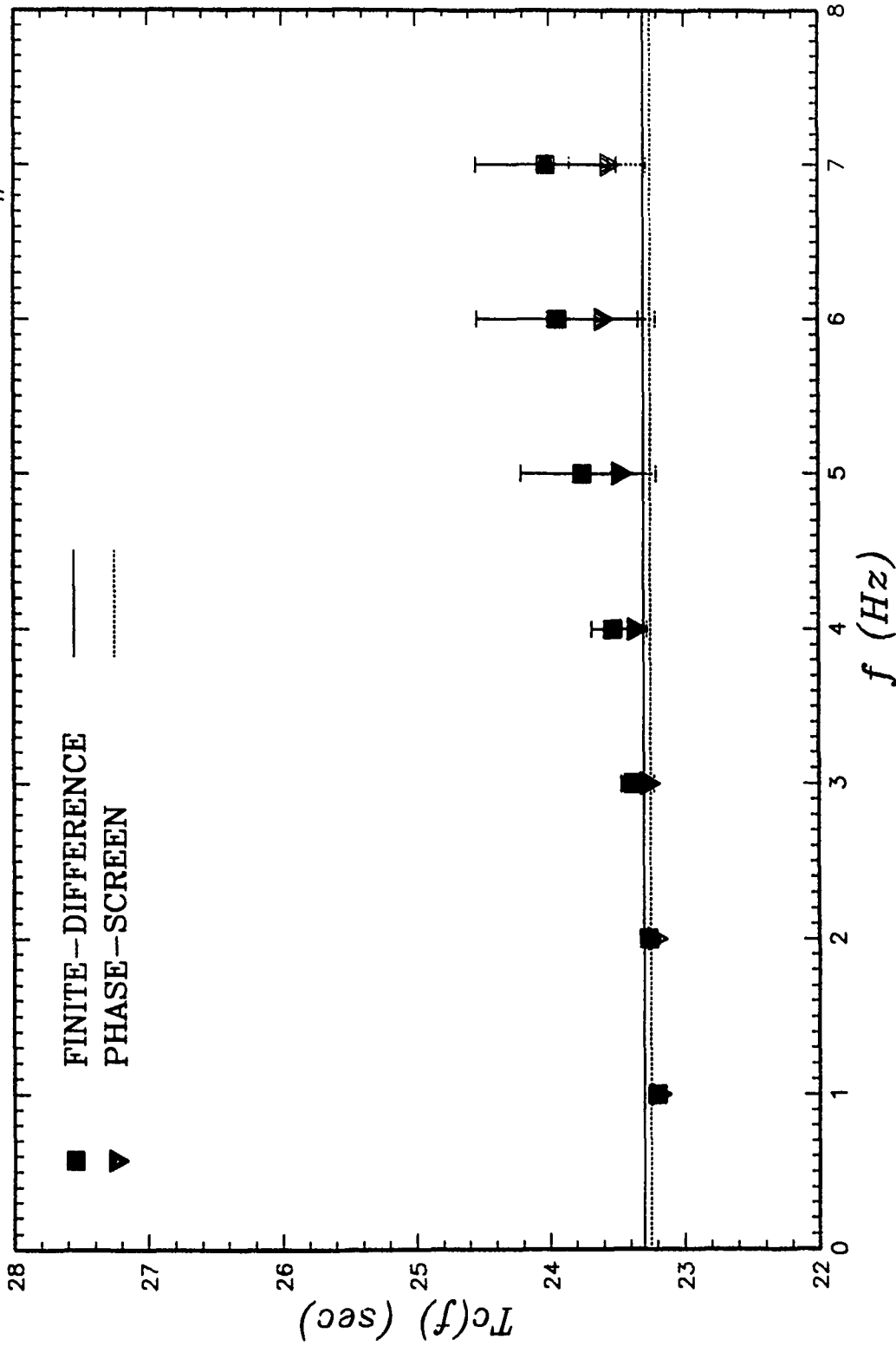
Figure 32. Average temporal energy centroids of bandpass filtered synthetics at $z = 0$ for model 6.
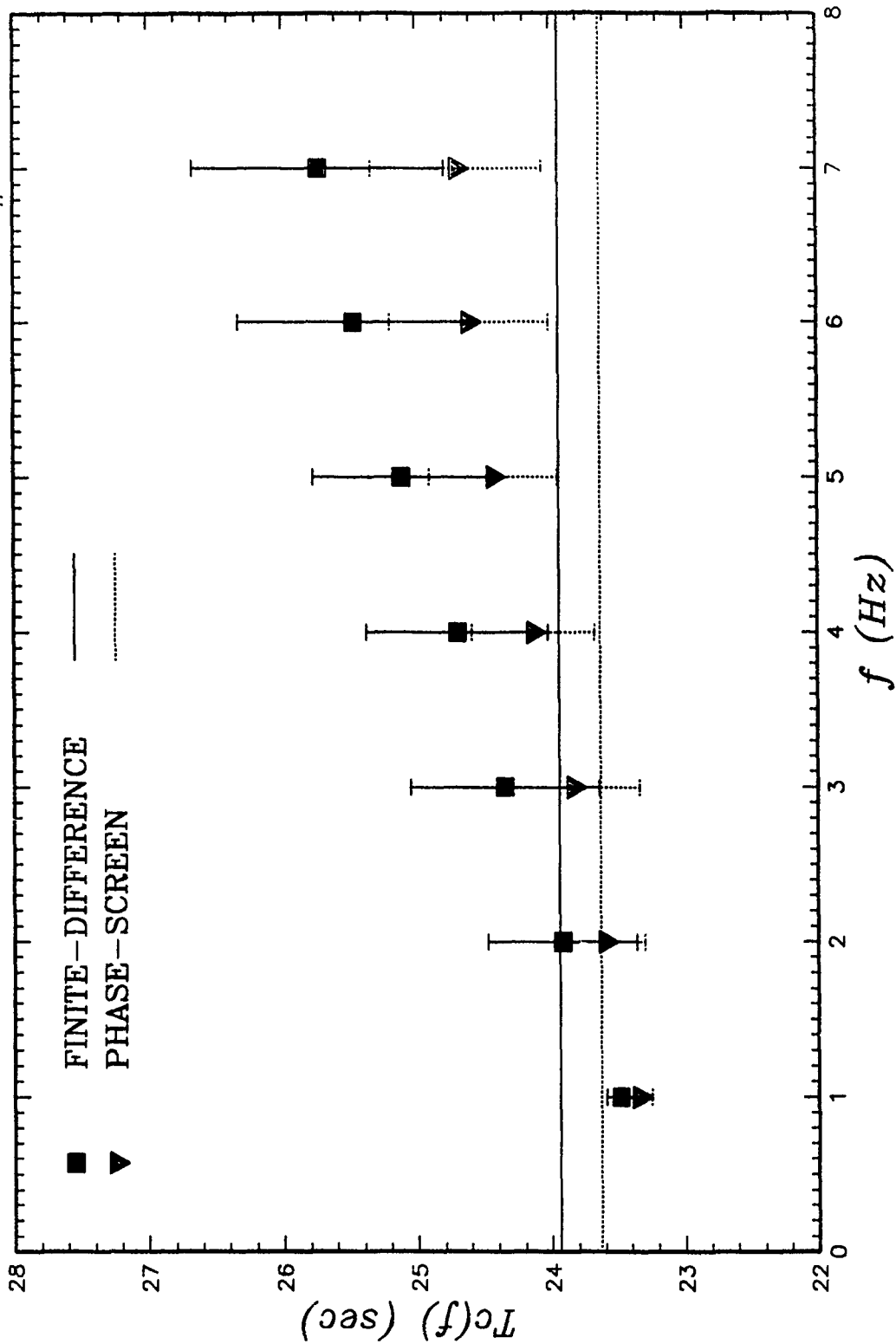
Figure 33. Average temporal energy centroids of bandpass filtered synthetics at $z = 0$ for model 7.
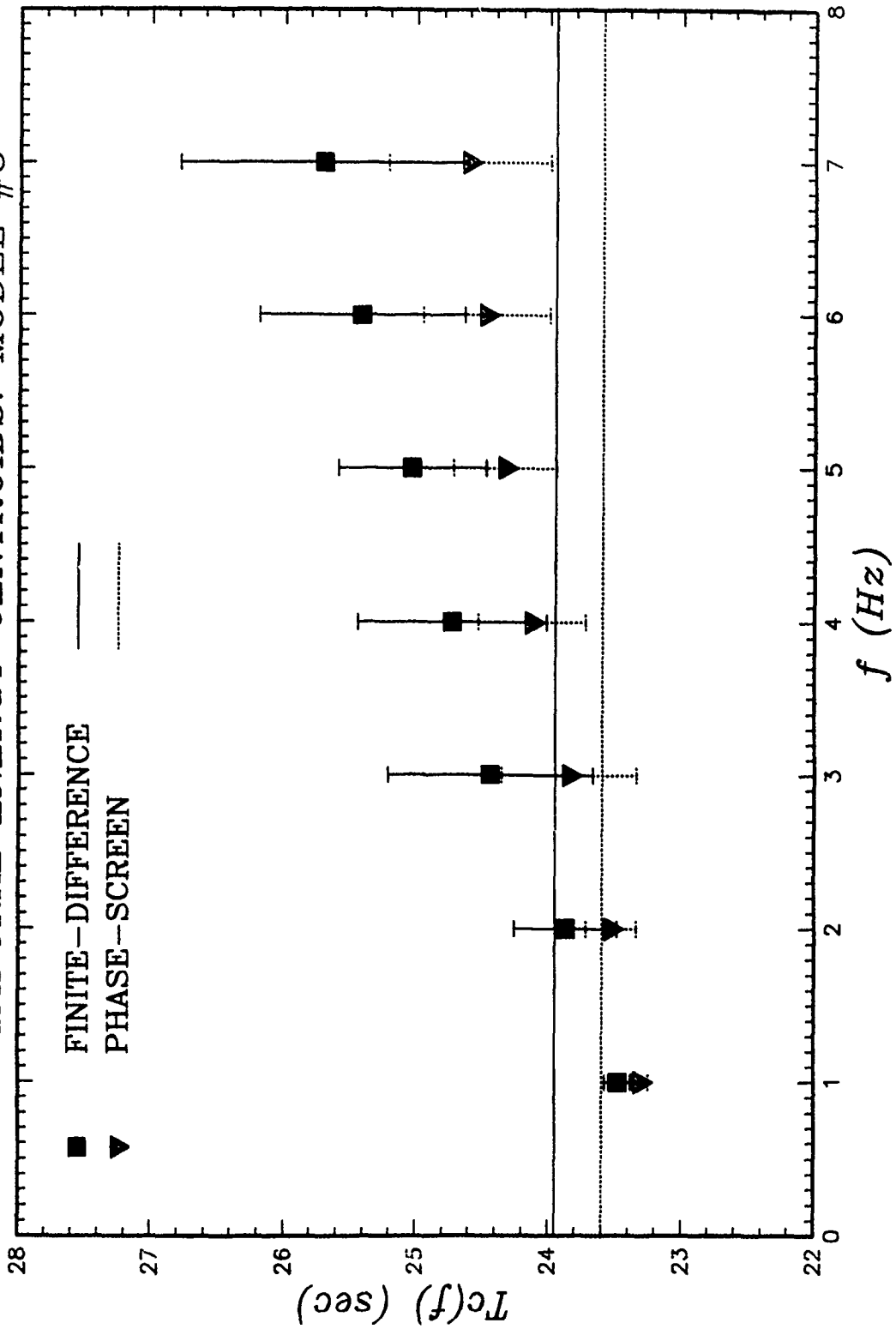
Figure 34. Average temporal energy centroids of bandpass filtered synthetics at $z = 0$ for model 8.
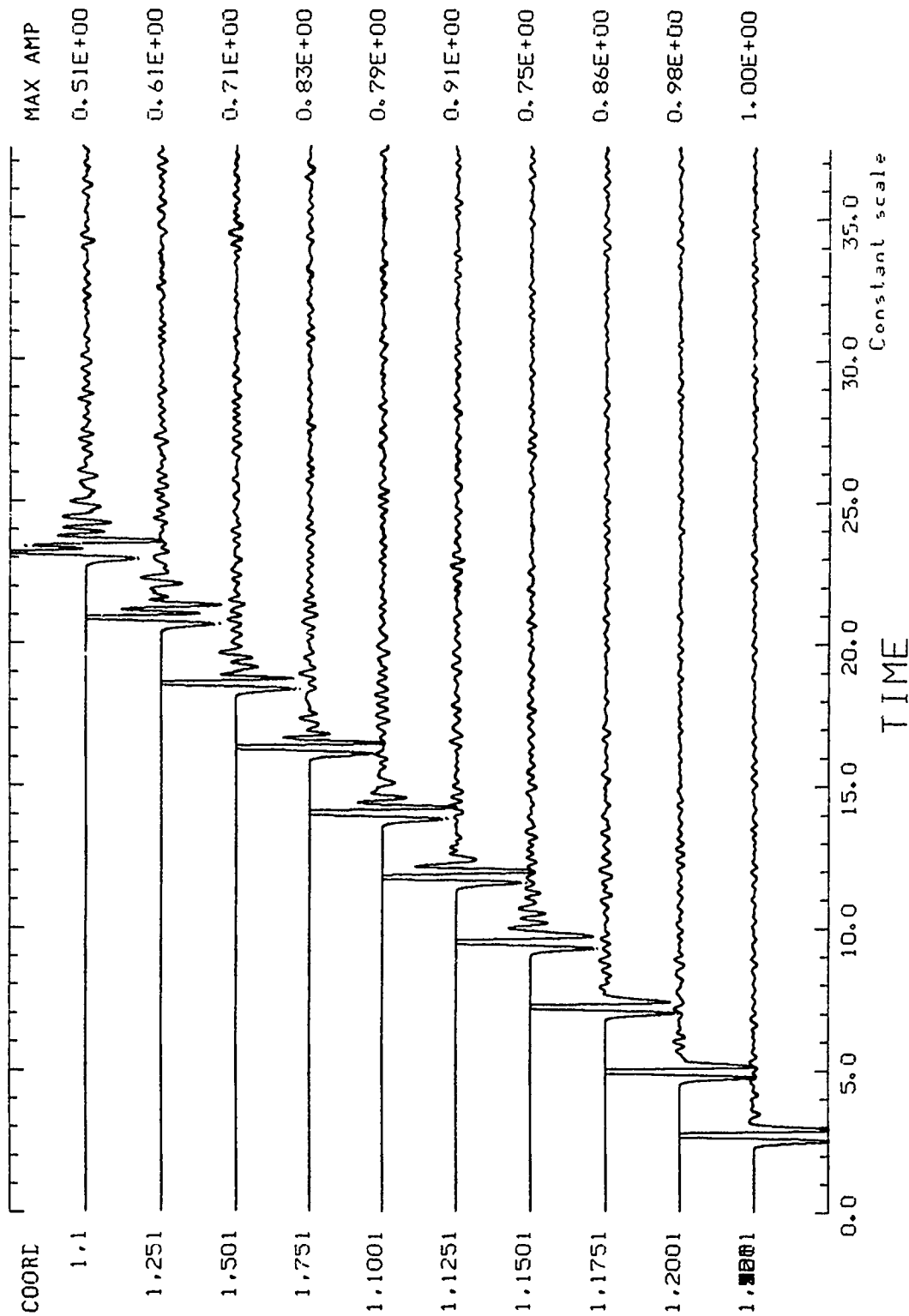
Figure 35. Comparison of synthetic seismograms using two different grid spacings. Shown here is the vertical component of the displacement vector (dominated by compressional waves) for model 1. The solid lines are from the finite difference simulations with 50 m grid spacings and the dashed lines are from the finite difference simulations with 25 m grid spacings.
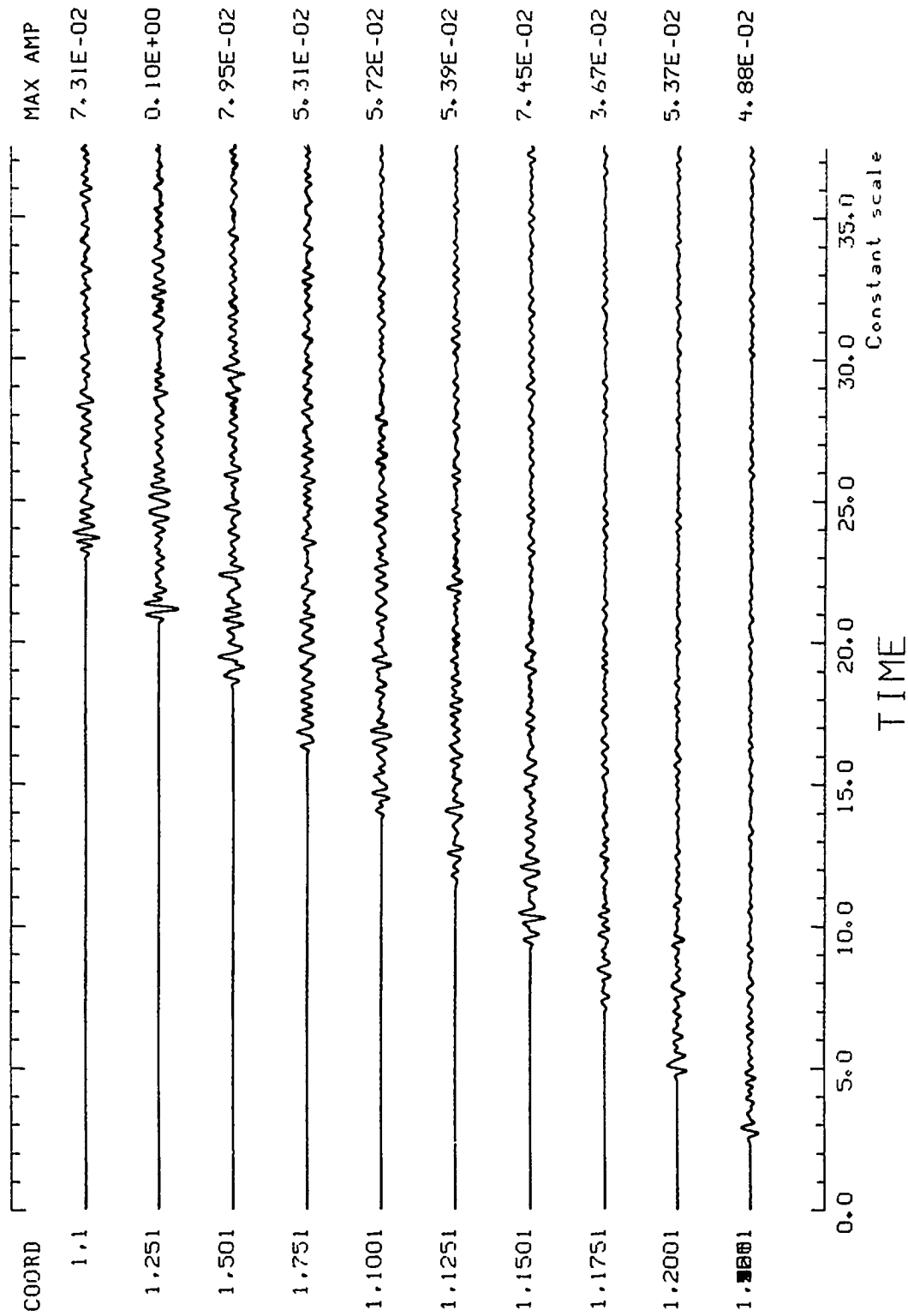
Figure 36. Comparison of synthetic seismograms using two different grid spacings. Shown here is the horizontal component of the displacement vector (dominated by shear waves) for model 1. The solid lines are from the finite difference simulations with 50 m grid spacings and the dashed lines are from the finite difference simulations with 25 m grid spacings.

FLUCTUATION ANALYSIS OF ELASTIC WAVES IN RANDOM MEDIA VIA PHASE SCREEN SIMULATIONS

M. D. Fisk
Mission Research Corporation
Santa Barbara, CA 93102
and
G. D. McCartor
Department of Physics
Southern Methodist University
Dallas, TX 75275-0175

Abstract

Phase screen simulations of vector wave propagation in elastic random media are applied to two independent studies of seismic wave scattering. In the first study, we analyze transmission fluctuations of incident P waves propagated through a two-dimensional version of Flatté and Wu's two-layer model of the crust and upper mantle under NORSAR. Transverse coherence functions (TCF's) of the log amplitude, phase and cross correlation, computed from vector wave simulations using 100 realizations, are compared to analytic and simulated TCF's based on the parabolic approximation to the scalar wave equation; the analytic results also assume the Rytov approximation. Our results show that the TCF's all agree reasonably well for velocity perturbations ≤ 0.5%, but the simulated TCF's (vector and scalar) are significantly different for perturbations ≥ 2%. The simulated vector wave also decorrelates over somewhat shorter spatial offsets than the simulated scalar wave for perturbations above 2%. In the second study, we examine the effect of random structure on the variances of the direct peak-to-peak P wave amplitude, and the rms amplitude of the transverse component in the velocity window between the P and S wave speeds. A large synthetic database of seismograms were generated at 25 km intervals out to 200 km for each of the eight random medium models considered. Our study shows that the relative variance of the scattered phase is far less dependent on the structure than the direct phase. The variance of the forward scattered P wave depends greatly on the strength of the large-scale heterogeneities.

1. INTRODUCTION

The complexity of the heterogeneities in the lithosphere and asthenosphere has led to a statistical characterization of the small-scale structure as random media. Wave propagation in random media is a relatively mature subject (e.g., Chernov,

59

1960; Tatarskii, 1961; Ishimaru, 1977; Flatté et al., 1979). Predominantly the theory has been applied to scalar wave propagation. Typically, weak scattering approximations are assumed to make the calculations tractable. For propagation in highly heterogeneous media, however, analytic solutions are often infeasible. Numerical simulations, such as finite difference calculations, are attractive in this case because they produce complete solutions to the elastic wave equation, and synthetic data may be generated at any gridpoint in the model (Frankel, 1989). Unfortunately, CPU time considerations often prohibit the use of finite difference techniques for many interesting problems in seismology. For the case of moderately strong scattering, a practical way to obtain the solution is to make a compromise between the analytical and numerical methods, e.g., by neglecting backscatter, numerical simulations may be performed in a fraction of the time required by full finite difference calculations.

In this paper, we consider two independent problems of seismic wave scattering in random media, whose analytic and finite difference solutions are currently infeasible. This is not to say that methods of these types could not be used if certain assumptions were made about the strength of the scattering, or the extent of the medium. However, the interesting features of these problems cannot be adequately probed with these solutions. In the first study, we analyze transmission fluctuations of incident plane P waves, propagated through a two-dimensional version of the model proposed by Flatté and Wu (1988) for the crust and upper mantle beneath NORSAR. Analytic solutions exist for this problem, however, the approximations involved lead to results that are valid only for weak fluctuations. We compare simulated and analytic solutions to assess the validity of the approximations assumed, and the usefulness of phase screen simulations for analyzing array data. In the second study, we examine the effect of random structure on the variances of direct and scattered phases. A large statistical ensemble of realizations (320 total samples of synthetic seismograms at 25 km intervals out to 200 km for each of eight models) was generated to compute statistically reliable variances. It is the first study of this type of which we are aware. The details of these studies are contained in sections 2 and 3. First, we briefly describe the computational technique used for this work.

1.1. The Phase Screen Method

The phase screen method is a rapid forward propagation algorithm, which exploits the benefits of analytic approximations and numerical simulation. Phase screen methods for scalar waves have been used in previous propagation studies of starlight through the atmosphere (Ratcliffe, 1956; Mercier, 1962; Filice, 1984), radio signals through the ionosphere (Buckley, 1975; Bramley, 1977; Knepp, 1983), acoustic waves in the ocean (Flatté et al., 1979), and P waves in the crust (Haddon and Husebye, 1978). Simulations for scalar waves in three dimensions have been performed by

Filice (1984) and Martin and Flatté (1988). Recently, Fisk and McCartor (1989,1991) have developed a phase screen method which treats vector elastic waves, including P/S conversion. The algorithm allows for simulation of seismic wave propagation in 3-D heterogeneous media. Like the finite difference method, this method may be used to generate synthetic data at any gridpoint.

Common to ray theory methods (e.g., Aki and Richards, 1980), the phase screen method makes use of the following facts: (1) To first order at high frequency the P and S wave displacements, expressed as the curl-free and divergence-free portions of the total displacement respectively, decouple; and (2) to first order the propagation of the waves depend only on the local P and S wave velocities, which act to retard or advance the phases of the wavefronts. For problems which meet these criteria, the heterogeneous medium depicted in Figure 1(a) may be replaced with a homogeneous medium and a set of phase screens, as shown in Figure 1(b). Based on the first fact, and working with single-frequency plane waves for now, the initial P and S waves at $z = 0$ are independently propagated to $z = \Delta z$ according to the uniform elastodynamic equation, using the average wave velocities. The affect of variations in the local velocities is treated by multiplying the S and P waves by position dependent phase factors at screen 2. The spacing of the screens is determined such that the phase factors may be computed from geometrical optics. Below, we describe how random realizations of the phase factors are computed.

The wavefronts of the P and S waves become distorted by the phase factors, and thus no longer satisfy the curl-free and divergence-free conditions. Hence, if these waves are decomposed onto a complete set of forward propagating P and S plane waves that do satisfy these conditions, P/S conversion occurs. The procedure may now be repeated, inserting phase screens for larger values of z, to propagate the new expressions for the P and S wave displacements further. If synthetic data in the time domain are desired, the single-frequency results may be computed at a discrete set of frequencies, and then convolved with the frequency spectrum of the time source function. (Detailed formulas of the method outlined here have been given by Fisk and McCartor (1989,1991) and Fisk et al. (1991).)

The method has been compared, with considerable success, to other calculations. Fisk and McCartor (1991) compared the results of the phase screen method to an "exact solution" of an elastic wave in a 2-D laterally-layered structure. (By "exact" we mean that there were no fundamental approximations made to solve the equation of motion and satisfy the boundary conditions. The solution could not be written in closed form, however, but may be numerically determined to any desired precision.) Even for wavelengths on the order of the length scale of the layers and velocity variations of 5%, the comparison was excellent. In a separate study, Fisk et

al. (1991) compared phase screen and finite difference calculations for elastic waves in 2-D random media. Again, the comparison was quite favorable. In addition, it was shown that the phase screen algorithm is roughly two orders of magnitude faster than a second-order finite difference scheme for two-dimensional problems.

2. TRANSMISSION FLUCTUATIONS

Transmission fluctuations of direct P arrivals have been analyzed at LASA and NORSAR by Aki (1973), Capon (1974), Bertreussen et al. (1975) and others to deduce the statistical properties of the crust and upper mantle beneath the arrays. Assuming a single-layer Gaussian medium, comparisons of theoretical TCF's of the log amplitude and phase with data, provided estimates of the depth, correlation length and rms velocity perturbations of the crust. The TCF's measure how the waveform decorrelates as a function of the spatial offset across an array, due to propagation through the random structure.

The analytic techniques to compute TCF's were originally developed by Chernov (1960), Tatarskii (1971), Munk and Zachariasen (1976), Ishimaru (1978), and Flatté et al. (1979). Flatté and Wu (1988) extended the theory to compute angular coherence functions (ACF's), which describe the coherence of the wavefield as a function of the angle of incidence. Using the additional information in the ACF's, they found that the single-layer Gaussian medium model does not accurately fit the data at NORSAR. They proposed a two-layer power-law medium model which sufficiently predicts the observations.

While the analytic calculations provide elegant closed form expressions for the coherence, they often assume the scalar wave, Rytov and parabolic approximations. Wu and Flatté (1990) have noted that their analytic results are valid for only sufficiently weak fluctuations. In fact, by assuming the Rytov approximation, the normalized TCF's are independent of the magnitude of the rms velocity perturbations. Intuitively, the coherence of the wave cannot be entirely independent of the scattering strength of the medium. Wu and Flatté (1990) suggested that numerical simulation is needed to determine when the weak fluctuation (Rytov) approximation no longer applies.

The Rytov approximation assumes that gradients in the wave fluctuations are small. Thus, as the frequency of the wave increases, the validity of the approximation decreases. Using a phase screen method based on the parabolic approximation to the scalar wave equation, Flatté et al. (1988) looked at the behavior of the TCF's with increasing frequency. They found that at 2 Hz, their simulated and analytic results were in agreement. For frequencies greater than 4 Hz, the log amplitude TCF's

differed dramatically. Alternatively, as the strength of the perturbations increase, for fixed frequency, the analytic results are also expected to break down. The scalar wave and parabolic approximations are also apt to break down in this case since moderately strong heterogeneities are likely to generate obliquely scattered waves and P/S conversion.

At the time, Wu and Flatté (1990) noted that the phase screen method they used provided the only practical means to numerically simulate the 3-D problem. Since then, Fisk and McCartor (1991) have developed a phase screen method for vector wave propagation. We compare simulated TCF's based on the method for vector waves to analytic and simulated results based on the parabolic approximation to the scalar wave equation. We perform this comparison for a 2-D version of the model proposed by Flatté and Wu (1988). Although this study could be performed for the 3-D model, for the purpose of assessing the assumptions involved and understanding the scattering effects, the 2-D model is adequate. To begin, we present the analytic calculation. The details of the simulation and the model of the crust and upper mantle follow.

2.1. The Analytic Calculation

Following the derivation of the TCF's by Wu and Flatté (1990), it is assumed that the propagation of the initial P arrival is governed by the scalar wave equation

$$\left(\nabla^2 + \frac{w^2}{\alpha(\mathbf{x})^2}\right) U = 0, \tag{1}$$

where w is the frequency, $\alpha(\mathbf{x})$ is the local P wave speed, and U is the single-frequency P wave. For weak velocity perturbations, eq. (1) may be written as

$$\left(\nabla^2 + k^2\right) U = -2k^2 \delta n(\mathbf{x}) U, \tag{2}$$

where $k = w/\bar{\alpha}$, $\bar{\alpha}$ is the average wave speed, and $\delta n = \bar{\alpha}/\alpha - 1 \simeq -\delta\alpha/\bar{\alpha}$. Expressing the wavefield as $U = U_0\, e^\psi$, where U_0 is taken to be the solution of the homogeneous wave equation, one obtains

$$\left(\nabla^2 + k^2\right)(U_0\psi) = -U_0(\nabla\psi \cdot \nabla\psi + 2k^2\delta n). \tag{3}$$

The solution may be written as an integral equation, and assuming $|\nabla\psi|$ is small, it takes the form

$$\psi(\mathbf{x}) = 2k^2 \, U_0(\mathbf{x})^{-1} \int_V d^N x' \, G(\mathbf{x}, \mathbf{x}') \, U_0(\mathbf{x}') \, \delta n(\mathbf{x}'), \qquad (4)$$

where G is the Green's function of the homogeneous wave equation, and N is the number of spatial dimensions. The assumption which neglects the nonlinear term $\nabla\psi \cdot \nabla\psi$ is known as the Rytov approximation.

This expression may be further simplified if the scattering is predominantly in the forward direction, *i.e.* by assuming the parabolic approximation. Let z be the direction of forward propagation and $\mathbf{r}_T$ be the vector of transverse coordinates. Let the Green's function be expressed in the form

$$G(\mathbf{x}, \mathbf{x}') = \int d^{N-1} K_T \, \tilde{G}(\mathbf{K}_T; z - z') \, e^{i\mathbf{K}_T \cdot \mathbf{r}_T}, \qquad (5)$$

where $\tilde{G}(\mathbf{K}_T; z - z')$ is the Fourier transform *w.r.t.* the transverse coordinates $\mathbf{r}_T$ of G. For small-angle propagation in N dimensions

$$\tilde{G}(\mathbf{K}_T; z - z') = \frac{i}{2(k^2 - K_T^2)^{1/2}} \, e^{i(k^2 - K_T^2)^{1/2}(z - z')} \simeq \frac{i}{2k} \, e^{i(k - K_T^2/2k)(z - z')}. \qquad (6)$$

Also, assuming a normally incident plane wave,

$$U_0(\mathbf{x})^{-1} U_0(\mathbf{x}') = e^{-ik(z - z')}. \qquad (7)$$

To complete the analysis, the fluctuations δn are characterized by their power spectrum $P_n(\mathbf{K}; z)$ and rms perturbation σ as

$$\langle \delta n(\mathbf{x}) \delta n(\mathbf{x}') \rangle = \sigma^2 \int d^N K \, P_n(\mathbf{K}; z) \, e^{i\mathbf{K} \cdot (\mathbf{x} - \mathbf{x}')}. \qquad (8)$$

The z dependence represents the possibility that the power spectrum may vary with depth. Now let $\psi = u + i\phi$, where u is the log amplitude and ϕ is the phase of the fluctuating wavefield. Using the expressions above, the TCF's for a 2-D medium are given by

$$\langle u(r_T) u(0) \rangle = 2\pi k^2 \sigma^2 \int_0^h dz \int dK_T \, P_n(K_T, 0; z) \, \sin^2(K_T^2 z/2k) \, \cos(K_T r_T) \qquad (9)$$

$$\langle \phi(r_T)\phi(0)\rangle = 2\pi k^2 \sigma^2 \int_0^h dz \int dK_T \ P_n(K_T, 0; z) \ \cos^2(K_T^2 z/2k) \ \cos(K_T r_T) \quad (10)$$

$$\langle u(r_T)\phi(0)\rangle = \pi k^2 \sigma^2 \int_0^h dz \int dK_T \ P_n(K_T, 0; z) \ \sin(K_T^2 z/k) \ \cos(K_T r_T). \quad (11)$$

In these expressions, $\mathbf{K} = (K_T, K_z)$ and h is the depth of the structure. The angled brackets denote an ensemble average over all possible realizations of the medium. As Wu and Flatté (1990) have noted, the wavefield fluctuations depend only on the D.C. component of the heterogeneities in the direction of propagation, *i.e.* on the power spectrum with $K_z = 0$. Thus the results are insensitive to the small-scale structure in the vertical direction. Typically, the TCF's are normalized such that

$$\langle u(r_T)u(0)\rangle_N = \frac{\langle u(r_T)u(0)\rangle}{\langle u(0)^2\rangle} \quad (12)$$

$$\langle \phi(r_T)\phi(0)\rangle_N = \frac{\langle \phi(r_T)\phi(0)\rangle}{\langle \phi(0)^2\rangle} \quad (13)$$

$$\langle u(r_T)\phi(0)\rangle_N = \frac{\langle u(r_T)\phi(0)\rangle}{\sqrt{\langle u(0)^2\rangle\langle \phi(0)^2\rangle}}. \quad (14)$$

These functions are clearly independent of the rms wave speed perturbation σ, which may be traced back to the Rytov approximation. We will return to these results momentarily. First, we describe how the simulated results were obtained.

2.2. Phase Screen Simulations

The phase screen method based on the parabolic approximation to the scalar wave equation has a great deal of similarity to the calculation just described. Propagation between any consecutive pair of screens is accomplished by using the parabolic free-field Green's function in wavevector space. Thus the wavefield at $z' = z + \Delta z$ in terms of the wavefield at z is given by

$$\tilde{U}(K_T, z') = \tilde{U}(K_T, z) \exp\left[i(k - K_T^2/2k)\Delta z\right] \quad (15)$$

This expression is now Fourier transformed *w.r.t.* the transverse component of the wavevector, to obtain $U(\mathbf{r}_T, z')$. The affect of the wave speed perturbations are treated by multiplying this expression by the phase factor $\exp[i\phi(\mathbf{r}_T)]$, where

$$\phi(\mathbf{r}_T) = k \int_z^{z+\Delta z} dz' \, \delta n(\mathbf{r}_T, z'). \tag{16}$$

Now inverse Fourier transform $U(\mathbf{r}_T, z') \exp[i\phi(\mathbf{r}_T)]$ to obtain $\tilde{U}(\mathbf{K}_T, z'_+)$ on the other side of the screen. The process may be repeated to propagate further. Once the wave has been propagated to the surface, TCF's may be computed numerically.

The fundamental difference between this approach and the analytic calculation is the treatment of diffraction effects. The phase screen solution divides the medium into segments such that the geometrical optics regime applies between consecutive screens. Thus instead of multiplying the free-field solution by an amplitude and a phase, $\exp(u + i\phi)$, it is multiplied by only a phase, $\exp(i\phi)$. Diffraction effects (variations in the amplitude) are accumulated as the wave propagates through many screens. The diffracted wavefield in this case may depend nontrivially on the strength of the perturbations. The Rytov solution, on the other hand, computes the diffraction effects over the full propagation distance in a single step. Unfortunately, to do so, the Rytov approximation leads to a dependence on the rms perturbations that is simply a multiplicative constant.

The phase screen method for vector waves has two additional features. First, P/S conversion is treated as described in the first section of the paper. Second, the S and P waves are propagated between the screens using free-field Green's functions of the form $\exp\left[i(k^2 - K_T^2)^{1/2}\Delta z\right]$, where $k = w/\bar{\alpha}$ for the P wave and $k = w/\bar{\beta}$ for the S wave. The parabolic Green's function may be recovered from this expression by expanding the argument of the exponential to first order for $K_T \ll k$.

To generate random realizations of the phase screens, we relate the power spectrum of the phase, denoted $P_\phi(K_T)$, to the power spectrum of the perturbations $P_n(K_T, K_z)$ (Knepp, 1983; Martin and Flatté, 1988) via

$$P_\phi(K_T) \propto P_n(K_T, 0). \tag{17}$$

If the spectra are normalized such that

$$1 = \int dK_T \, P_\phi(K_T) = \int dK_T dK_z \, P_n(K_T, K_z), \tag{18}$$

66

then the variance of the phase is given by

$$\sigma_\phi^2 = \sigma^2 k^2 \Delta z \int dK_T \, P_n(K_T, 0). \tag{19}$$

Each phase screen is created by filtering computer-generated Gaussian random numbers by the square root of the phase spectrum. The rms phase of each screen is normalized by σ_ϕ.

2.3. The Two-Layer Power-Law Model

The model proposed by Flatté and Wu (1988) for the crust and upper mantle beneath NORSAR is described by two overlapping layers whose heterogeneities are characterized by power-law spectra. A schematic of the model is shown in Figure 2. The spectra of the heterogeneities are band limited. The lower cutoff is determined by the fact that wavenumbers below $2\pi/D$ cannot be sampled by the finite array with aperture D. For NORSAR the array aperture is $D = 110$ km. The subarray beamforming process determines the upper cutoff; for NORSAR it is $2\pi/5.5$ km. The upper layer is described by a flat spectrum down to a depth of 200 km. This represents the fact that the corner wavenumber of this spectrum is greater than the upper cutoff. Since the corner wavenumber is inversely related to the correlation length of the medium, this suggests that there is considerable structure at distance scales ≤ 1 km. The lower layer ranges from a depth of 15 km down to 250 km. It is thought to consist of predominantly smooth large-scale structure, which may be modeled by an exponential autocorrelation function. The corresponding spectrum in N dimensions is given by $a^N/(1 + K^2 a^2)^{(N+1)/2}$, where a is the correlation length. Evidence suggests that the correlation length is larger than the lower cutoff. Thus the band limited spectrum may be approximated by a pure $K^{-(N+1)}$ power-law spectrum. The relative strengths of the spectra are assumed to be equal at $K = 0.31$ km^{-1}, *i.e.* at a length scale of 20 km.

3.4. Results

The two dimensional version of the model is obtained by setting $N = 2$. The phase screen results were simulated using a total of 24 phase screens; 4 were used for the lowest segment, 18 for the overlapping segment, and 2 in the uppermost segment. For the overlapping segment the phase screens were generated as the sum of realizations of the two spectra. This assumes the two layers are statistically independent. The incident wave in all of these calculations was a 1 Hz normally incident plane P wave. To obtain statistical results from the simulations, 100 realizations were

averaged. The TCF's for the vertical component of the simulated vector wave are compared with the simulated and analytic scalar wave results.

Figures 3-5 show the TCF's for this model with $\sigma = 0.1\%, 0.5\%, 1.0\%$. The solid, dashed, and dotted curves represent the simulated vector wave, simulated scalar wave, and analytic results, respectively. For wave speed perturbations $\leq 0.5\%$ the comparison of the three calculations is excellent. For $\sigma = 1.0\%$, however, the simulated results begin to differ noticeably from the analytic results. For $\sigma = 2.0\%, 5.0\%$ (Figure 6 and 7), there is a slight difference between the rate at which the simulated vector and scalar TCF's decorrelate. The difference is on the order of a couple of kilometers. (Note that only the simulated results are shown in Figures 6 and 7, and the axes are scaled differently than in Figures 3-5.)

Figures 6 and 7 also show TCF's of the horizontal component of the scattered vector wave. It is not clear whether the transverse component TCF's for a direct P arrival can be put to significant use; in practice the signal-to-noise ratio may be too small. We have included these results to illustrate that the phase screen method for vector waves may be used to analyze three-component data, perhaps for arrivals other than the incident P, PKP or PKIKP phases. The additional information contained in the transverse components could possibly lead to tighter constraints on the models of the crust and mantle beneath seismic arrays or single three-component stations.

There are clearly measurable differences in the results depending on the scattering strength of the medium. The simulations verified the analytic results for sufficiently weak structures, but showed that the wavefield decorrelated more rapidly than the analytic results indicated for stronger media. This is intuitively as one would expect; the wavefield in a homogeneous medium, would be totally coherent. The fact that the simulated vector wave decorrelated on slightly shorter distances than the simulated scalar wave may be attributed to the additional scattering modes in the vector case. Only as the strength of the perturbations increased above 2% were P/S conversion effects noticeable in the TCF's. Qualitatively, these results would also be observed for the three-dimensional problem. Quantitatively, however, the generalization is not readily apparent. Further array analysis using phase screen simulations of elastic waves in 3-D media should be performed.

3. ACCURACY OF DIRECT VERSUS SCATTERED PHASES

Accurate yield estimates based on seismic techniques depend on the uncertainties in seismic magnitudes. Among other aspects, the observed seismic magnitudes are subject to the variability of the intermediate receiver-source geology, and the number and quality of observing stations. Richards (1988) has noted that teleseismic body

68

waves do not relate reliably to the yield unless the data is processed from many stations. Other phases such as Lg or P-coda often provide excellent estimates of yield for data obtained at only one or two stations, but depend on the crustal structure, propagation distance, etc. In a study by Nuttli (1986a), 22 Nevada Test Site (NTS) nuclear explosions in hard rock were analyzed. The magnitude–yield relation for $m_b(Lg)$, using data from only 2 or 3 stations, versus the announced yield, exhibited a remarkably small variance. Nuttli (1986b) also analyzed Lg data taken at NORSAR for 23 Semipalatinsk explosions. Richards (1988) has noted the Nuttli's Lg data do not exhibit the same degree of consistency as that of published P-coda data (Gupta et al., 1985), observed at a single teleseismic station, for the same events. The consistency of the data were determined by comparing with an $m_b(P)$, estimated from ISC data (Marshall et al., 1984) using hundreds of stations. Richards has suggested that the considerably longer propagation distances (> 2000 km) may be responsible for the inferior results based on $m_b(Lg)$ for the Semipalatinsk events.

These examples illustrate how the number of observing stations, geology and propagation distances influence which portion, or phase, of the seismogram provides the best estimate of yield. Ideally, large sets of physical data could be used to calibrate the seismic stations and determine which magnitudes or weighted combination of magnitudes provide the most reliable yield estimates. Unfortunately, relevant seismic data are not always abundant, particularly at new stations. A practical approach to supplement the information gained from physical data is to numerically simulate seismic data.

As a first step towards understanding the scattering affects responsible, we have simulated elastic wave propagation in uniform isotropic random media. We generated a large statistical ensemble of data (20 realizations of each model by 16 synthetics, at each 25 km interval out to 200 km), and computed the variances of the direct P wave peak-to-peak amplitude and the rms scattered amplitude of the transverse component in the velocity window between the P and S wave speeds. It is the first such study of this type of which we are aware. It is made possible by the tremendous efficiency of the numerical propagation algorithm we use. The CPU time required to run each model was under 3 hrs. on an ELXSI 6400. To run this problem on a CRAY-2 would take under 20 minutes.

The random media are conveniently characterized by their autocorrelation functions, which measure the similarity of nearby points in the medium. In this study, we focused on isotropic exponential ($N(r) = e^{-r/a}$) and 0th order Von Karman (self-similar) ($N(r) = K_0(r/a)$) functions, where r is the spatial offset and a is the correlation length (e.g., Chernov, 1960; Tatarskii, 1961). For all of the media considered here, we assumed mean P and S wave velocities of $\bar{\alpha} = 6.0$ km/s and $\bar{\beta}$

= 3.5 km/s, respectively. We also assumed that the ratio of P to S wave speeds was fixed throughout the medium. Let the rms velocity perturbation be denoted by $\sigma = (\delta\alpha/\alpha)_{rms} = (\delta\beta/\beta)_{rms}$. The random medium models considered in this study are listed in Table 1.

Table 1. List of Models.

Model	Corr. Function	σ	a (km)
1	Exponential	2%	5.0
2	Self-Similar	2%	5.0
3	Exponential	2%	2.5
4	Self-Similar	2%	2.5
5	Exponential	5%	5.0
6	Self-Similar	5%	5.0
7	Exponential	5%	2.5
8	Self-Similar	5%	2.5

Statistically representative realizations of the velocities may be generated by the well established technique of filtering computer-generated Gaussian random numbers, corresponding to each point on a discrete lattice of the medium, with the square root of the desired power spectrum. The power spectrum is the Fourier transform of the autocorrelation function. In two dimensions, the power spectra corresponding to the exponential and self-similar functions are $a^2(1 + k_r^2 a^2)^{-3/2}$ and $a^2(1 + k_r^2 a^2)^{-1}$, respectively. The media were normalized by their standard deviation σ. For this study, the number of gridpoints used to sample the medium was 512 by 2048, and the sampling interval was 0.1 km in each direction.

Once the velocities for a particular medium have been generated, the phase factors needed in the phase screen algorithm were obtained as follows. The medium is divided into intervals, by planes of constant z (referred to as screens in much of the literature), such that the accumulated phase between the screens may be computed from geometrical optics principles. The phase for the P wave, computed by integrating (or for the discrete case, summing) the P wave speed perturbations along the direction of propagation, is given by eq. (16). There is an analogous expression for the S wave phase factor. In practice, 40 phase screens were used in each run.

A Ricker wavelet was used as the initial pulse in our study. The time source function of a Ricker wavelet and its Fourier transform are given by

$$F(t) = (1 - (2\pi f_0(t - t_0))^2/2) \exp\left(-(2\pi f_0(t - t_0))^2/4\right), \qquad (20)$$

$$\tilde{F}(f) = \frac{2}{\sqrt{\pi} f_0} \left(\frac{f}{f_0}\right)^2 \exp\left(-(f/f_0)^2 + 2\pi i t_0 f\right), \qquad (21)$$

where f_0 is the peak frequency and t_0 defines the origin of time. The value $f_0 = 1$ Hz was used for all of the simulations. The maximum frequency sampled was 5 Hz, where the norm of the spectrum has dropped off to $\sim 10^{-10}$. The number of positive frequencies sampled was 256; the remaining frequency data were zero padded to minimize wrap-around effects when numerically Fourier transforming to the time domain.

Sixteen synthetic seismograms were generated at 25 km intervals out to 200 km for twenty realizations of each random medium model considered. The synthetics were evenly spaced in the horizontal direction. Figures 8-15 show characteristic synthetics at 50 km intervals for the eight models. Using a total sample of 320 seismograms at each interval, we computed the first and second statistical moments of the vertical peak-to-peak P wave amplitude $(m_b(P))$, and the rms amplitude of the transverse component, in the time window between $z/\bar{\alpha} + 1/f_0$ to $z/\bar{\beta}$. The time window corresponds more closely to that of P-coda, however, we have denoted this rms amplitude by $m_b(Lg)$ since it is part of the transverse component. (We hope that the serious seismologist will not hold this notation against us. A layered structure, necessary to actually produce Lg, is not present in our models. We have also misused the definition of m_b, which is customarily used to denote the logarithm of an amplitude. These expressions should be thought of only as amplitudes of direct (vertical) and scattered (horizontal) phases.)

In Figures 16-23 we have plotted the standard deviations, given as percentages relative to the means. These plots show that near the source the direct P wave amplitude has far less variation than the scattered phase, which is only beginning to form. However, at some distance away, between 50 km to 150 km from the source for these models, the scattered phase has less variation. In all cases, the cross-over distance was greater for the self-similar media than the exponential media with the same parameters. This result may be attributed primarily to the rate at which the P wave standard deviation changes with distance, and from one model to next. In fact, perhaps the most interesting result of this study is that the standard deviation

of the scattered phase is so insensitive to the model. At 200 km the relative standard deviation of the scattered phase is between 0.11 and 0.12 for six of the eight models. The other two values are 0.13 and 0.14 for models 1 and 5, respectively. In contrast, at 200 km the relative standard deviations of the P wave range from 0.14 for model 4 to 0.41 for model 1.

To interpret these results, scattering theory provides some insight. Wu (1990) has pointed out that large-scale heterogeneities have the greatest affect on the distribution of forward scattered waves. Thus it is not surprising that the media with the greatest power at low wavenumber (or equivalently, on large distance scales) should produce the largest variations in the direct P wave. Models with 5% perturbations lead to greater variations in the P wave than those with 2%. Also, since the self-similar media have more small-scale structure than the exponential, but both are normalized to have the same total power σ, the power at low wavenumber is greater for the exponential medium. Our results indicate that exponential media lead to larger variations in the P wave amplitude than do the corresponding self-similar media, keeping everything else fixed.

Media with larger correlation lengths, for all other parameters fixed, lead to larger variations in the P wave as well. One might argue that this result could be caused in part by the fact that we have averaged over twice as many synthetics per correlation length when $a = 2.5$ km as when $a = 5.0$ km. To explore this possibility, we have compared the results when only half as many samples per correlation length were used for the $a = 2.5$ km cases. These results are represented by the open symbols in Figures 18,19,22,23. The difference in the relative standard deviations are negligible.

Wu (1990) has also noted that the small-scale heterogeneities are responsible for scattering at large angles, and hence the generation of coda. Although the relative standard deviations of the scattered phase do not vary much from one model to the next, they are in general the smallest for the self-similar media. The presence of considerable small-scale heterogeneities produces a more uniform distribution in the scattered waves.

Simulations for more realistic layered earth models are needed before further conclusions may be drawn concerning the variability of body waves, surface waves, regional phases and P-coda. Our study shows that useful information may be gained from such simulations. It will be necessary to use an efficient propagation algorithm, such as the phase screen method used here, in order to generate a sufficiently large synthetic database needed for this type of study.

ACKNOWLEDGEMENTS

REFERENCES

Aki, K., Scattering of P waves under the Montana Lasa, *J. Geophys. Res.*, *78*, 1334–1246, 1973.

Aki, K., and P. G. Richards, *Quantitative Seismology: Theory and Methods*, Vols. 1 and 2, W. H. Freeman, San Francisco, Calif., 1980.

Bertreussen, K. A., A. Christoffersson, E. S. Husebye, and A. Dahle, Wave scattering theory in analysis of P wave anomalies at NORSAR and LASA, *Geophys. J. R. Astr. Soc.*, 42, 402–417, 1975.

Bramley, E. N., The accuracy of computing ionospheric radio-wave scintillation by the thin-phase screen approximation, *J. Atmos. Terr. Phys.*, 39, 367–373, 1977.

Buckley, R., Diffraction by a random phase-changing screen: A numerical experiment, *J. Atmos. Terr. Phys.*, 37, 1431–1446, 1975.

Capon, J., Characterization of crust and upper mantle structure under LASA as a random medium, *Bull. Seismol. Soc. Am.*, *64*, 235–266, 1974.

Chernov, L. A., *Wave Propagation in a Random Medium*, McGraw-Hill, New York, 1960.

Filice, J. P., *Studies of the Microscale Density Fluctuations in the Solar Wind using the Power Law Phase Screen Model*, U. Calif., San Diego, Ph.D. Thesis, 1984.

Fisk, M. D., E. E. Charrette and G. D. McCartor, A comparison of phase screen and finite difference methods for elastic waves in random media, to be published (contained in this report), 1991.

Fisk, M. D., and G. D. McCartor, "The Phase-Screen Method for Elastic Waves and Seismic Discrimination", GL-TR-89-0330, ADA220771, Mission Research Corp., 1989.

Fisk, M. D., and G. D. McCartor, The phase-screen method for vector elastic waves, *J. Geophys. Res.*, 96, 5985–6010, 1991.

Flatté, S. M., R. Dashen, W. H. Munk, K. M. Watson, and F. Zachariasen, *Sound Transmission Through A Fluctuating Ocean*, Cambridge University Press, 1979.

Flatté, S. M , J. M. Martin, and R. S. Wu, Numerical simulation of high-frequency teleseismic waves transmitted through the lithosphere to a large array, Fall, American Geophysical Union Meeting, abstract, 1988.

Flatté, S. M., and R. S. Wu, Small-scale structure in the lithosphere and asthenosphere deduced from arrival-time and amplitude fluctuations at NORSAR, *J. Geophys. Res.*, 93, 6601–6614, 1988.

Frankel, A., and R. W. Clayton, Finite difference simulations of seismic scattering: Implications for the propagation of short-period seismic waves in the crust and models of crustal heterogeneity, *J. Geophys. Res.*, 91, 6465–6489, 1986.

Gupta, I. N., R. R. Blandford, R. A. Wagner, J. A. Burnetti, and T. W. McElfresh, Use of P coda for determination of yield of nuclear explosions, *Geophys. J. R. Astr. Soc.*, 83, 541–553, 1985.

Haddon, R. A. W. and E. S. Husebye, Joint interpretation of P-wave time and amplitude anomalies in terms of lithospheric heterogeneities, *Geophys. J. R. Astr. Soc.*, 55, 19–43, 1978.

Ishimaru, A., *Wave Propagation and Scattering in Random Media*, Vol. II (Academic Press, New York), 1978.

Knepp, D. L., Multiple phase screen calculation of the temporal behavior of stochastic waves, *Proc. IEEE*, 71, 722–737, 1983.

Marshall, P. D., T. C. Bache, and R. C. Lilwall, AWRE Report No. O 16/84 (U.K. Atomic Weapons Research Establishment, December, 1984).

Martin, J. M. and S. M. Flatté, Intensity images and statistics from numerical simulation of wave propagation in 3-D random media, *Applied Optics*, 27, 2111–2125, 1988.

Mercier, R. P., Diffraction by a screen causing large random phase fluctuations, *Proc. Cambridge Phil. Soc.*, 58, 382–400, 1962.

Munk, W. H., and F. Zachariasen, Sound propagation through a fluctuating ocean-theory and observation, *J. Acous. Soc. Am.*, 59, 818–838, 1976.

Nuttli, O. W., Yield estimates of Nevada Test Site explosions obtained from seismic Lg waves, *J. Geophys. Res.*, 91, 2137–2151, 1986(a).

Nuttli, O. W., Lg magnitudes of selected east Kazakhstan underground explosions, *Bull. Seismol. Soc. Am.*, 76, 1241–1251, 1986(b).

Ratcliffe, J. A., Reports on Progress in Physics, XIX, 190–263, 1956.

Richards, P. G., *Seismic Methods for Verifying Test Ban Treaties*, in "Nuclear Arms Technologies in the 1990's", Chapter 4, pp. 54–108 (American Institute of Physics, New York), 1988.

Tatarski, V. I., *Wave Propagation in a Turbulent Medium*, McGraw-Hill, New York, 1961.

Tatarski, V. I., *The Effects of the Turbulent Atmosphere on Wave Propagation*, National Technical Information Service, TT-68-50464, 1971.

Wu, R. S. and S. M. Flatté, Transmission fluctuations across an array and heterogeneities in the crust and upper mantle, *Pure Appl. Geophys.*, *132*, 175–196, 1990.

Wu, R. S., Seismic wave scattering, in *Encyclopedia of Geophysics*, D. E. James, ed. Van Nostrand Reinhold, 1988.
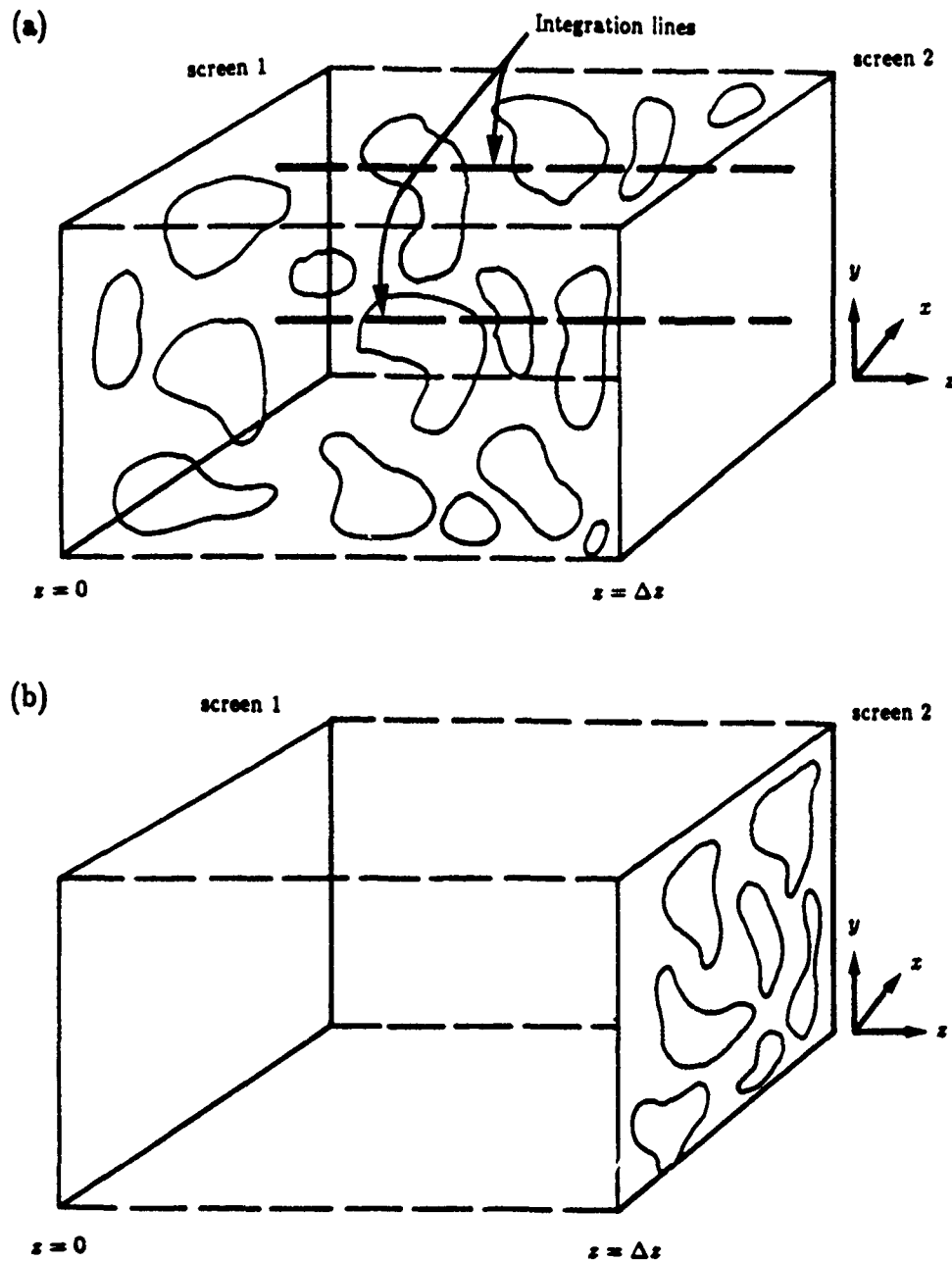
Figure 1. The multiple phase-screen method replaces (a) each segment of the heterogeneous medium with (b) a uniform segment and a phase screen. The accumulated position-dependent phase is projected onto screen 2.
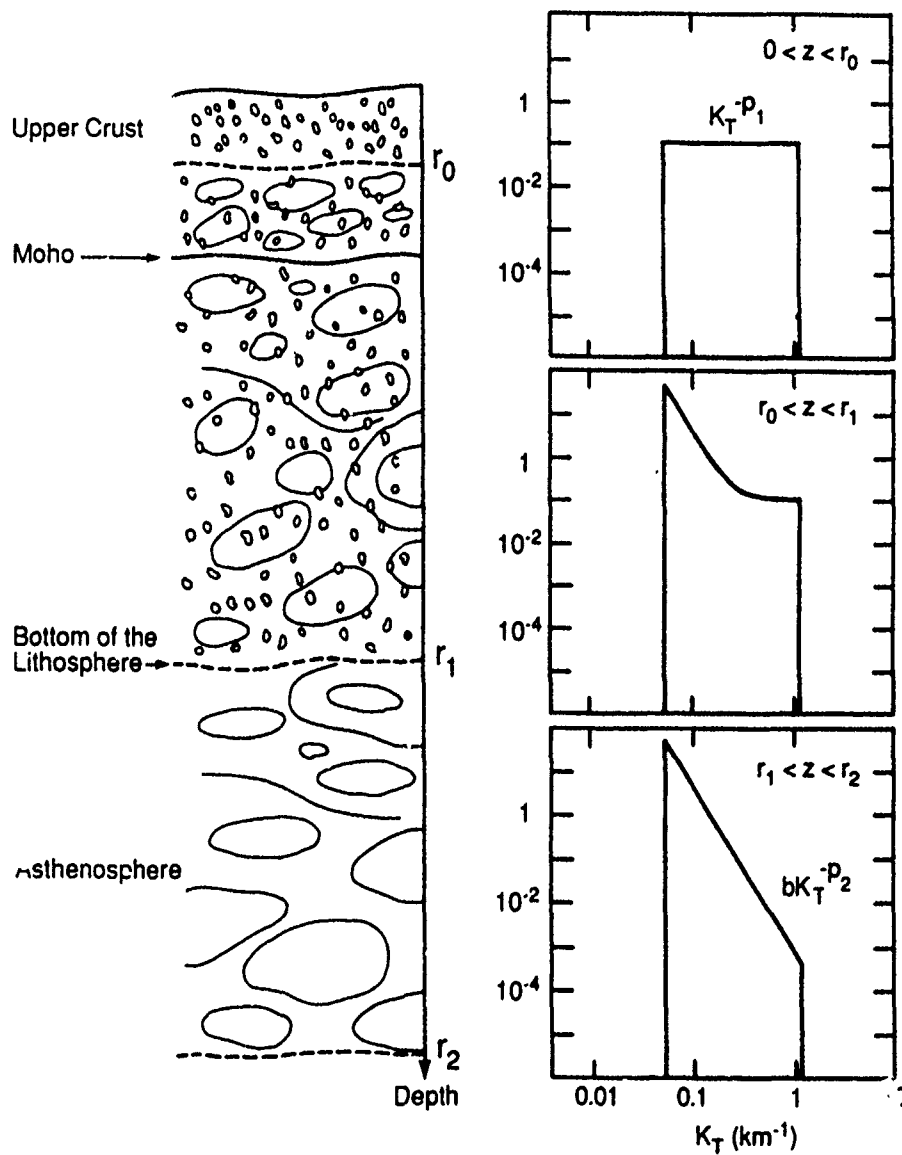
Figure 2. Schematic diagram of Flatté and Wu's two-layer power-law medium for modeling the heterogeneities beneath NOR-SAR. The power spectra for the different layers are shown on the right (from Flatté and Wu, 1988).
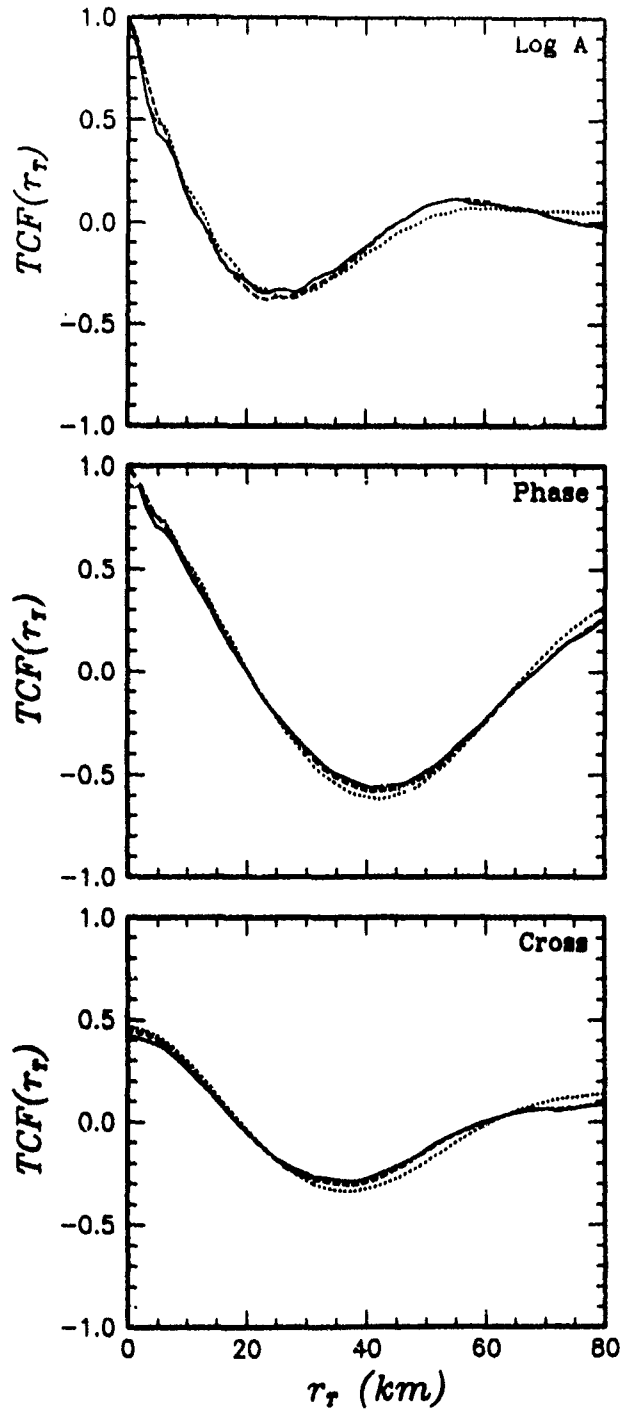
Figure 3. Transverse coherence functions of the log amplitude, phase and cross correlation computed for a P wave transmitted through the two-layer power-law model for an rms velocity perturbation of 0.1%. The solid, dashed, and dotted curves represent the simulated vector wave, simulated scalar wave, and analytic scalar wave results.
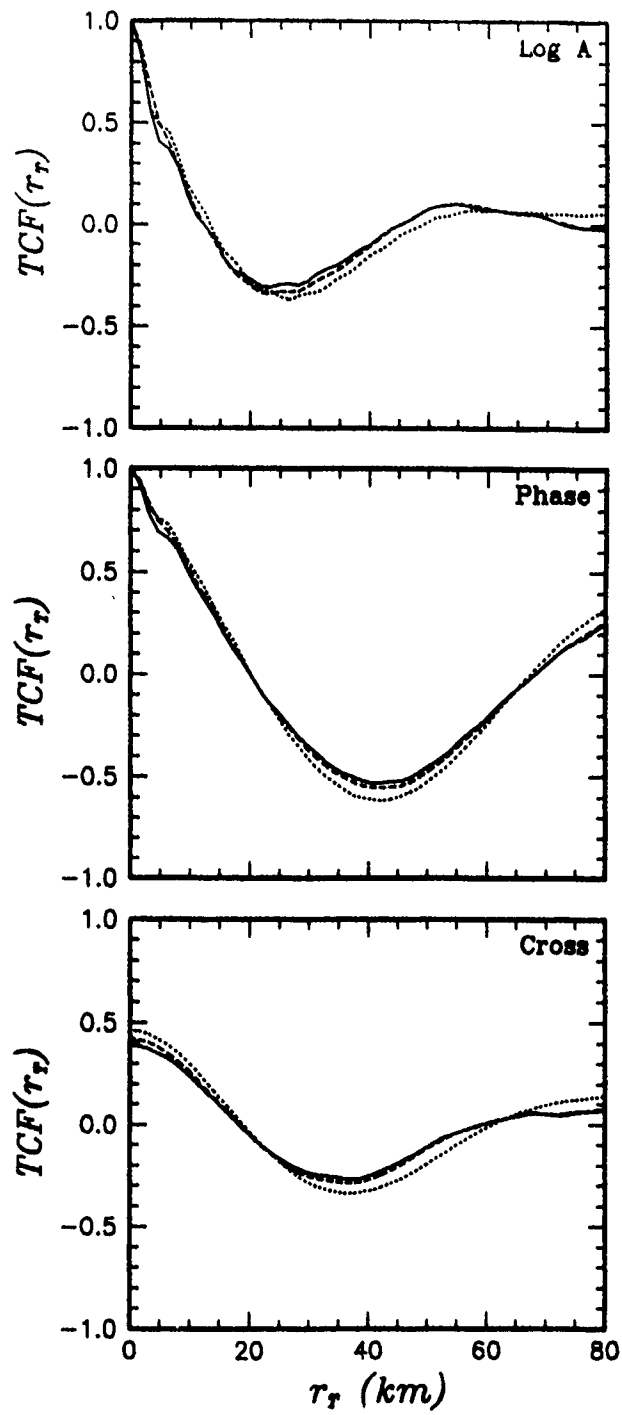
Figure 4. Same as Figure 3, but for an rms velocity perturbation of 0.5%.

79
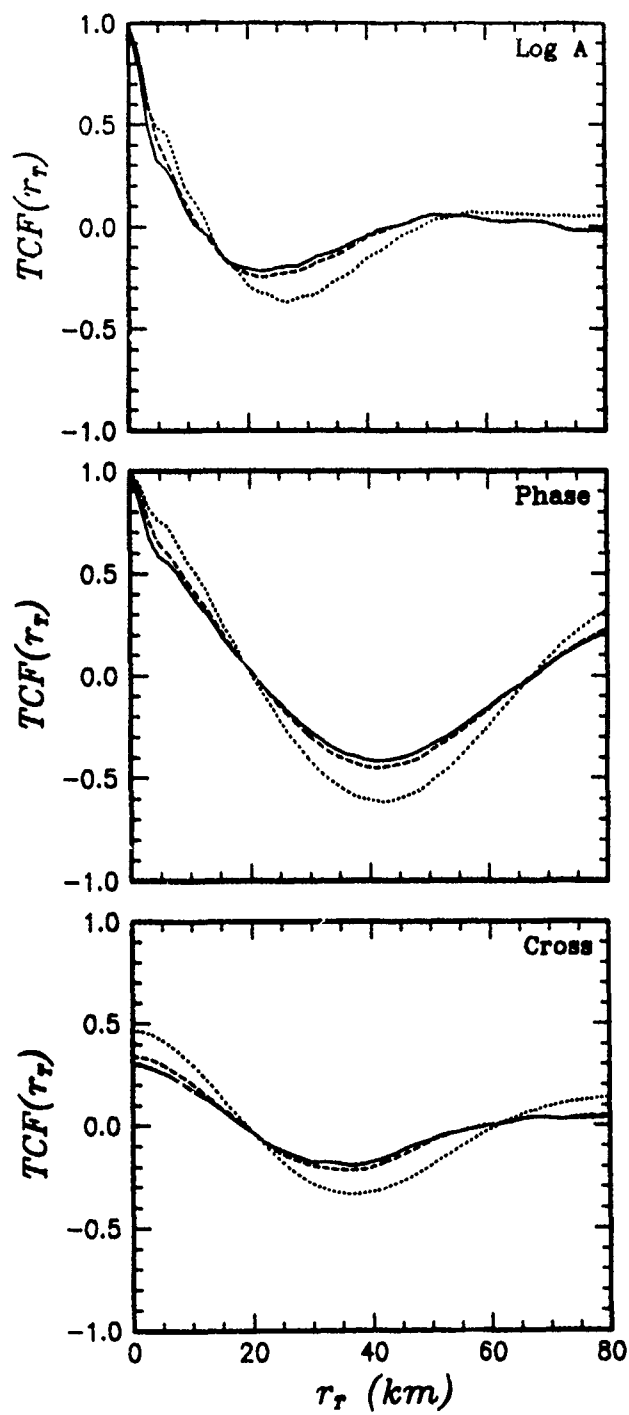
Figure 5. Same as Figure 3, but for an rms velocity perturbation of 1.0%.
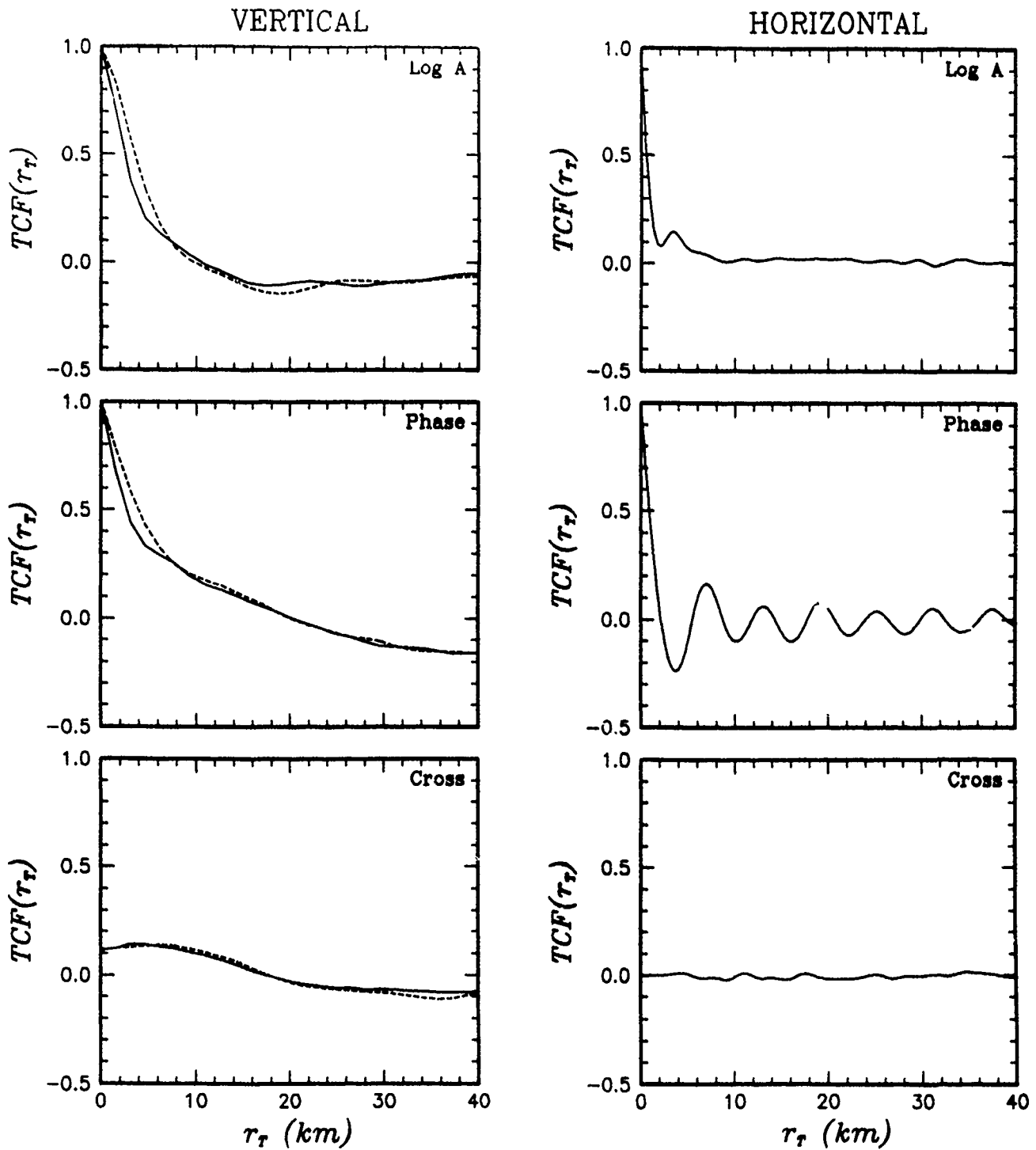
Figure 6. TCF's for the vertical component of the simulated vector wave (solid curve) and the simulated scalar wave (dashed curve) are on the left. On the right are TCF's computed for the transverse component of the simulated vector wave. The rms velocity perturbation was 2.0%.
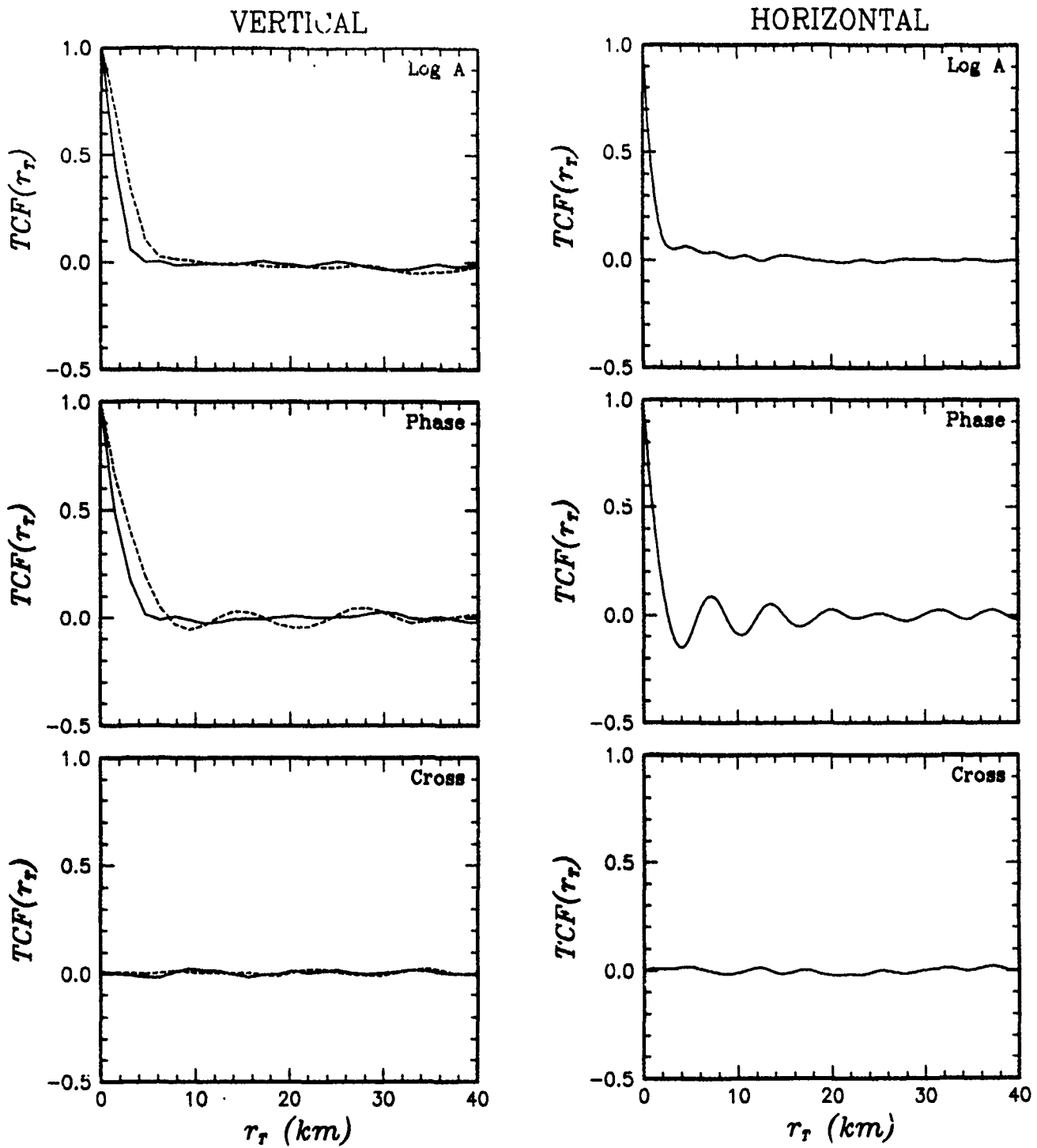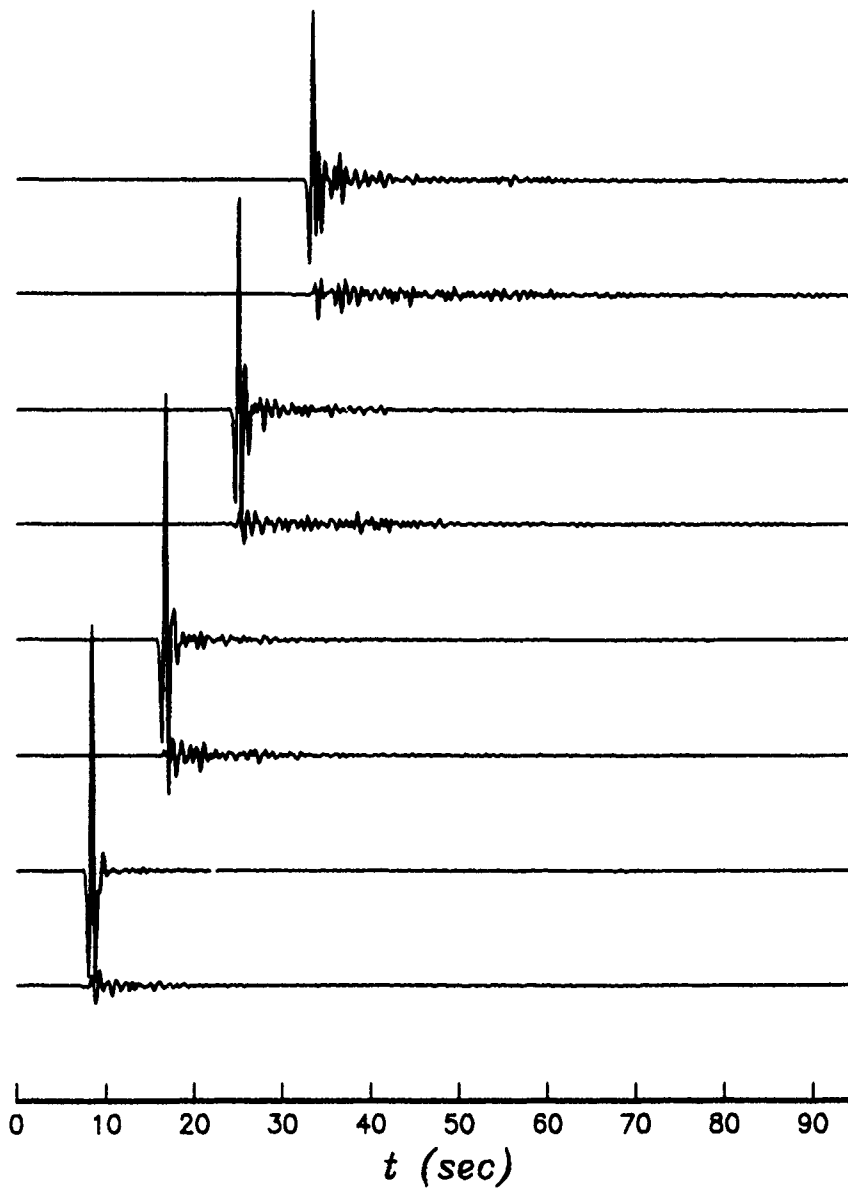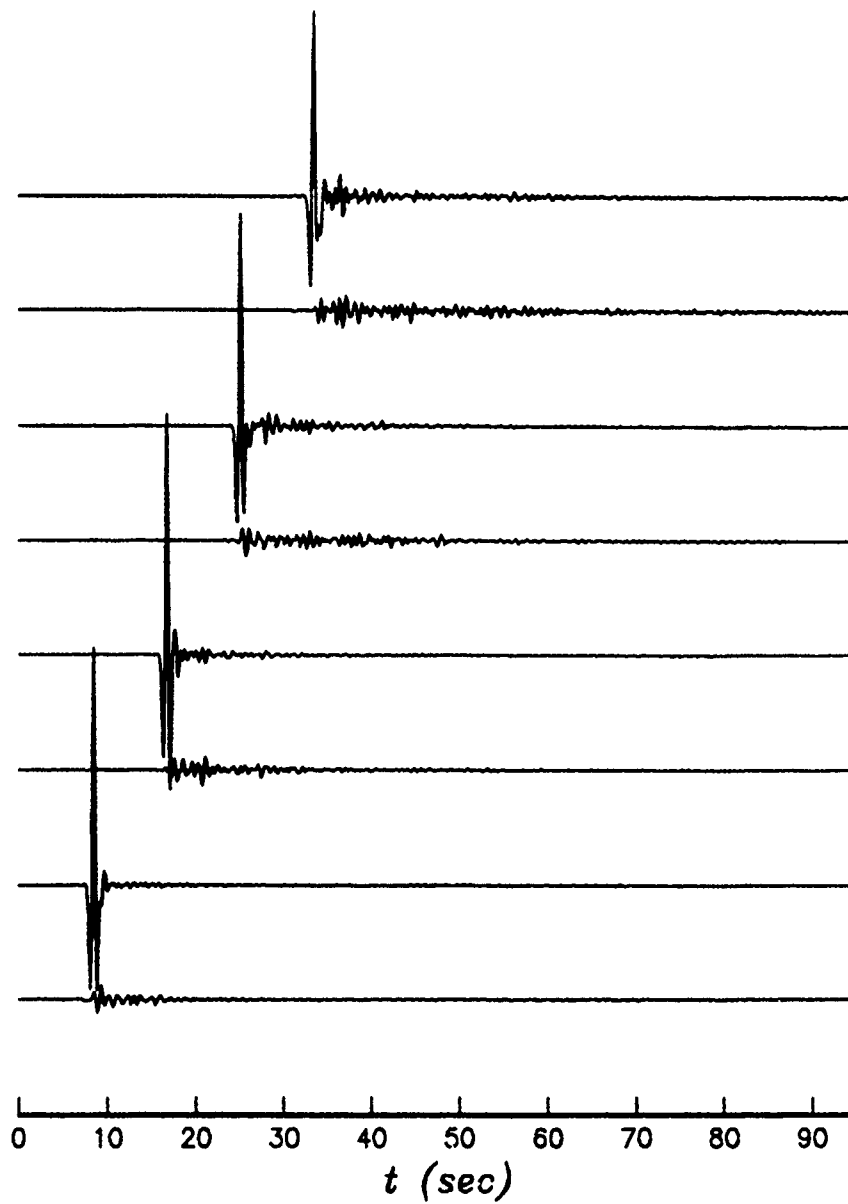
81

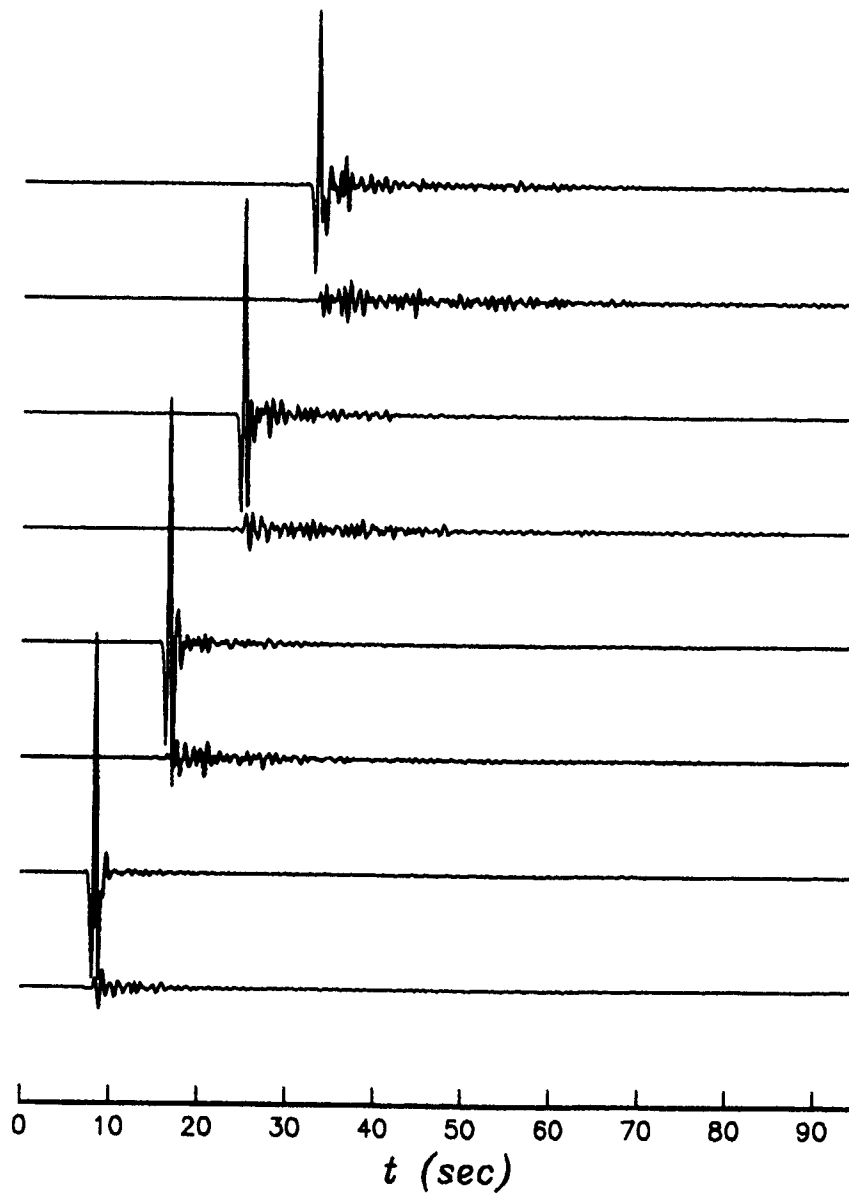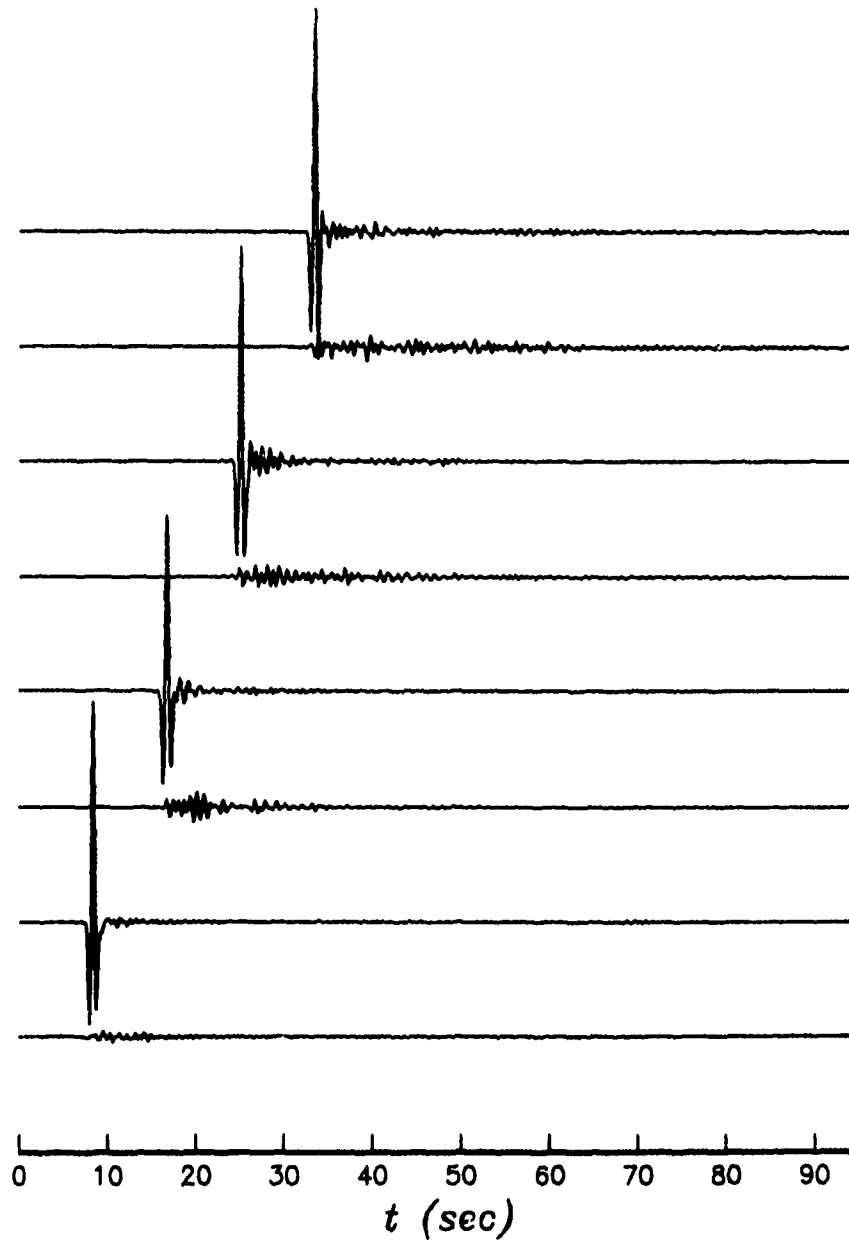**Figure 7.** Same as Figure 6, but for an rms velocity perturbation of 5.0%.

Figure 8. Synthetic seismograms for model 1 at 50 km intervals out to 200 km. The vertical (upper trace) and horizontal (lower trace) components are plotted in pairs.

83

Figure 9. Synthetic seismograms for model 2 at 50 km intervals out to 200 km. The vertical (upper trace) and horizontal (lower trace) components are plotted in pairs.

84

Figure 10. Synthetic seismograms for model 3 at 50 km intervals out to 200 km. The vertical (upper trace) and horizontal (lower trace) components are plotted in pairs.
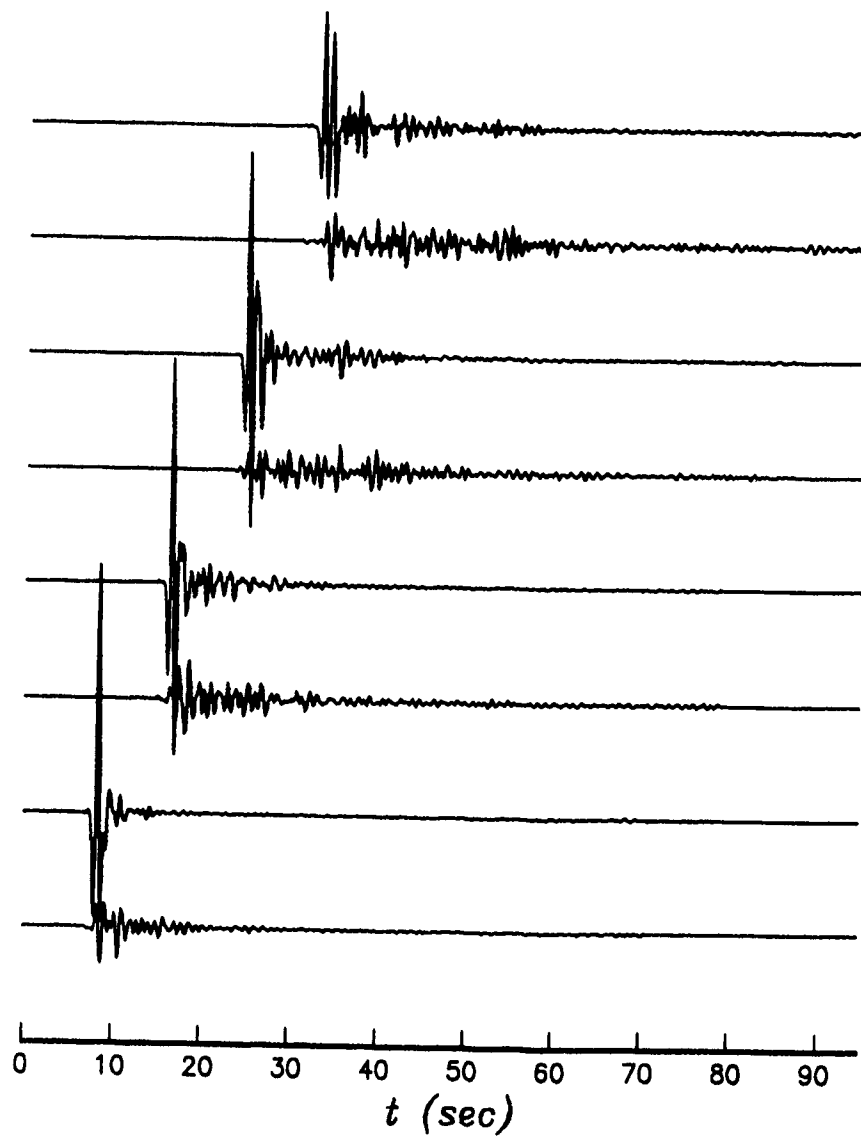
Figure 11.   Synthetic seismograms for model 4 at 50 km intervals out
to 200 km. The vertical (upper trace) and horizontal (lower
trace) components are plotted in pairs.

Figure 12. Synthetic seismograms for model 5 at 50 km intervals out to 200 km. The vertical (upper trace) and horizontal (lower trace) components are plotted in pairs.
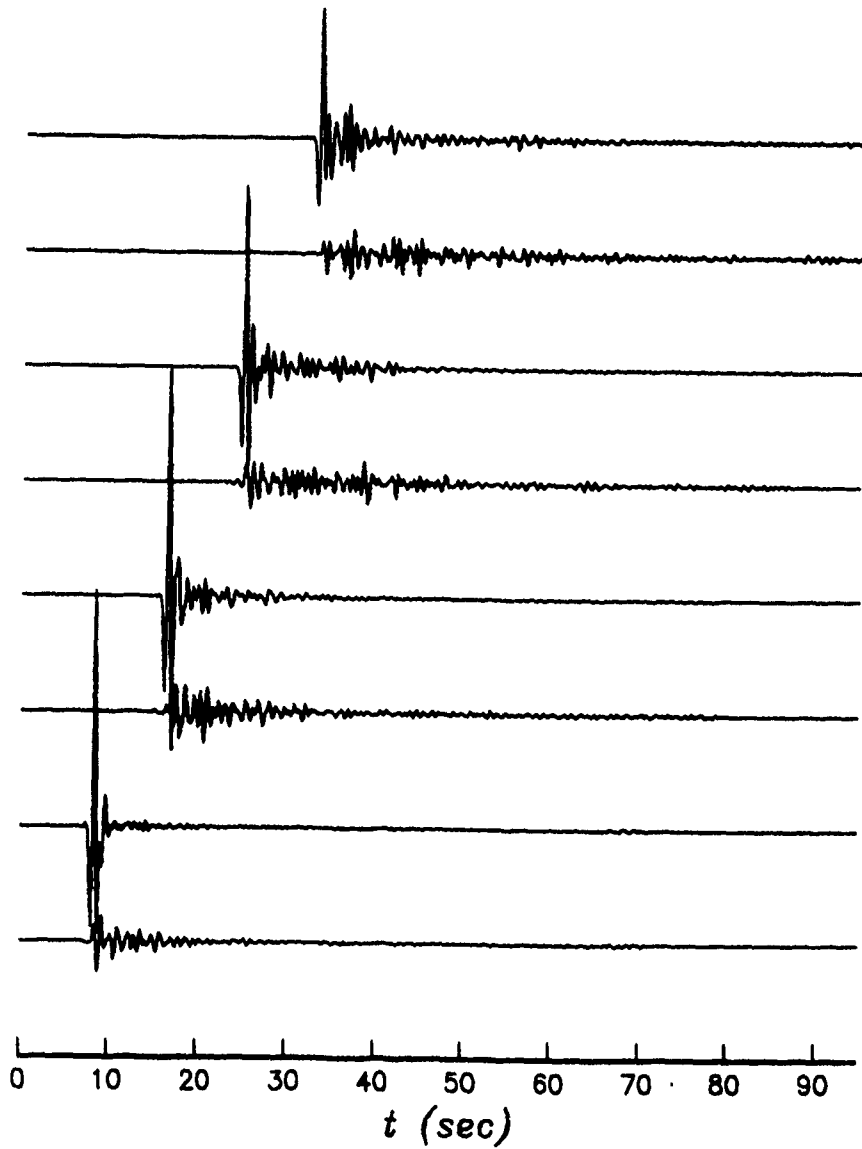
87

Figure 13. Synthetic seismograms for model 6 at 50 km intervals out to 200 km. The vertical (upper trace) and horizontal (lower trace) components are plotted in pairs.

88

Figure 14. Synthetic seismograms for model 7 at 50 km intervals out to 200 km. The vertical (upper trace) and horizontal (lower trace) components are plotted in pairs.
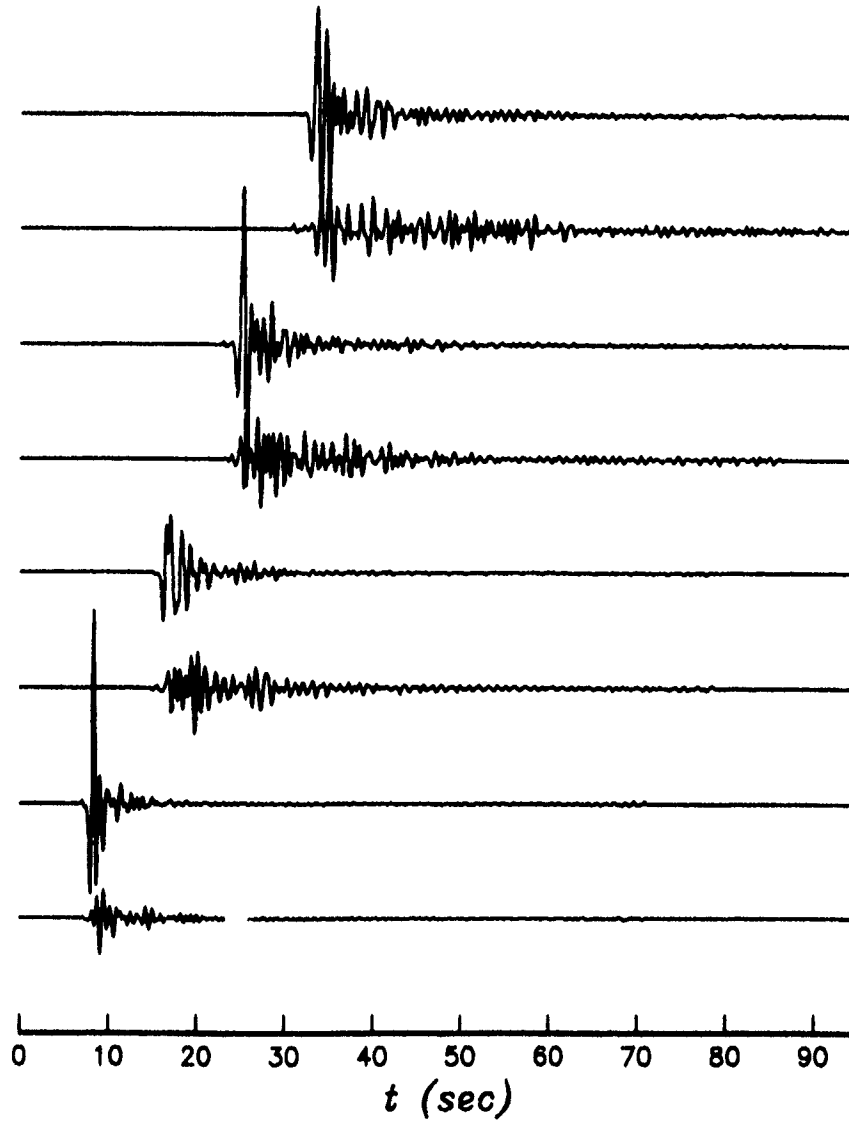
89

Figure 15. Synthetic seismograms for model 8 at 50 km intervals out to 200 km. The vertical (upper trace) and horizontal (lower trace) components are plotted in pairs.
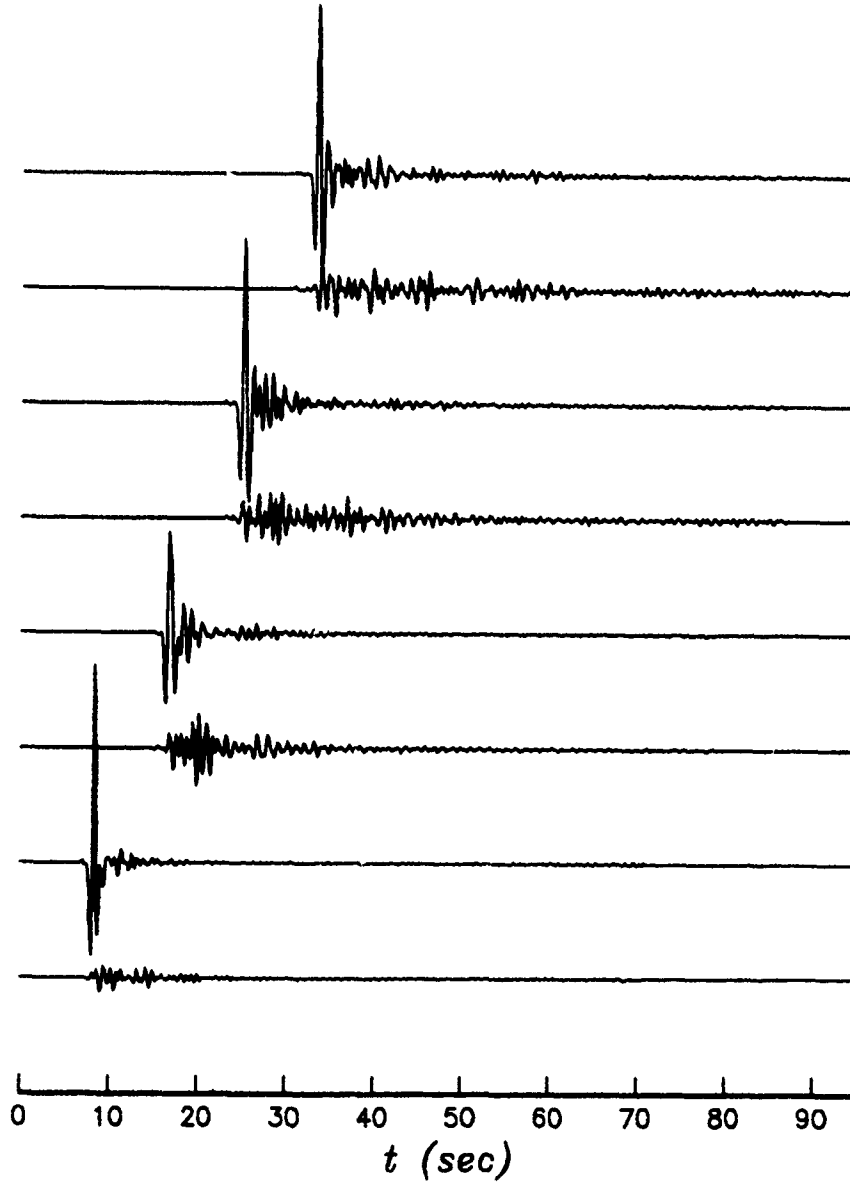
90

Figure 16.   Model 1 standard deviations, given as percentages relative to the means, of the direct peak-to-peak P wave amplitudes $\sigma_{mb(P)}$, and the rms transverse amplitudes $\sigma_{mb(Lg)}$.

91

Figure 17. Model 2 standard deviations, given as percentages relative to the means, of the direct peak-to-peak P wave amplitudes $\sigma_{mb(P)}$, and the rms transverse amplitudes $\sigma_{mb(Lg)}$.

Figure 18. Model 3 standard deviations, given as percentages relative to the means, of the direct peak-to-peak P wave amplitudes $\sigma_{mb(P)}$, and the rms transverse amplitudes $\sigma_{mb(Lg)}$. The open symbols represent the results, averaged over half as many samples per correlation length.
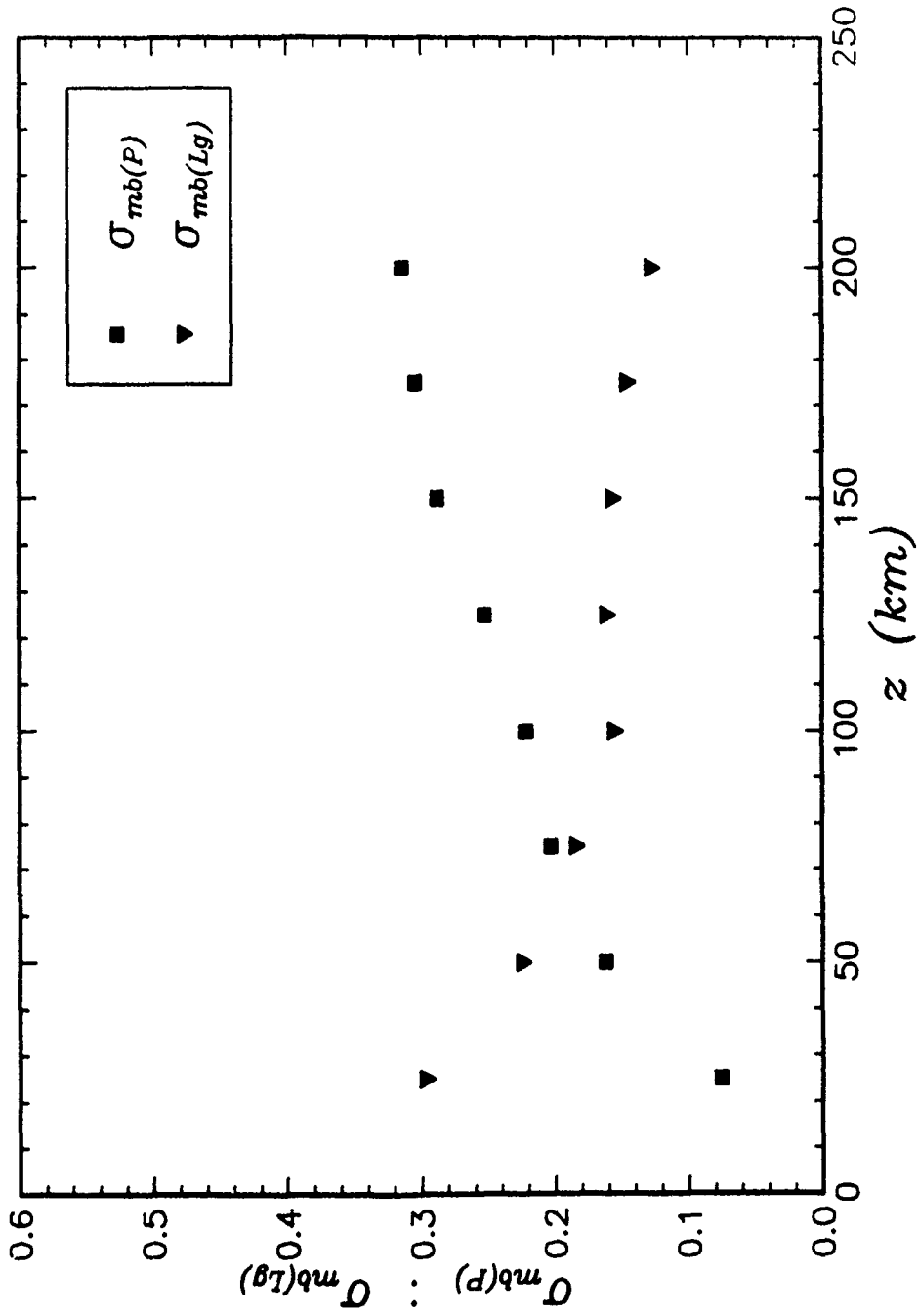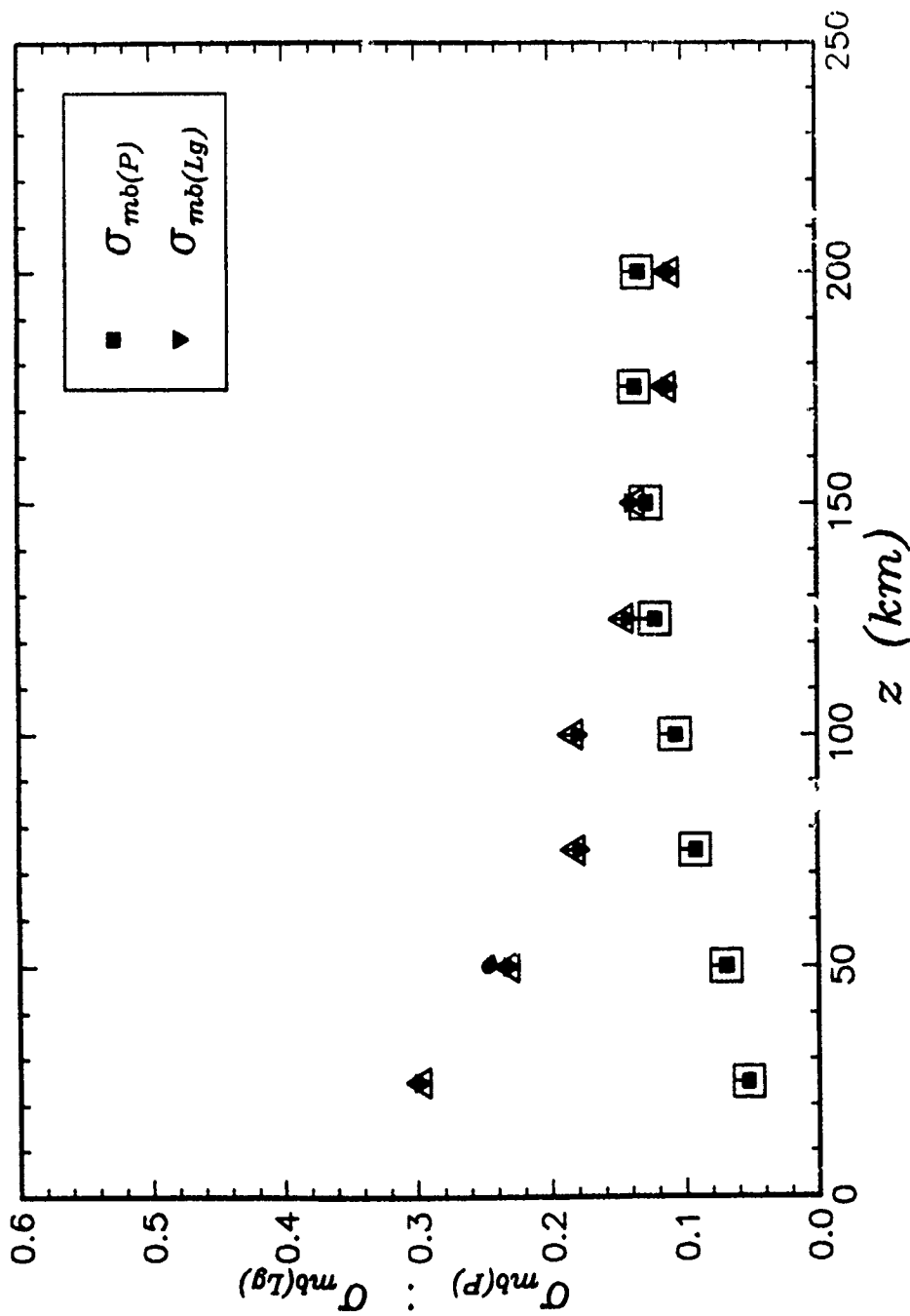
Figure 19. Model 4 standard deviations, given as percentages relative to the means, of the direct peak-to-peak P wave amplitudes $\sigma_{mb(P)}$, and the rms transverse amplitudes $\sigma_{mb(Lg)}$. The open symbols represent the results, averaged over half as many samples per correlation length.

94
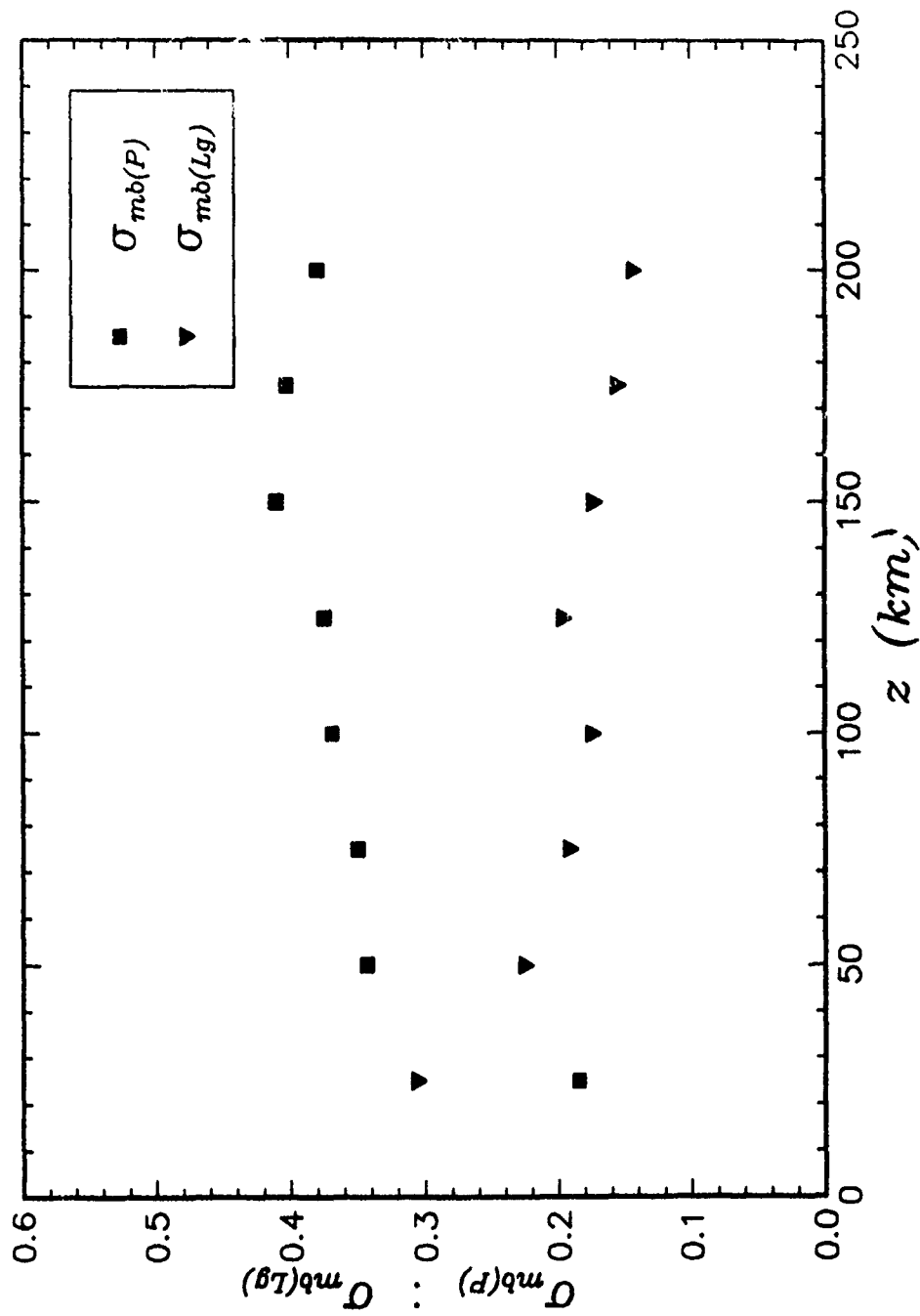
Figure 20. Model 5 standard deviations, given as percentages relative to the means, of the direct peak-to-peak P wave amplitudes $\sigma_{mb(P)}$, and the rms transverse amplitudes $\sigma_{mb(Lg)}$.
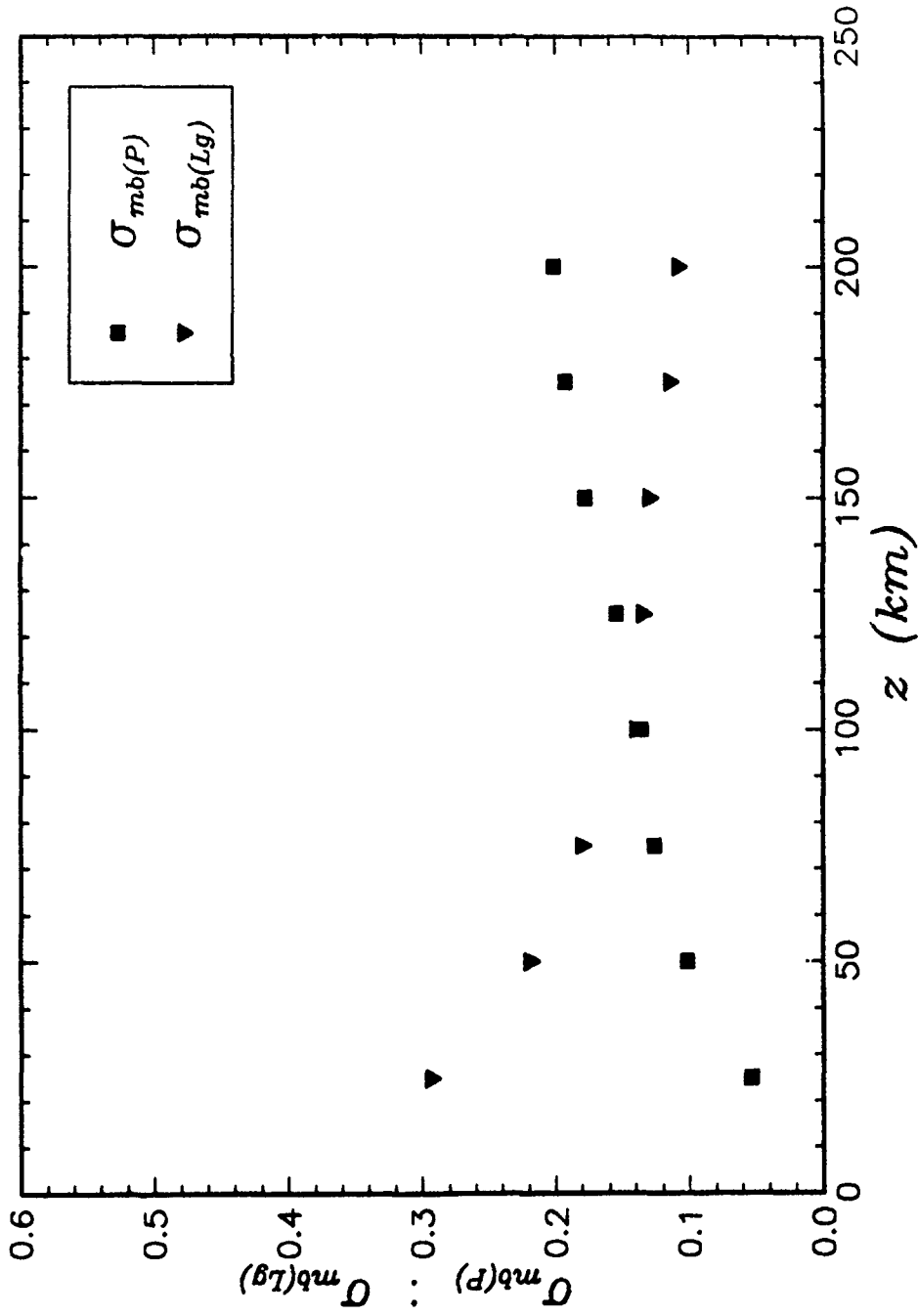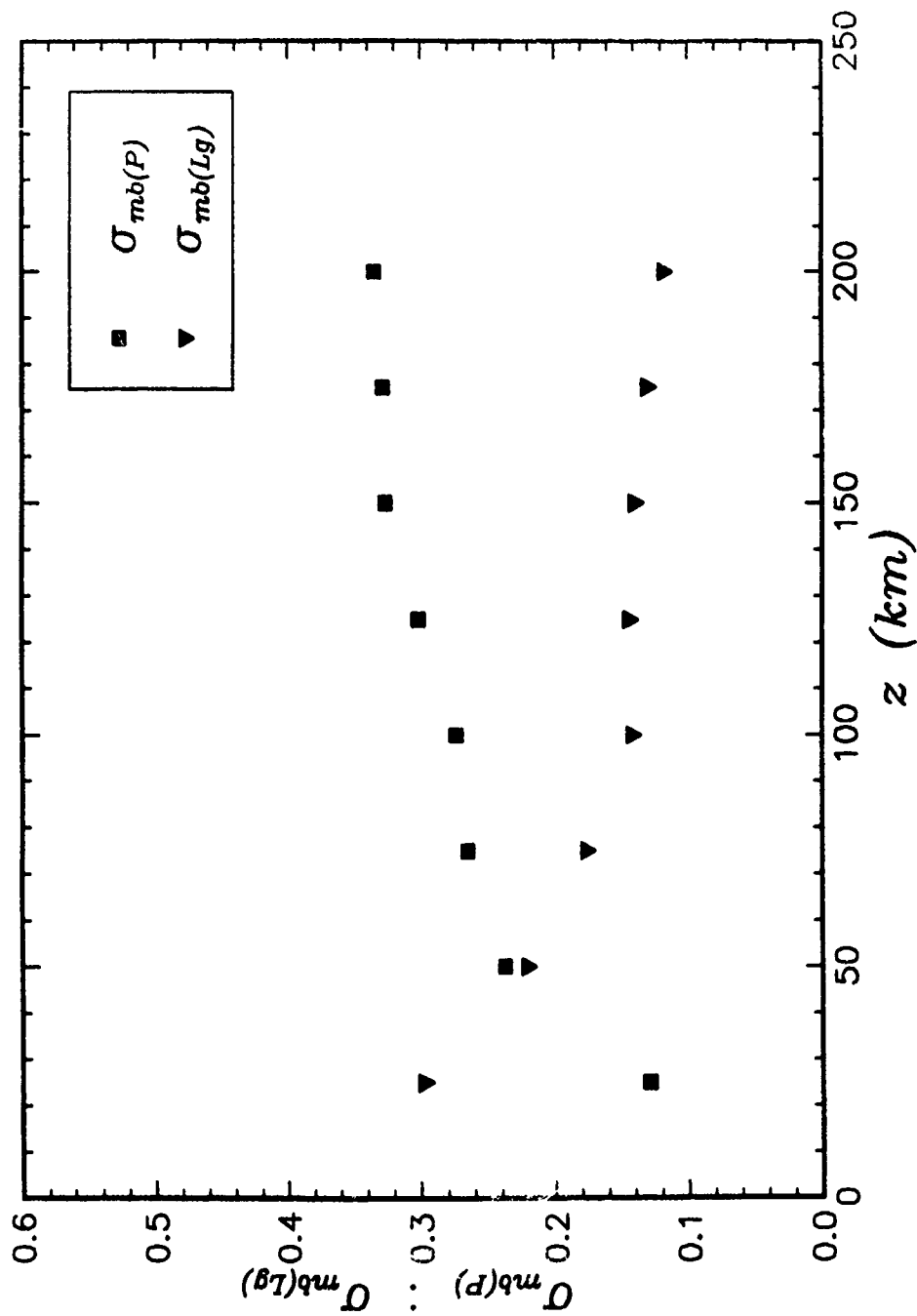
Figure 21. Model 6 standard deviations, given as percentages relative to the means, of the direct peak-to-peak P wave amplitudes $\sigma_{mb(P)}$, and the rms transverse amplitudes $\sigma_{mb(Lg)}$.
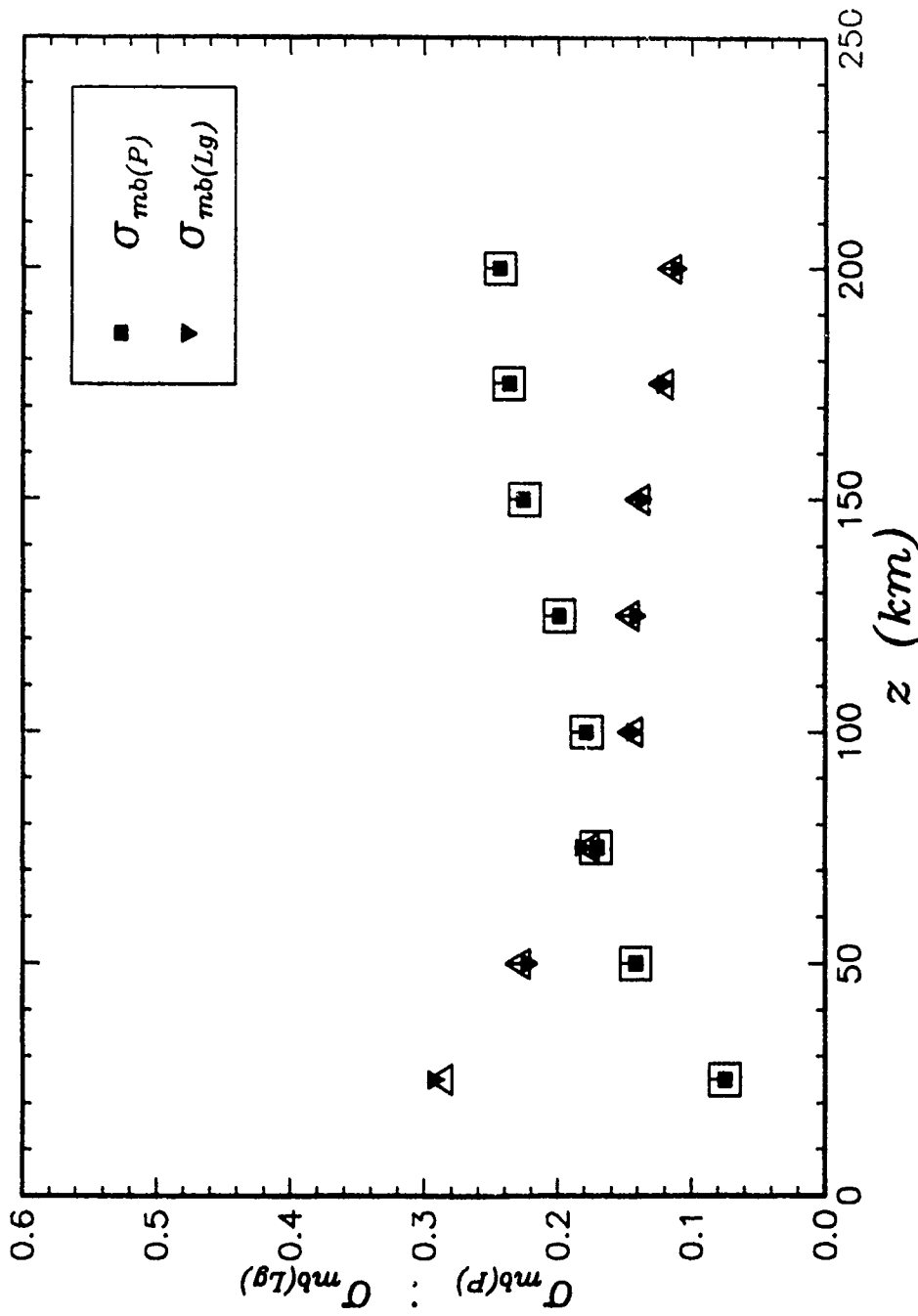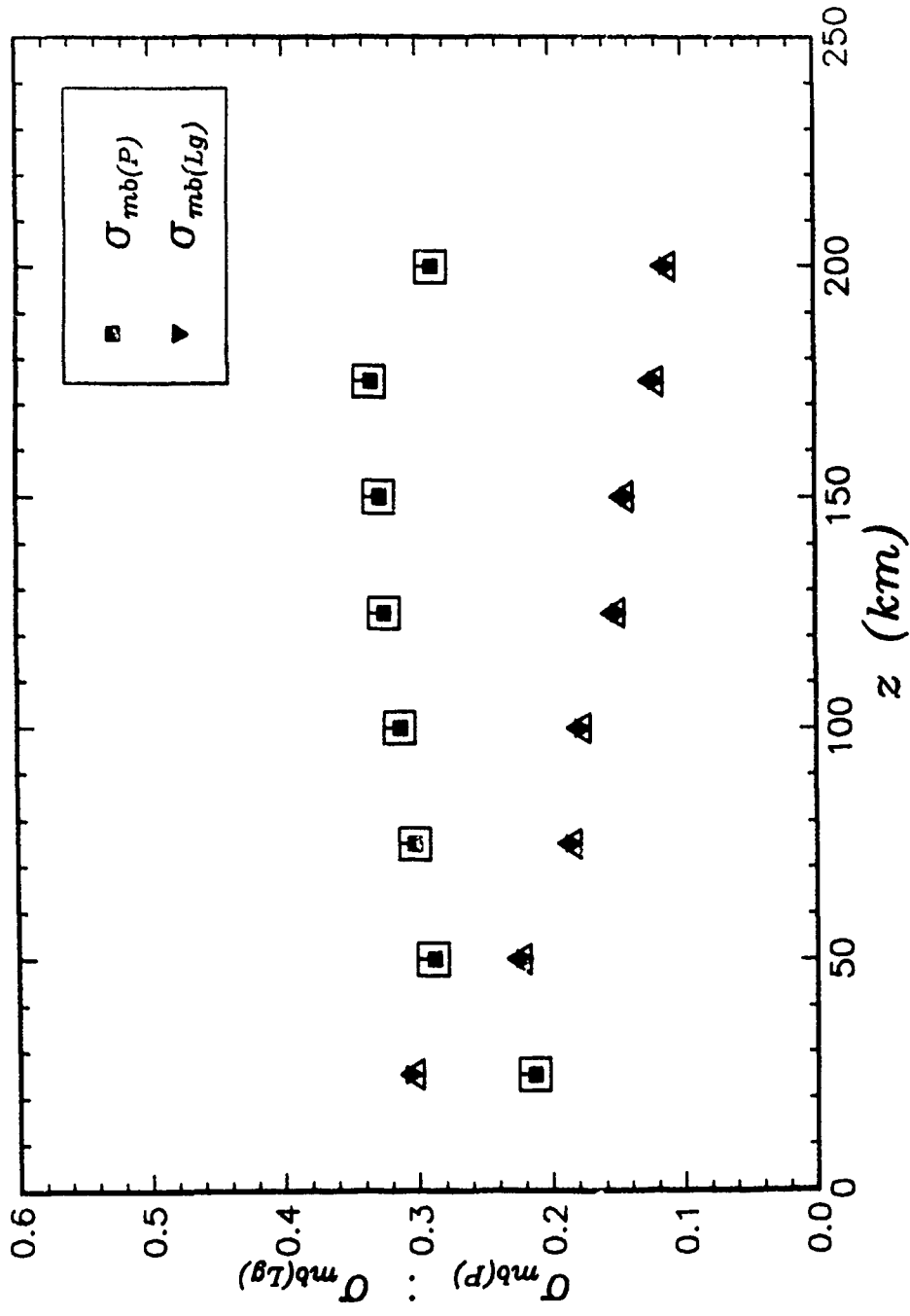
Figure 22. Model 7 standard deviations, given as percentages relative to the means, of the direct peak-to-peak P wave amplitudes $\sigma_{mb(P)}$, and the rms transverse amplitudes $\sigma_{mb(Lg)}$. The open symbols represent the results, averaged over half as many samples per correlation length.

Figure 23. Model 8 standard deviations, given as percentages relative to the means, of the direct peak-to-peak P wave amplitudes $\sigma_{mb(P)}$, and the rms transverse amplitudes $\sigma_{mb(Lg)}$. The open symbols represent the results, averaged over half as many samples per correlation length.
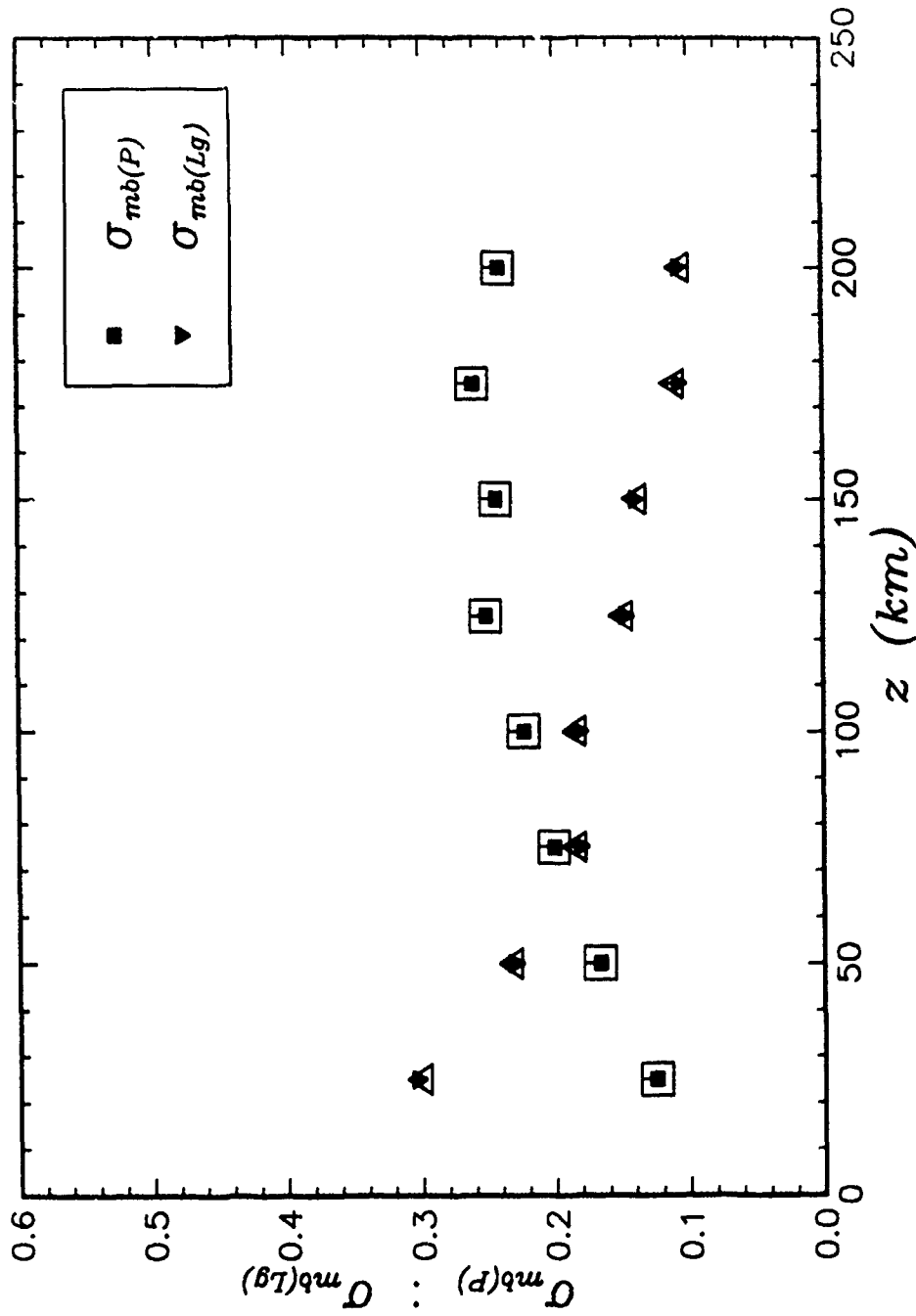
REVIEW OF ATTENUATION IN SALT AT MODERATE STRAINS

W. R. Wortman and G. D. McCartor [1]

Abstract. Experiments which reflect the attenuation of propagating pulses in salt in the moderate strain regime of 10^{-3} to 10^{-6}, which corresponds roughly to ranges of 100 to 10,000 meters from an explosion with a yield of 1-kt, are reviewed. A transition from nonlinear to linear behavior occurs in this interval. This regime is important for monitoring of nuclear test treaties since models for linear source functions are normally defined inside it. Salt is of interest since it can be readily mined to produce decoupling cavities. Data from explosive sources, nuclear and chemical field and small scale laboratory tests, resonant bars and ultrasonic pulse methods are summarized. The experiments are diverse in their character and frequency and no single experiment covers the nonlinear-linear transition. However, the totality suggests that attenuation in salt does decrease dramatically over the moderate strain regime. A full physical description does not exist although shear failure or yielding can account for some effects.

Introduction

Seismic monitoring of underground nuclear tests requires that properties of distant seismic signals be related to the yield of the explosive source. In general, providing this relation requires finding the material response to explosive loading under an extreme range of conditions. The rock next to the explosive device is vaporized out to about 10 meters for a 1-kt explosion. Somewhat beyond this the rock is melted and crushed. Out to a range of many tens of meters the rock is visibly cracked. All these effects are highly nonlinear. Fortunately, it is not necessary to provide first principles calculations of this behavior in order to monitor nuclear tests. Subsurface ground data have been taken which can be used to define the pulse from explosions in a variety of media outside the highly nonlinear regime. These data, along with some supporting theoretical calculations for interpolation, can be used to define an equivalent seismic source at the range where the data were taken. This bypasses many uncertainties from complex material behavior under extremes of temperature and pressure. It is common to assume that the resulting source, which is typically defined at a few hundred meters, can be propagated further to seismic receivers assuming that the medium is strictly linear, although not elastic with attenuation described by a linear Q operator, while taking into account the intervening geologic structure. With this, the computed waveform properties can be compared with those observed to estimate yield and depth. This technique is the fundamental approach to monitoring nuclear test treaties.

---

[1] Now at Department of Physics, Southern Methodist University, Dallas, TX 75275

As we shall see in this article, there is strong evidence of nonlinear attenuation in the range of moderate strains (sometimes called high-strains), which we define here as strains from 10^{-3} to 10^{-6} which occurs at roughly 100 to 10,000 m from a 1-kt explosion, which extends well outside the usual region, or "elastic radius," where equivalent seismic sources are defined. The effect of this nonlinear attenuation, for which the attenuation depends on the amplitude of the disturbance and not just the material properties, between ranges showing highly nonlinear structural changes and ranges with linear strains levels (roughly 10^{-6}) is not well understood. There is a substantial body of data on attenuation in salt which can be brought to bear on this question. Salt is also particularly interesting because it is relatively easily mined to produce cavities which could serve to decouple clandestine tests [Evernden et al., 1986]. For both of these reasons, salt is a medium for which the seismic response is important. In this article we shall indicate the nature and results of experiments which have been done in salt. There are three types of experiments which have provided useful attenuation data in salt. These are: explosive source generated pulse propagation, either in the field or the laboratory; ultrasonic pulse propagation; and resonant bar excitation.

The explosive source technique is obviously most directly related to the question at hand. It consists of placing a set of motion sensors at various ranges and orientations relative to a source to cover the amplitudes of interest. As a practical matter, there are limits on the number of sensors which can be used due to the available volume of uniform medium. The result is a set of time domain pulses measured at a discrete set of sensors which can be ordered according to range from the source to the sensor. When the effects of orientation, instrument response and spherical divergence are removed, the change of the pulse with range reflects the results of any attenuation. For linear attenuation described by a Q operator, the multiplicative change in amplitude in the frequency domain with a range change, δr, goes like

$$\exp(-\omega \delta r / 2cQ) \qquad (1)$$

where c is the phase speed. For linear mechanisms, Q^{-1} can be interpreted as the fractional energy loss per cycle over 4π or the tangent of the phase angle between the stress and strain. Through the above relation, generally referred to as using the spectral ratio method, Q is a common measure of attenuation even if the mechanism is not known to be linear. Using this measure, a Q as a function of frequency can be estimated for every pair of records.

Ultrasonic pulse propagation using a planar geometry can also be used to estimate a Q from (1). A sample, usually with a linear dimension of a few centimeters but large compared with the pulse wavelength, is placed between a pair of plates. One plate is pulsed with a finite source waveform while a transducer at the receiver plate detects the transmitted pulse. The timing of the received pulse allows determination of propagation speed while the spectral ratio of the transmitted and received pulses fixes Q. Both compressional and shear pulses can be measured by this method. The requirement of a reasonable apparatus and sample size limits this technique to ultrasonic frequencies.

The resonant or oscillating bar method does not involve pulse propagation. It measures the response of a damped resonant system to a harmonic driver, for which the damping element is the material under study. Typically a cylindrical rod approximately 10 cm in length is loaded with appropriate weights to give a resonant frequency as low as practical, often a few hundred Hertz. The system is then driven in torsion or flexure modes and its resonant response determined as the driver frequency is scanned across the spectrum. The resulting response given as an amplitude as a function of frequency determines the damping of the system. The half power bandwidth of the resonance curve divided by the resonant frequency is Q^{-1}.

It must be pointed out that the concept of Q is confined to linear attenuation. If there are nonlinear effects, Q may well not be a robust description which allows a meaningful comparison of different experimental results or a useful means of applying the results of experiments. The danger of blind use of experimental Q will be illustrated in this article.

Experimental Attenuation Data Available For Salt

Explosive Sources- Nuclear

Salmon. The nuclear explosion Salmon (5.3-kt) event took place in a natural salt dome in Mississippi in 1964 at a depth of 828 meters. A comprehensive set of approximately 83 near-field measurements at 16 instrument stations was planned, both at surface and subsurface locations at ground ranges from 166 to 744 meters [Perret, 1967]. A parallel set of measurements was carried out by SRI [Eisler and Hoffman, 1966]. A rather consistent set of near-field subsurface measurements including scaled ranges from 95 to 425 m/kt$^{1/3}$ resulted. The single component acceleration and velocity instruments provided measurements of a range of peak strains from about 4×10^{-3} to 2×10^{-4} with dominant frequencies from 1 to over 10 Hz. A representative set of particle velocity records [McCartor and Wortman, 1985] is shown in Figure 1.

The Salmon data have been discussed by several authors. The original experimenter, Perret [1967], gives an extensive description of the experimental details. He indicates that the peak acceleration, velocity and displacement data all tend to fall off in a fairly uniform manner with range. The peak radial velocity falls off like range to the -1.876 ± 0.049 power as shown in Figure 2. This decay rate, which is well in excess of the -1 power for geometrical far-field elastic fall off, is an indication that there is some attenuation mechanism in operation but it is not necessarily an indication of nonlinearity.

Rogers [1966] described the Salmon free-field data and compared the results with finite difference calculations. These comparisons generally show agreement with the magnitude of the pulses but the waveforms are noticeably different. This indicates that the models of highly nonlinear material behavior based on prior experiments in salt were within reason, but these mechanisms generally cease to be important at the ranges of the Salmon data. This article was a part of a Journal of Geophysical Research issue [Volume 71, No. 14, 1966] with a sequence of articles on the Salmon event.

McCartor and Wortman [1985] analyzed a selected sequence of the Salmon free-field records for the purpose of finding clear evidence of nonlinearity with this data set alone. It was found that these data require an effective Q which increases significantly with increasing frequency and which has a value of about 5 in the dominant frequency range from 5 to 10 Hz. This is consistent with Trulio [quoted by Larson, 1982] indicating that the Salmon data for decay of peak velocity with range are consistent with an effective Q of about 3 in the 0.5 to 5 Hz range for strains near 10^{-4}. Figure 3 shows a typical effective Q found using the spectral ratio of free-field records from 166 and 660 meters from the shot point. Examination of a series of Q estimates from 5 record pairs over this same range, shown in Figure 4, does not show clear evidence of decreasing attenuation with range. The extreme range record pairs attenuation estimates appear to differ by about 20%, decreasing with range, but this is the same level as the uncertainties. The Salmon elastic precursor which leads the Salmon pulses has been accounted for by McCartor and Wortman [1990] by a partial shear failure which permanently reduces the shear modulus when the strain exceeds a threshold of about 10^{-4}. Rimer and Cherry [1982] have shown that it is possible to reproduce much of the Salmon data, including the precursor, using a shear strength limit which is variable.

Gupta and McLaughlin [1989] analyzed Salmon and Sterling data and concluded that the effective Q at Salmon strains appears to be mildly strain dependent and strongly frequency dependent. The mean apparent Q in the 1-25 Hz range is about 7 and it appears to increase mildly with increasing range. The result for attenuation is reflected in a modified Q function called $\bar{Q}$. This is defined as $\bar{Q} = Q + f \, dQ/df$ which is a measure of the spectral slope change. The behavior found is shown in Figure 5. Gupta and McLaughlin argue that the decrease in attenuation with range is significant and this indicates that the behavior is nonlinear. The attenuation decreases sharply with increasing frequency. Denny [1990] reports that the source spectra characteristics of Salmon and Sterling indicate that the Salmon pulses are nonlinear to beyond 700 m.

Sterling. The nuclear explosion Sterling (0.38-kt) event took place in 1966 in the Salmon cavity, which was approximately spherical with a radius of 17 meters. This was the second half of the decoupling test and the same instrumentation was used. The waveforms observed are generally noisy and less cohesive than for Salmon. Sterling data [Sisemore et al., 1969] are at lower strains than Salmon due both to lower yield and decoupling. Sterling peak velocities indicate a strain range of 3×10^{-5} to 7×10^{-6}. Some analysis of these data by Springer et al. [1968] suggested that there was significant near-field attenuation. A more recent analysis by Glenn et al. [1987] corrects some errors in the previous work and indicates that the observed Sterling near-field pulses are in good agreement with elastic theory. Gupta and McLaughlin [1989] used a spectral ratio method to determine the attenuation over sensor pairs. They find that the average Q is approximately 200 to 400 and shows no evident dependence on frequency or range. These last two papers suggest that the Sterling strains have reached a transition to a linear low attenuation at small strains, near 10^{-5}. Langston [1983] has noted that SV waves generated by Sterling, apparently due to induced normal faulting rather than cavity asymmetry, showed attenuation with range which was significantly different from 1/r. He finds that Q_β of 35 is indicated at strains of about 10^{-5} and there is a mild tendency for Q_β to increase with range, and

so with decreasing strain. If it is assumed that there is no contribution to attenuation from compression, the corresponding P-wave Q will be approximately 70, although there is no direct evidence to tie the two modes together for this particular case.

Gnome. The Gnome explosion (3 kt) took place in the Salado salt layer at a depth of 360 meters [Weart, 1962]. Above the salt there were strata to a depth of about 200 meters consisting of diverse lithology. Analysis of the data from eight sensors sites located horizontally from the shot point at ranges of 62 to 477 meters indicates that there are three distinct arrival times. The high speed initial signal appears to be from refraction in a polyhalite layer below the shot, the normal moderate speed signal then appears followed by a plastic wave with a speed which diminishes with decreasing strain. Some of the acceleration records are clipped so it is difficult to use the details of the waveform to characterize the attenuation. Weart indicates that the peak velocity falls off like range to the -3.56 power out to 100 meters and then like the power -1.36 out to the last sensor at 477 meters. It is suggested that the elastic zone has been reached at this extreme range but no evidence beyond the amplitude variation with range is given.

Explosive Sources-Chemical

Cowboy. The Cowboy series of chemical explosions took place in a salt dome in Louisiana in 1959-60 [Murphey, 1961]. The explosions had a range of yields from 10 to 2000 pounds of TNT, some of which were carried out in cavities for decoupling tests. Each shot was sampled by from two to seven particle velocity sensors. The scaled ranges for the coupled or tamped experiments were from about 200 to 3000 $m/kt^{1/3}$ and the corresponding peak strains were from a few times 10^{-4} to about 10^{-5}. The dominant frequencies were 10 to 100 Hertz. Murphey observed that the peak velocity with scaled range (range/yield$^{1/3}$) data all lie near a smooth curve and they fall off like $r^{-1.65}$, as shown in Figure 6. This indicates first that the data scale and second that the material behavior is not elastic.

Minster and Day [1986] examined the Cowboy tamped data and investigated the attenuation required to reproduce the observed variation of peak velocity and displacement with scaled range. They conclude that an effective Q which is strain dependent with the frequency independent form

$$1/Q = 1/Q_0 + \gamma\varepsilon \tag{2}$$

can satisfactorily reproduce the both peak velocity and displacement. Here $Q_0 = 100$ is the small strain Q, ε is the peak strain and $\gamma \approx 3 \times 10^3$ is an empirical constant. This form was chosen to be consistent with some theoretical nonlinear mechanisms at high strains while reducing to modest anelastic attenuation at small strains. The resulting attenuation is consistent with scaling since it depends only on strain which scales. Note that the effective Q at the largest strains from Cowboy is then less than 10.

Trulio [private communication] has examined some scaled Cowboy data and concluded that the attenuation is frequency dependent, decreasing with increasing frequency. Q values of 12.5 and 32 are found at Salmon equivalent frequencies of $10^{1/2}$ and 10 Hz, found by scaling the

Cowboy data. The frequency dependence is roughly $Q \propto 1/f$. He observes that this dependence is inconsistent with linearity and scaling indicating that Cowboy attenuation is nonlinear.

Wortman and McCartor [1989] have used tamped Cowboy records to attempt to determine the character of the attenuation. They chose record pairs from the same shot and applied the spectral ratio method to determine the effective Q between the stations. By selecting pairs with internal consistency and by correcting the records for obvious anomalies, they found a set of Q estimates as a function of peak strain or range. The result is shown in Figure 7 as compared with the result of Minster and Day [1986]. Not surprisingly, the results are similar and they show that across the strains available in the Cowboy data there is a substantial decrease in attenuation with decreasing strain.

Cowboy Trails. Cowboy Trails [Workman and Trulio, 1985] was a series of field tests in a salt dome using chemical explosives of approximately 200 pounds. The single and dual explosions were monitored with free-field ground velocity sensors. The ranges of the sensors, which were varied over the ten events, covered from 0.388 to over 11.3 $km/kt^{1/3}$. They were set to attempt to define the transition to clearly linear behavior. Due to problems with sensors and noise, the Cowboy Trails experiments did not fully accomplish their goals. However, the results indicate that the propagation of explosively driven pulses in dome salt remain inelastic (though not necessarily nonlinear) out to scaled ranges of 11.3 $km/kt^{1/3}$. The exponent of peak velocity power law decay with range is -1.46±.05 which is somewhat slower than that seen in the Cowboy data (which were for higher strains). An analysis by Trulio [private communication] suggests that the scaled Cowboy Trails data show a decreased attenuation with range and frequency which is not inconsistent with scaled Salmon and Cowboy results. The scatter of the data is fairly large so it is difficult to draw stronger conclusions.

Livermore 1982 Small Scale Experiments. The experiments of Larson [1982] for small chemical explosions, yields of 0.63 to 291 kJ, in pressed salt have provided pulses over scaled ranges from approximately 10 to 250 $m/kt^{1/3}$. The dominant range of frequencies covered was from about 10^4 to 10^5 Hz and the ratio of peak particle velocities to compressional sound speed (which is comparable with the strain) went from about 10^{-1} to less than 10^{-3}. Data from three sensors at increasing ranges for a single shot, taken in pairs, indicate increasing values of Q from 12 to 25 with increasing range for ranges from 30 to 70 $m/kt^{1/3}$. This would suggest that the response was nonlinear. Another experiment consisting of a simultaneous pairs of shots, was used as a direct superposition experiment. It was found that the resulting response was consistent with that determined by linear addition of the two pulses at a range of 168 $m/kt^{1/3}$ as would be expected from a linear medium. Still it is not clear just how nonlinear effects would be manifest in this experiment of rather narrow pulses without knowing the character of any nonlinear behavior. That is, the apparent agreement with superposition for pulses with large strains may very well not directly negate the possibility of any sort of nonlinear behavior. Still, on the basis of this experiment, Larson concludes that the propagation is linear beyond 168 $m/kt^{1/3}$. He also indicates that the attenuation is strongly inelastic inside this range and that the magnitude of this inelasticity decreases with both range and frequency. By variation of the confining pressure, he finds that the propagation is independent of confinement at least up to

32 MPa. Larson combined his data with that from other salt experiments to further extend Trulio's [1978] assertion that peak velocity data for explosively driven pulses in salt scales remarkably well. This is shown in Figure 8 which contains data from experiments with over 10 orders of magnitude in yield. Larson also provides a direct comparison of scaled waveforms for his experiment and a Salmon pulse which shows a significant similarity.

Livermore 1987 Small Scale Experiment. In 1987 Larson [1989] carried out an additional laboratory experiment using a 0.622 kJ chemical explosion in mined dome salt. The cylindrical sample was sliced into layers perpendicular to the axis. Sixteen sensors were then inserted at eight ranges and the layers were cemented together. A explosive source tamped in a hole on one side then produced peak particle velocities from 1 m/s to 4×10^{-3} m/s. The experiment was not very successful. A variety of problems with the samples caused irregularities in the waveforms which made analysis difficult. Wortman and McCartor [1989, Appendix C] have reproduced the waveforms and attempted to find the attenuation. Aside from an apparent increase of Q with frequency, little can be concluded.

Nonexplosive Sources

Ultrasonic Pulse Attenuation. New England Research (NER) laboratory ultrasonic pulse propagation experiments [Coyner, 1987] used strains from less than 10^{-6} to more than 10^{-5}. Compressional and shear ultrasonic pulses consisting of about two cycles at 100-200 kHz were propagated through samples. Attenuations were calculated using a spectral ratio technique with an aluminum sample used for calibration. Variation of the attenuation with peak strain amplitude and confining pressure were determined. For dome salt it was found that over a strain range of 5×10^{-7} to 3×10^{-5} and for confining loads of either 0.1 or 1 MPa, the P-wave attenuation is nearly constant and can be described by a Q of about 20. For S waves, the Q_β is also nearly constant and it has a value of about 60. The results are shown in Figure 9. With the possible exception of the largest strains for S waves, there is no particular evidence of nonlinearity in these data alone although the attenuation is large. The P-wave attenuation is about a factor of three larger that that of S waves suggesting that the conventional assumption of dominant losses from shear mechanisms is not the case. It should be noted that these confining pressures are small compared with those for underground sources.

Multicycle Laboratory Experiments

Resonant Bars. Tittmann [1983] has taken laboratory data on the absorption of the energy in multiple cycle oscillations of halite rods. Both dome salt and pressed salt samples were used. These resonant bar experiments measure the width of the resonance peak for cyclic motion at frequencies from about 90 to 500 Hz induced in mechanically loaded salt samples. They were carried out for both torsion and flexure modes with peak strains from 10^{-5} to 10^{-8}. Pressure variation studies were carried out using jacketed samples in pressurized chambers allowing pressures up to 124 MPa. The effects of humidity variation were also determined.

105

The results for pressed salt indicate that attenuation is dependent on all parameters which were varied. Attenuation decreases with increasing frequency and increases with increasing humidity. At ambient pressure, for strains below 2×10^{-6} the attenuation is only weakly nonlinear while above this it is strongly amplitude dependent. In the low strain region Q's for extension and torsion are about 500 and 1000, respectively.

For dome salt the results are somewhat different. Nonlinear behavior persists to very low strains (10^{-8}). For any significant confining pressures the threshold strain for nonlinear behavior increases to about 2×10^{-6} but the attenuation is then essentially independent of pressure up to at least 68 MPa. The attenuation increases slightly with increasing frequency; 1/Q increases by a factor of about two from 80 to 480 Hz. The high pressure behavior appears to stabilize at the quoted levels only after a period of adjustment of hours suggesting that crack healing strengthens the samples under pressure. An illustration of the strain dependence is shown in Figure 10.

Tittmann points out that the attenuation in these multicycle experiments after the hundreds of cycles required, especially for high strains, may reflect changes or damage in the material resulting from previous cycles. Measurements made then may then not correspond to behavior for a single pulse. Tittmann gives no data on this subject but it has been investigated experimentally by Bonner et al. [1989] although not with salt. The difference in attenuation between uncycled granite and samples with 10^7 cycles, attributed to fatigue damage, is shown in Figure 11. This suggests the possibility that Tittmann's experimental strain dependence may actually be the result of damage from cycling. In any case, Tittmann's attenuation for salt is significantly less than that suggested by the other experiments described in this article.

Summary Of Salt Attenuation

While there is a substantial body of data for attenuation of signals in salt, the results are rather diverse. It appears that attenuation is a function of many factors including strain, frequency, humidity, number of cycles, source of salt samples and character of experiment. It is difficult, if not impossible, to combine the various experimental results into a cohesive pattern, let alone a constitutive relation. However, there is some degree of consistency which we shall now attempt to define.

It is most striking that the data from explosive sources roughly satisfy simple cube root scaling for peak velocities, if not for all details of the waveforms. This means that if the lengths and times are all scaled by the cube root of the yield then, to a remarkable degree, all tamped explosive source experiments give approximately the same pulses at any scaled range.

It is perhaps not so remarkable that this scaling should hold near the explosions since the initial pulse character is not determined by attenuation. Rather the scale of the explosively generated cavity is fixed by the cube root of ratio of the density to the yield. Given the propagation velocity, this spatial scale will determine a temporal scale, both varying as the cube root of the yield.

106

The more interesting result is that the pulses continue to scale as they propagate out into the medium at strain levels, less than 10^{-3}, for which there are no gross changes in the medium. If the attenuation suffered is intrinsic to the medium, or linear, the associated Q must be independent of frequency in order for the results to obey cube root scaling. This is clear from the form shown in (1) for the attenuation operator. If scaling holds, the expression $\omega r/cQ$ must scale. The combination ωr has units of velocity which scales while c is constant. Therefore Q must scale but it can only a function of frequency since the medium is assumed uniform and linear and the only function of frequency which scales is a constant. In general, for either linear or nonlinear effects, the fact that the experimental results cube root scale indicates that the medium must have no inherent scales of length or time (in the range of scales of the experiments) so any constitutive relation must be rate independent.

Salmon, Cowboy and small scale laboratory velocity pulses all scale well but they also all indicate that the effective Q extracted is strongly frequency dependent. To illustrate this clearly, consider Figure 12 which shows unscaled estimates of Q as a function of frequency for pairs of records from Salmon and Cowboy at approximately the same peak strain. Note that the two functions of frequency are quite distinct but they are quite similar when scaled relative to their respective corner frequencies. The corner frequency, of course, scales with the cube root of the yield which says that the scaled effective Q's are nearly the same. This has been observed both by Trulio [private communication] and by Wortman and McCartor [1989]. This clearly says that the attenuation is not just a function of the medium but it must depend on amplitude or shape of the pulse. In other words, the attenuation must be nonlinear, at strains above 10^{-4}. Since the behavior is nonlinear, there is no benefit in using a Q description. In fact, the use of Q often serves to confuse the fundamental problem of finding a physically meaningful constitutive relation at moderate strains.

In spite of the fact that moderate strain attenuation is almost certainly nonlinear, it is possible to use effective Q estimates to combine data by taking the effective Q at the dominant frequency. This effective Q gives a measure of the magnitude of attenuation. It is much more difficult to combine attenuation information from explosive pulses and multicycle experiments since the effective Q will generally be a function of the details of the experiment. If a proper constitutive relation were known, a comparison could be made. However, no such relation is known. Ignoring this substantial problem, the data from all the experiments discussed in the text of this paper can be expressed as effective Q and compared as a function of peak strain. Figure 13 gives all these data on a single plot. The strain range available is from about 10^{-3} to 10^{-8}.

With a single exception, the trend of this collection of data is for a decrease in attenuation with decreasing peak strains. The Salmon, higher strain Cowboy and small scale explosion data give Q's of the order ten. The Cowboy and Sterling data suggest that Q's are well over one hundred by strains of 10^{-5}. The resonant bar results (which seem to consistently show lower attenuation than other experiments) have Q's of several hundred but show an increase as strains approach 10^{-5}. The New England Research ultrasonic pulse experiments are the exception as they give a Q independent of strain. However, these experiments were carried out with no confinement.

Furthermore, recent work on other media [K. Coyner, private communication] suggests that this experimental technique may be strongly influenced by scattering from normally existing inhomogeneities in the samples. This scattering from structure comparable with the ultrasonic wavelength may depend strongly on frequency so the attenuation results would not be relevant to the lower frequency pulse propagation problem.

Taken as a whole, the salt data indicate that attenuation is strong and nonlinear for strains greater that 10^{-5}. For smaller strains the attenuation appears to become small and linear. The peak strain of 10^{-5} occurs at a scaled range of approximately 3 km/kt$^{1/3}$. Murphy [1978] indicates that an elastic radius for salt is less than 500 m/kt$^{1/3}$ based on analysis of stabilization of RDP's of nuclear explosions. This contrasts with the fact that other measurements quoted in the current article indicate that the effective Q is less than 10 and apparently nonlinear. When a source function is defined at this small radius the subsequent propagation out to sufficiently large ranges, where the totality of the data indicates the behavior is linear, will have an effect which is not currently understood.

There are no completely satisfactory descriptions of the nonlinear behavior of salt in the moderate strain regime. Without a physical constitutive relation, it is difficult to remove the uncertainty in the effective seismic source function. There are two conjectures which have been put forth to account for Salmon data.

Rimer and Cherry [1983] have noted that a reasonable fit to the Salmon data, including attenuation and precursor, can be obtained by use of a constitutive relation combining a limiting yield strength with quadratic work hardening and softening. Cherry and Rimer [1980] find that the same parameters also provide a reasonable description of other salt data. The work hardening model provides a variable yield strength Y which is given by

$$Y = Y_0 (1 + e_1 E - e_2 E^2) < Y_{Lim} \qquad (3)$$

There are only three free parameters since the limiting yield strength, Y_{Lim}, is constrained by other experiments. In this model the initial yield strength, Y_0, is rather low. The harding and softening parameters e_1 and e_2 as well as Y_0 are used to fit the data. The yield strength initially increases as inelastic energy, E, is absorbed by the shear failure in a manner quadratic in this inelastic energy. The yield strength is a measure of the maximum potential energy which can be held in shear in the medium. When addition shear stress is applied to a medium at its yield limit, the work goes into inelastic energy which then is taken to alter the yield limit in this model. As indicted by Figure 14, there are some experimental data to suggest that work hardening and yielding in salt does occur [Boresi and Deere,1963]. However, Glenn [1989] has noted that while the Salmon data can be largely accounted for by a constitutive model for which the salt first hardens and then softens greatly, the required parameters are inconsistent with independently measured material properties.

McCartor and Wortman [1988,1990] have proposed another nonlinear model for partial shear failure which is designed to account for the Salmon attenuation and precursor. In this model the Lamé shear modulus, μ, is permanently and instantly reduced by 80% in any material element once the compressional strain level exceeds 10^{-4}. The other Lamé modulus, λ, is held fixed. This has the effect of reducing the compressional speed (which is proportional to $(\lambda +2\mu)^{1/2}$) of the main part of the pulse by about 20% relative to the elastic speed seen in the precursor. In addition to producing a precursor which propagates at the observed speed, this also produces attenuation due to the loss of shear energy which is proportional to m, giving an effective Q of about 13 for peak strains well in excess of 10^{-4}. Note that for small strains below this threshold there will be no loss. This value of Q is much less than that expected for very small strains but it is still more than the 5 to 10 seen for Salmon attenuation. It will produce a sharply changing effective Q at a threshold strain in the manner suggested by the Cowboy data. Furthermore, since the partial shear failure threshold is a function of the strain level only, the resulting constitutive model will preserve cube root scaling. McCartor and Wortman [1990] find that this mechanism is not adequate to account for all aspects of the waveform unless some addition linear attenuation is added. Still their calculations, and the model of Rimer and Cherry [1983] (which also is consistent with cube root scaling), strongly suggest that shear failure plays a strong role in the nonlinear behavior of salt at moderate strains. While these models hint at the character which is required for a robust constitutive relation for salt at moderate strains, the issue is clearly not resolved.

References

Bonner, B., B. J. Wanamaker and S. R. Taylor, Amplitude-dependent attenuation and implications for the seismic source, in Proceedings of the DOE/LLNL Symposium on Explosion-Source Phenomenology, (Conference) CONF-890398, Lawrence Livermore National Laboratory, Livermore, Calif., 1989.

Boresi, A. P. and D. U. Deere, Creep closure of a spherical cavity in an infinite medium, Rep. Unnumbered, Holmes&Narver, Inc., Las Vegas Division, Las Vegas, Nev., 1963.

Cherry, J. T. and N. Rimer, A constitutive model for salt, Rep. SSS-R-81-4725, Systems, Science and Software, La Jolla, Calif., 1980.

Coyner, K. B., Attenuation measurements on dry Sierra white granite, dome salt and Berea sandstone, Rep. NER Contract 9092405, New England Research, Inc., Norwich, Vt., 1987.

Denny, M. D., A case study of the seismic source function: Salmon and Sterling reevaluated, J. Geophys. Res. 95, 19705, 1990.

Eisler, J. D. and H. V. Hoffman, Free-field particle motion from a nuclear explosion in salt, Part II, Project Dribble, Salmon Event, Rep. VUF-3013, Stanford Research Institute, Menlo Park, Calif., 1966.

Evernden, J. , C. Archambeau, and E. Cranswick, An evaluation of seismic decoupling and underground nuclear test monitoring using high-frequency seismic data, Rev. Geophys. 24, 143, 1986.

Glenn, L. A., M. D. Denny and J. A. Rial, Sterling revisited: The seismic source for a cavity-decoupled explosion, Geophys. Res. Letters 14, 1103, 1987.

Glenn, L. A, Anomalies in the results of the Salmon experiment, in Proceedings of the DOE/LLNL Symposium on Explosion-Source Phenomenology, (Conference)CONF-890398, Lawrence Livermore National Laboratory, Livermore, Calif., 1989.

Gupta, I. N. and K .L. McLaughlin, Strain and frequency dependent attenuation estimates in salt from Salmon and Sterling near-field recordings, Bull. Seis. Soc. Am. 79, 1111,1989.

Langston, C. A., Kinematic analysis of strong motion P and SV waves from the Sterling event, J. Geophys. Res. 88, 3486,1983.

Larson, D. B., Inelastic wave propagation in sodium chloride, Bull. Seis. Soc. Am. 72, 2107 (1982).

Larson, D. B., Source and material modeling project: Experimental facilities and wave propagation results, in Seismic Coupling of Nuclear Explosions, D. B. Larson, editor, Rep. UCRL-21086, Vol 1, Defense Advanced Research Projects Agency, Arlington, Va., 1989.

McCartor, G. D. and W. R. Wortman, Experimental and analytic characterization of nonlinear seismic attenuation, Rep. MRC-R-900, Mission Research Corp., Santa Barbara, Calif., 1985.

McCartor, G. D. and W. R. Wortman, Nonlinear attenuation mechanisms in salt at moderate strain based on Salmon data, Rep. AFGL-TR-89-0013, ADA207540, Mission Research Corp., Santa Barbara, Calif., 1988.

McCartor, G. D. and W. R. Wortman, Analysis of Salmon near-field data for nonlinear attenuation, J. Geophys. Res. 95, 21805, 1990.

Minster, J. B. and S. M. Day, Decay of wave fields near an explosive source due to high-strain nonlinear attenuation, J. Geophys. Res. 91, 2113, 1986.

Murphey, B. F., Particle motions near explosions in halite, J. Geophys. Res. 66, 947, 1961.

Murphy, J. R., A review of available free-field seismic data from underground nuclear explosions in salt and granite, Rep. CSC-TR-78-0003, Computer Sciences Corp., Falls Church, Va.,1978.

Perret, W. R., Free-field particle motion from a nuclear explosion in salt, Part I, Project Dribble, Salmon Event, Rep. VUF-3012, Sandia Laboratory, Albuquerque, N.M., 1967.

Rimer, N. and J. T. Cherry, Ground motion predictions for the Grand Saline experiment, Rep. USC-TR-83-25, S-Cubed Corp., La Jolla, Calif., 1982.

Rogers, L. A., Free-field motion near a nuclear explosion in salt: Project Salmon, J. Geophys. Res. 71, 3415, 1966.

Sisemore, C. J., L. A. Rogers and W. R. Perret, Project Sterling: Subsurface phenomenology measurements near a decoupled nuclear event, J. Geophys. Res. 74, 6623, 1969.

Springer, D., M. Denny, J. Healy and W. Mickey, The Sterling experiment: Decoupling of seismic waves by a shot-generated cavity, J. Geophys. Res. 73, 5995, 1968.

Tittmann, B. R., Non-linear wave propagation study, Rep. SC5361.3SAR, Rockwell

International Science Center, Thousand Oaks, Calif., 1983.

Trulio, J., *Simple scaling and nuclear monitoring*, Rep. ATR-78-45-1, Applied Theory, Inc., Los Angeles, Calif., 1978.

Weart, W. D., Particle motion near a nuclear detonation in halite, *Bull. Seis. Soc. Am.* 54, 981, 1962.

Workman, J. W. and J. G. Trulio, *Cowboy Trails: Analysis of gauge records for peak velocity and wavespeed*, Rep. PAI-FR-0119-2, Physics Applications, Inc., Los Angeles, Calif., 1985.

Wortman, W. R. and G. D. McCartor, Nonlinear seismic attenuation from Cowboy and other explosive sources, in *Seismic Coupling of Nuclear Explosions*, D. B. Larson, editor, Rep. UCRL-21086, Vol 2, Defense Advanced Research Projects Agency, Arlington, Va., 1989.
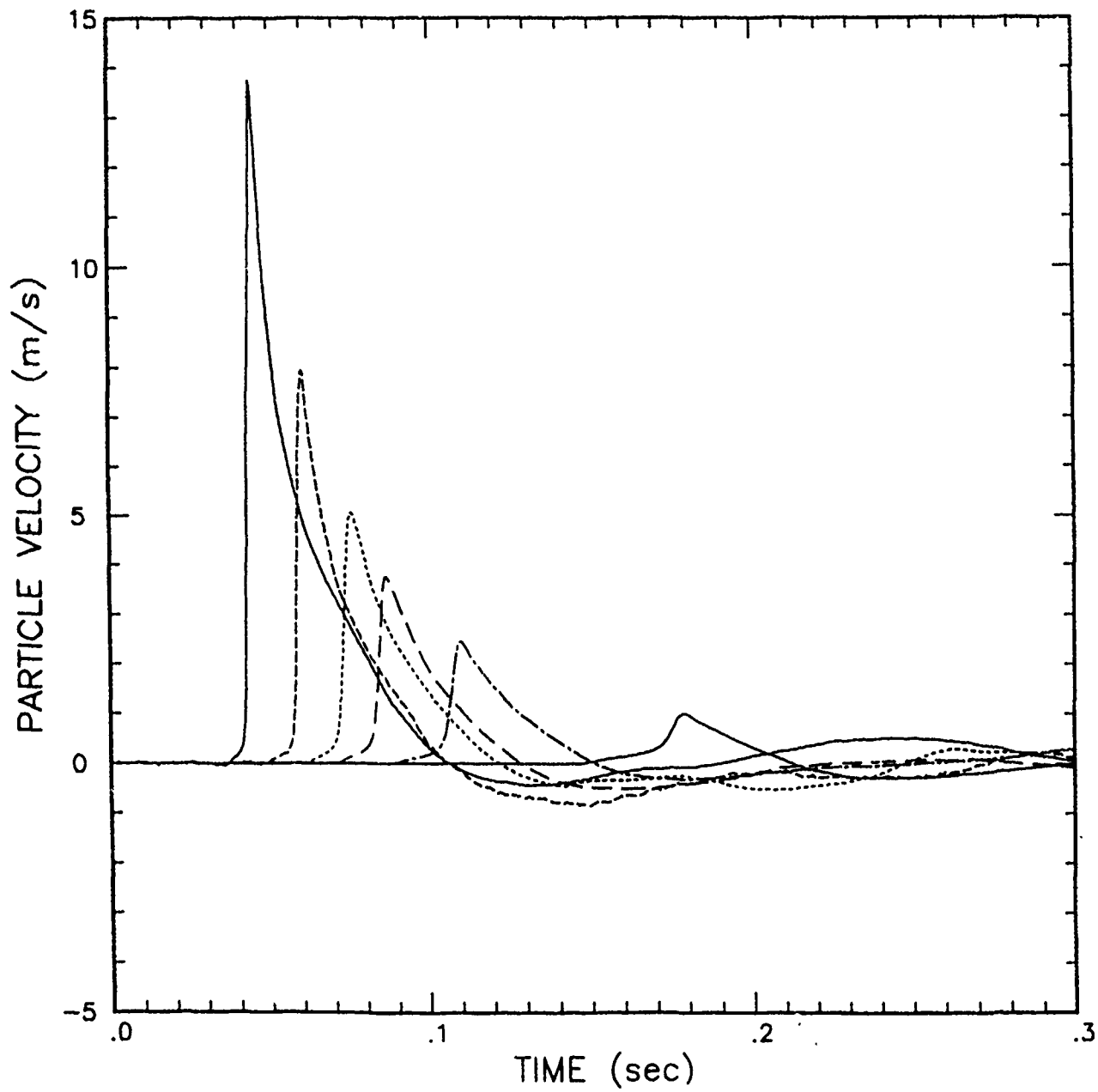
Fig. 1. Salmon particle velocity records at 166, 225, 276, 318, 402 and 660 m, in that order from left to right [McCartor and Wortman, 1989].
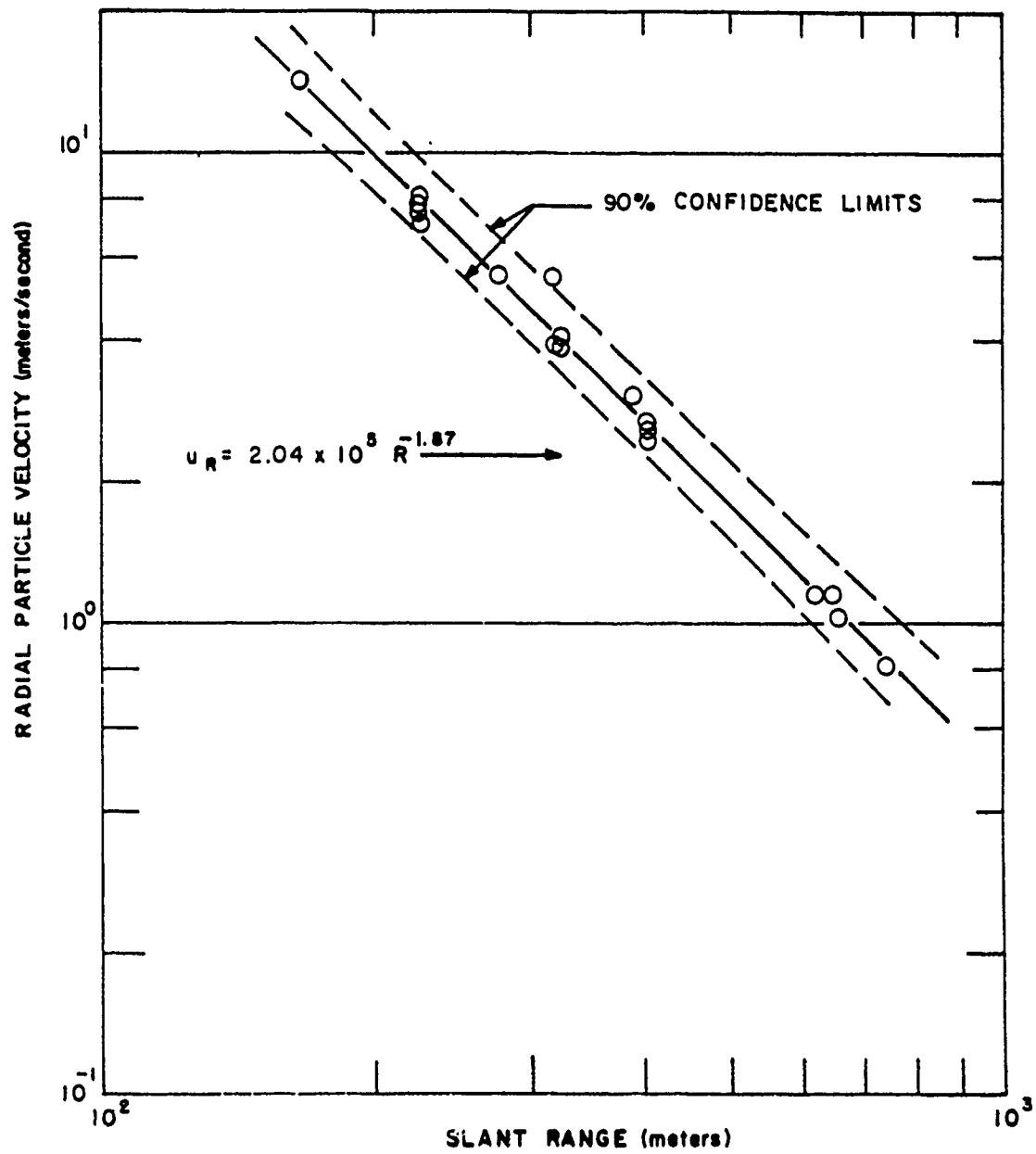
Fig. 2. Perret's [1967] Salmon peak radial particle velocities versus range from 18 sensors.
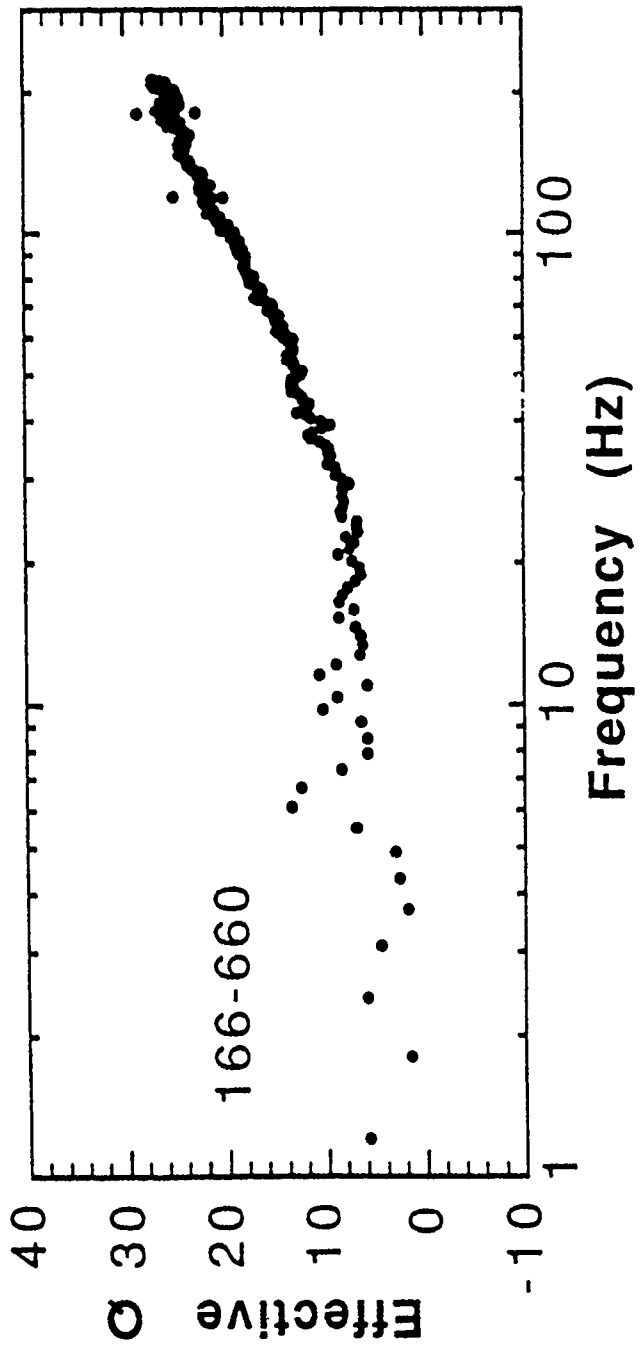
Fig. 3. Salmon Q estimated from the 166 and 660 m sensor pair [McCartor and Wortman, 1989].
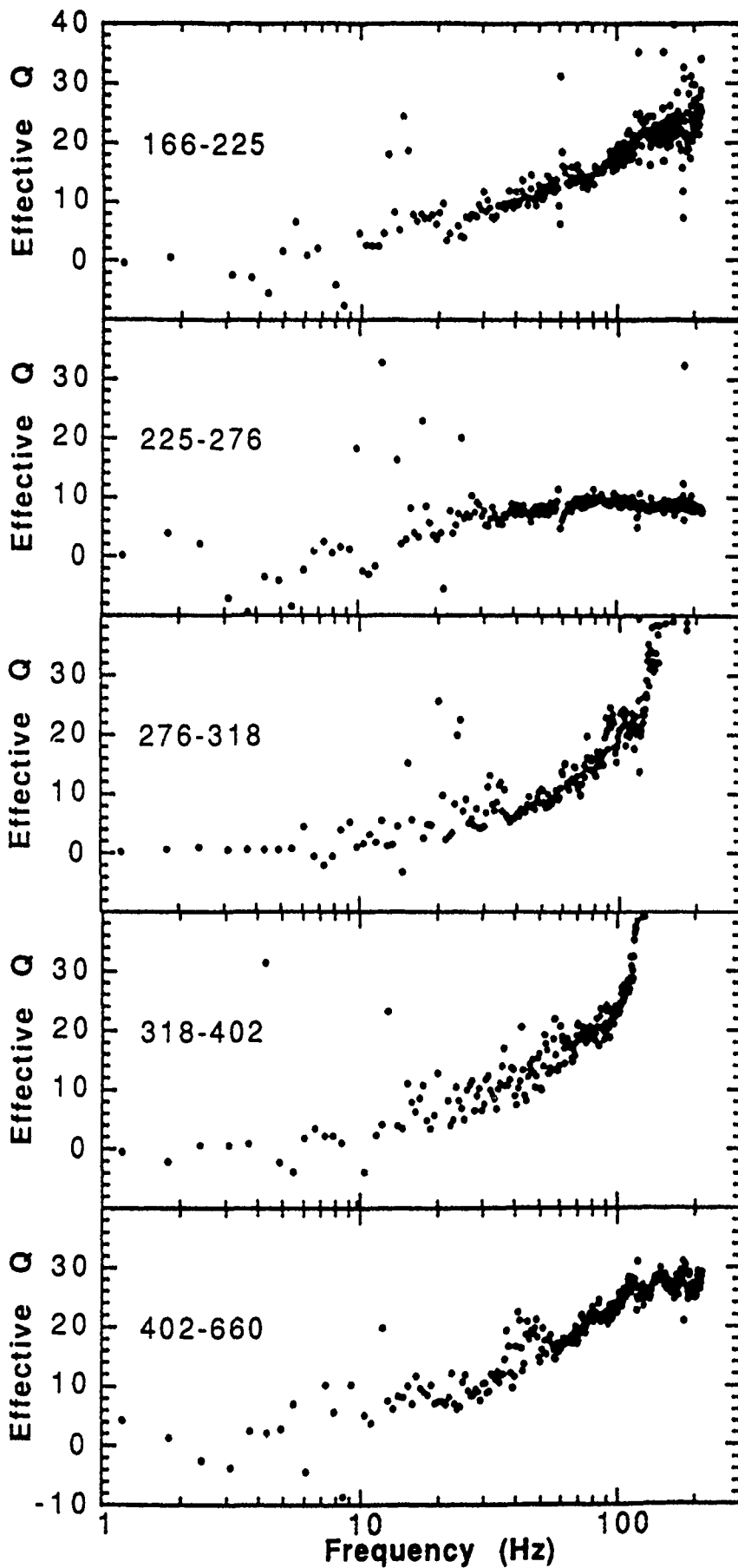
Fig. 4. Salmon Q's estimated from adjacent sensor pairs between 166 and 660 m
[McCartor and Wortman, 1989].
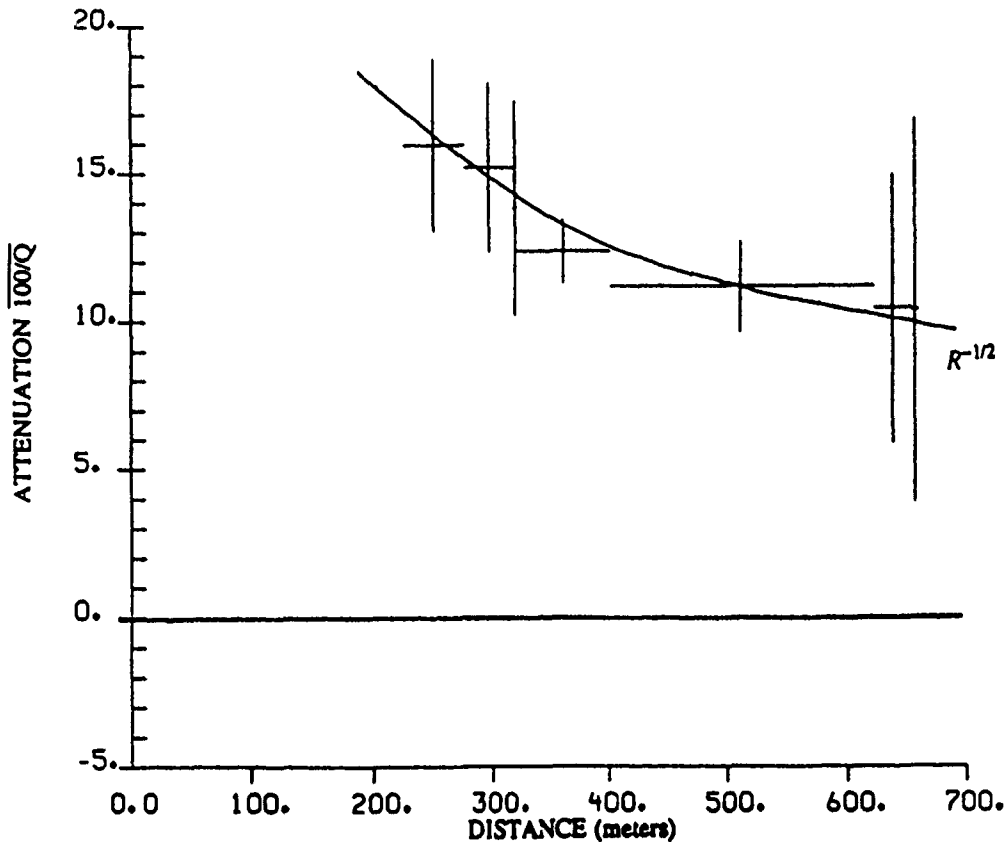
Fig. 5. Salmon Q estimates with range [Gupta and McLaughlin, 1989]. Vertical bars show a standard deviation. Horizontal bars indicate the separation of the sensors used for that estimate.
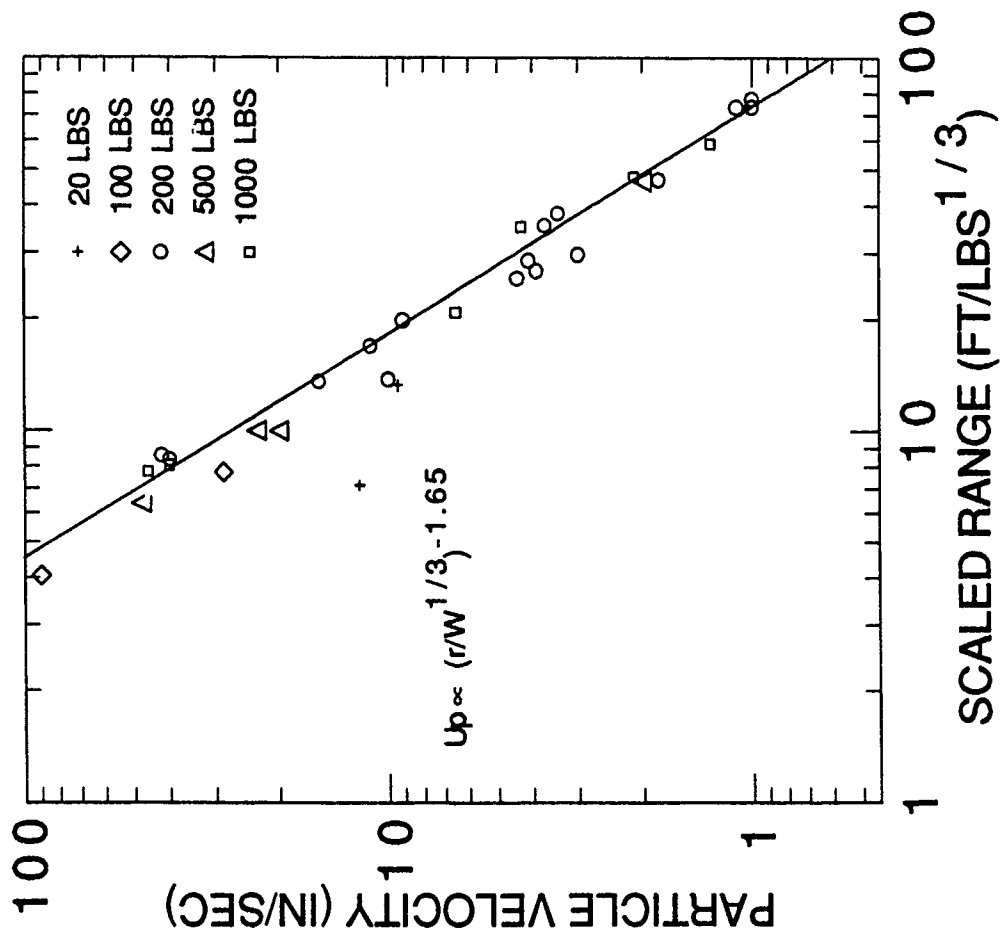
Fig. 6. Cowboy peak particle velocity data versus scaled range [Murphey,1961].

117
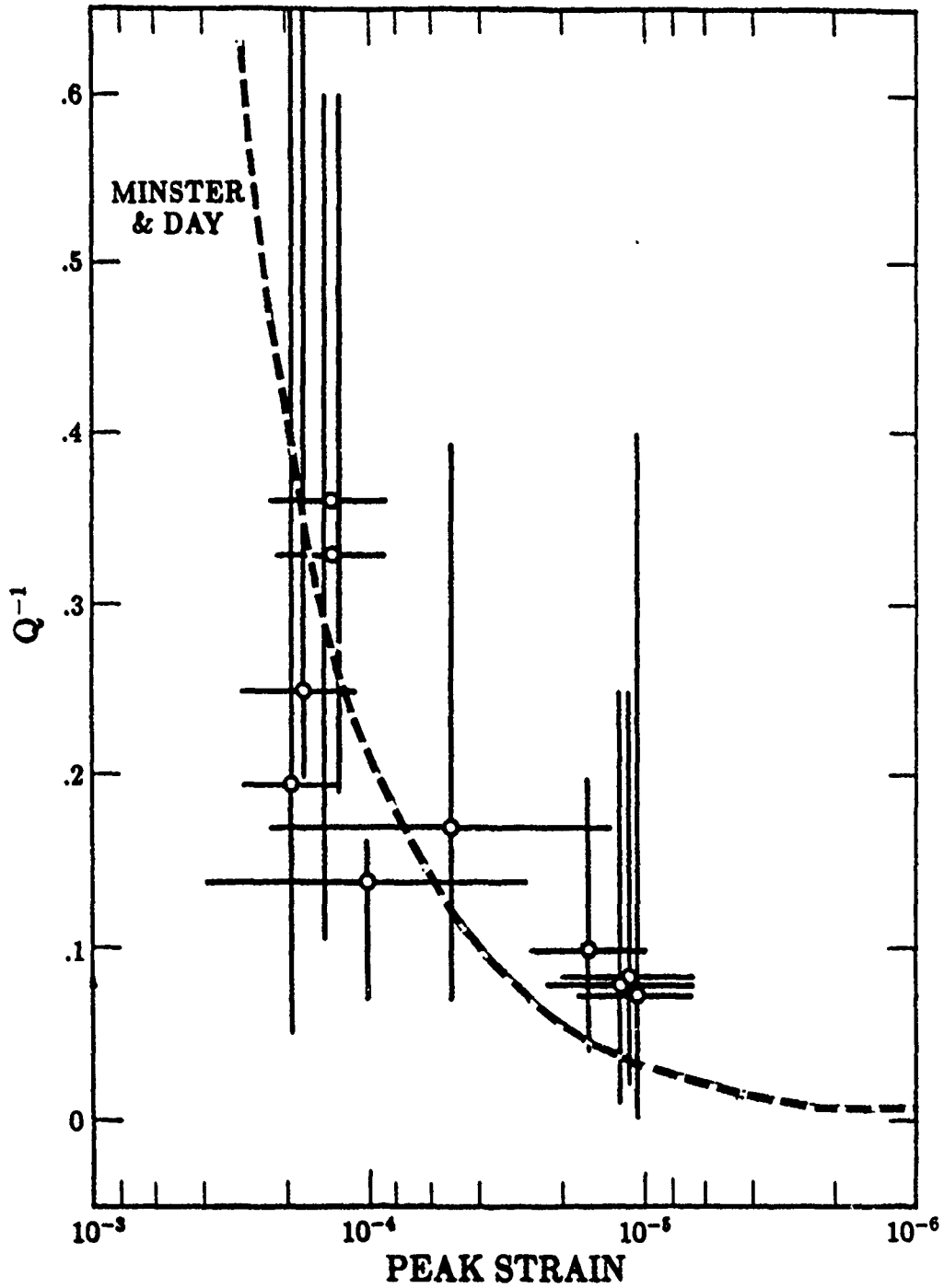
Fig. 7. Cowboy Q estimates with range from Wortman and McCartor [1989] and Minster and Day [1986]. Vertical bars show the variation of Q over an order of magnitude in frequency about the dominant frequency. Horizontal bars indicate the separation of the sensors used.

118
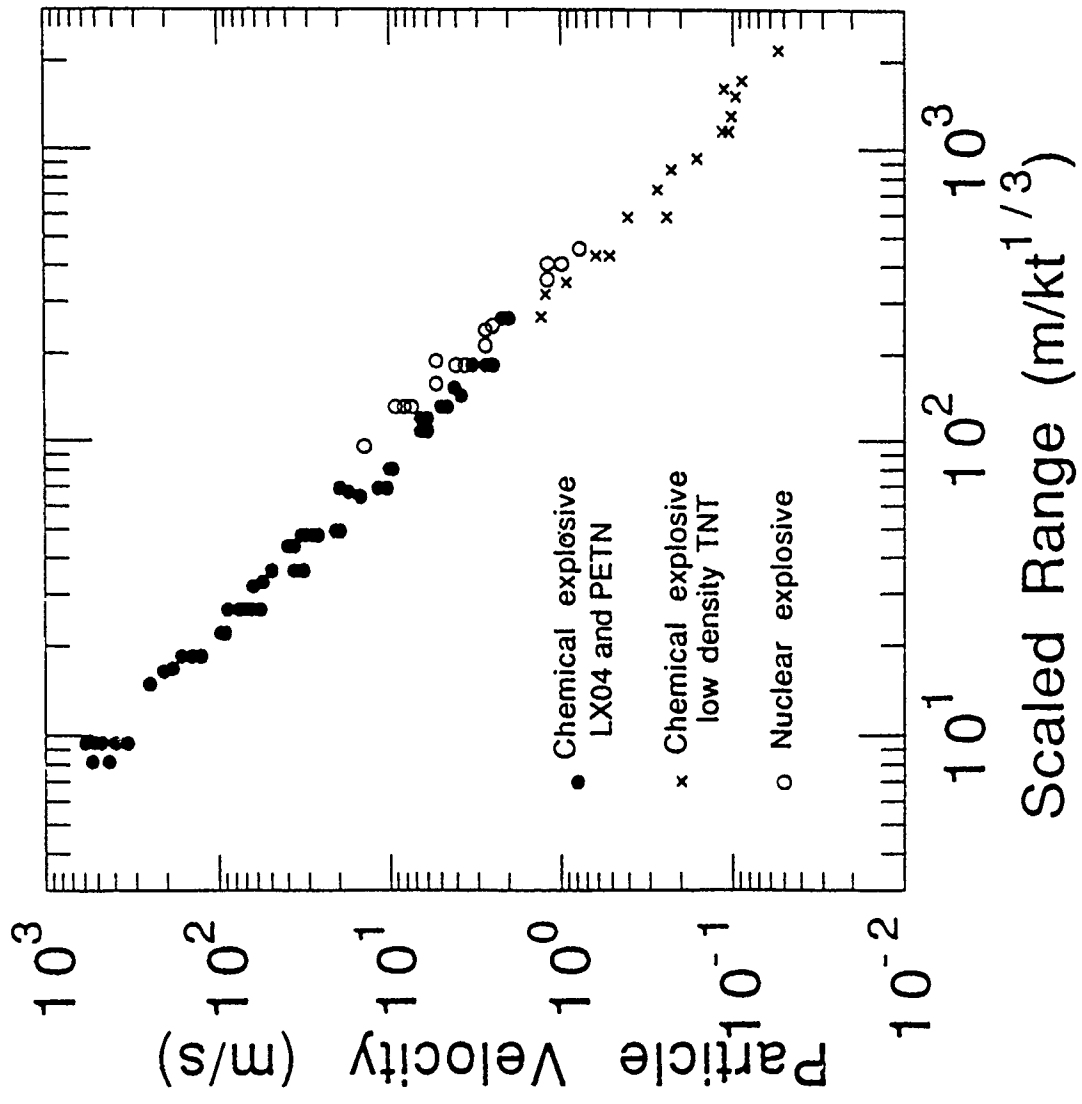
Fig. 8. Salt peak particle velocity data versus scaled range [Larson, 1982].
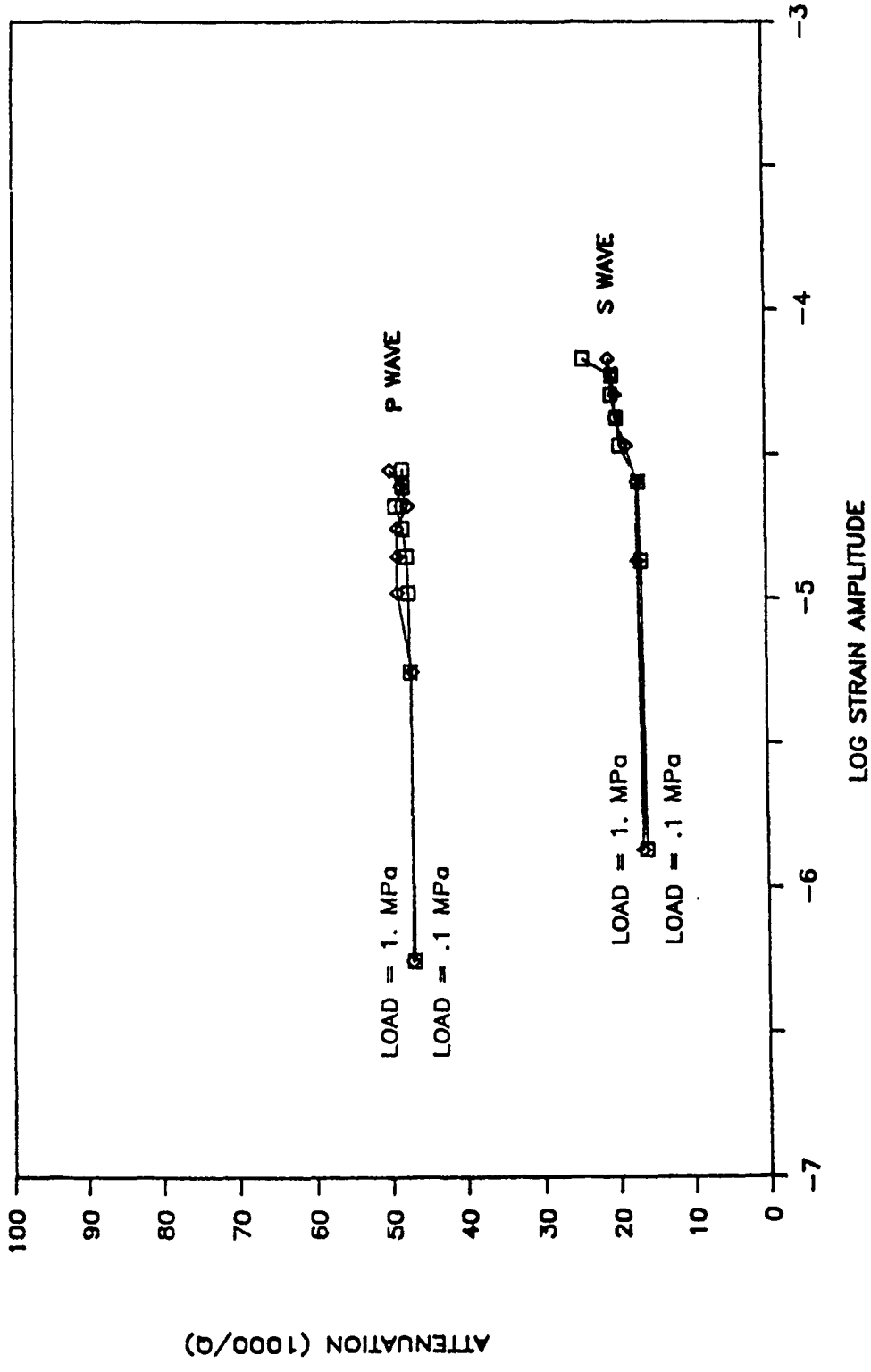
Fig. 9. Q in salt for P and S wave ultrasonic pulse experiments [Coyner, 1987].

120
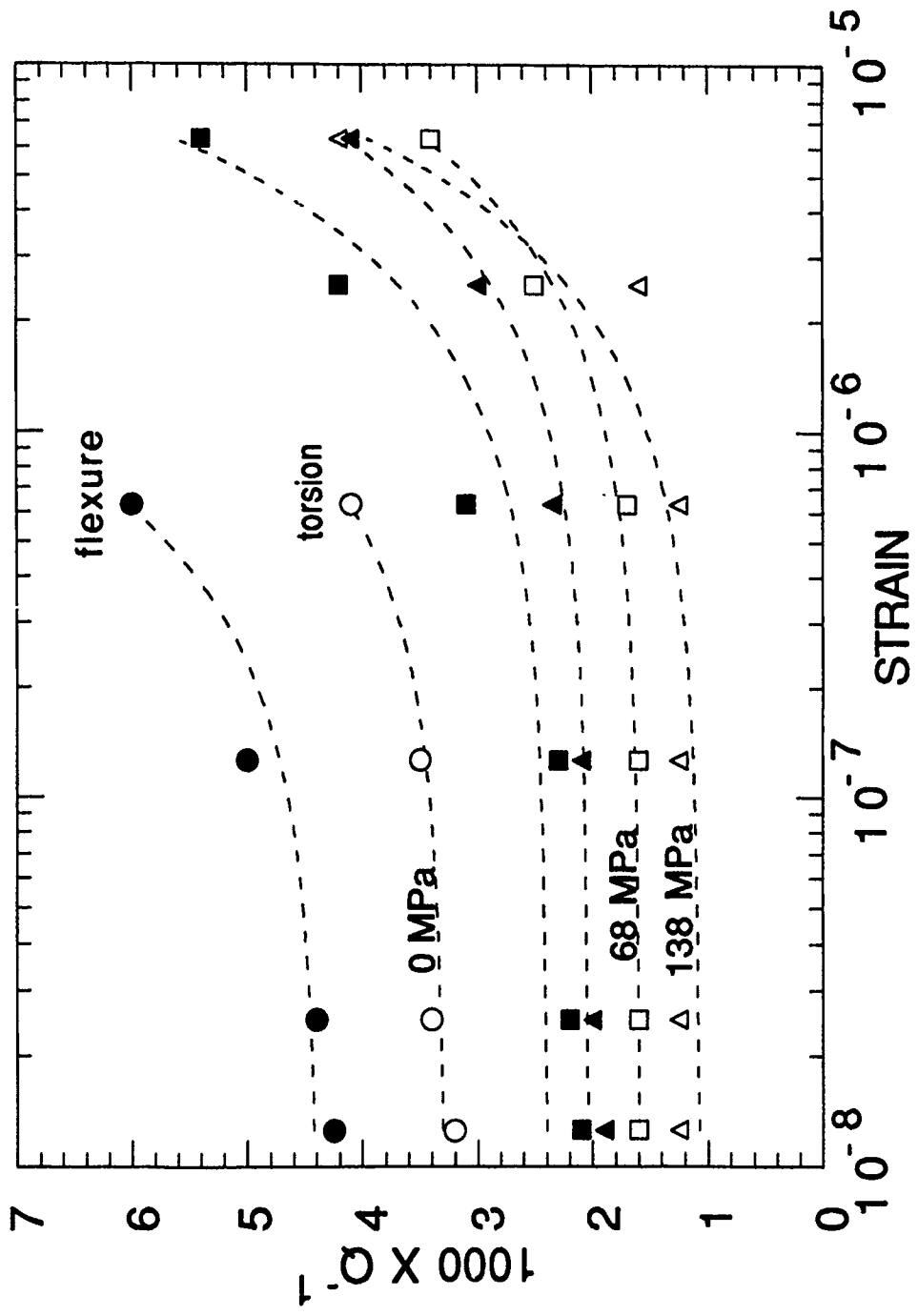
Fig. 10. Resonant bar Q estimates versus strain for three pressures for both flexure (solid) and torsion (open) [Tittmann, 1983].
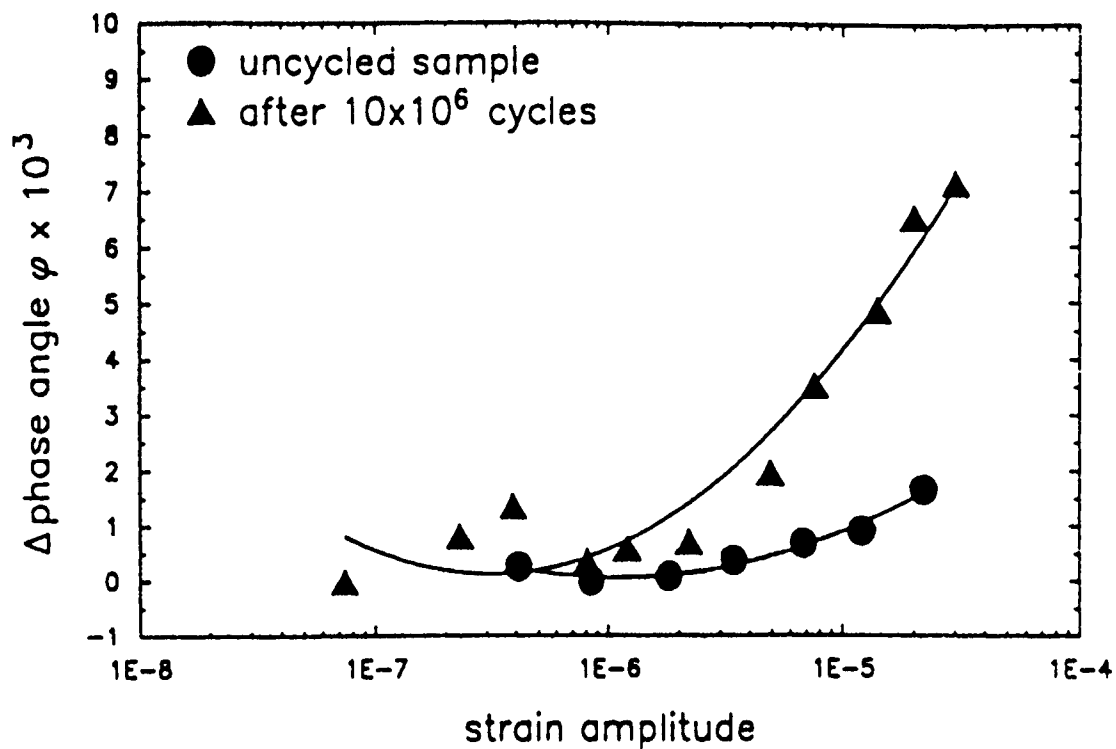
121

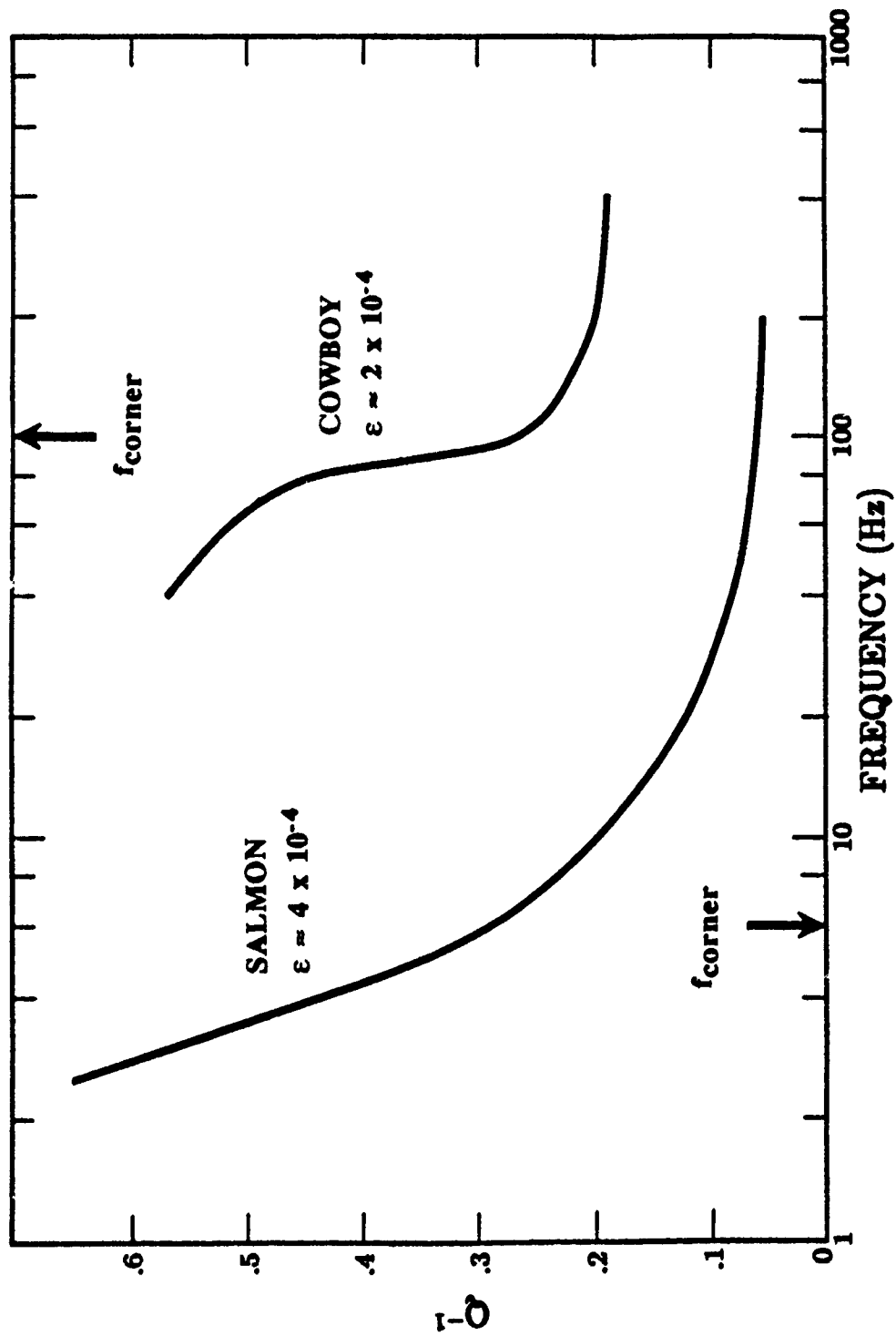Fig. 11. Variation of attenuation with strain for cycling in Sierra white granite [Bonner et al.,1989].

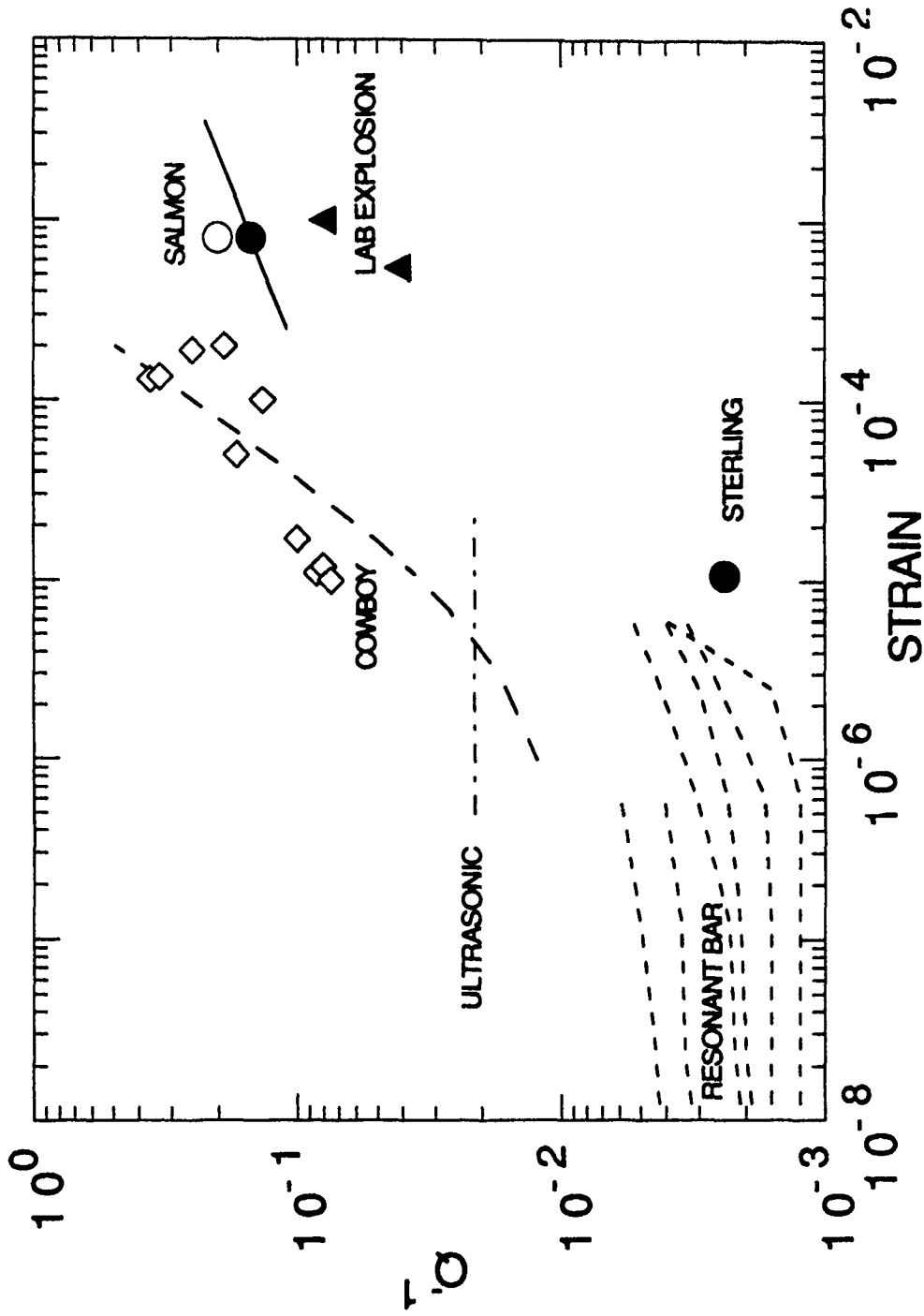Fig. 12. Unscaled Salmon and Cowboy Q estimates as a function of frequency [Wortman and McCartor, 1989].

Fig. 13. All available salt attenuation data as a function of peak strain, taken at the dominant frequencies of the various experiments including Salmon (O McCartor and Wortman [1985], • Gupta and McLaughlin [1989]), Sterling (• Gupta and McLaughlin [1989]), Cowboy (◇ Wortman and McCartor [1989] and – – – Minster and Day [1986]), ultrasonic pulse (·–· Coyner [1987]) and resonant bar (·–·– Tittmann [1983]). See Fig. 10 for resonant bar parameters.
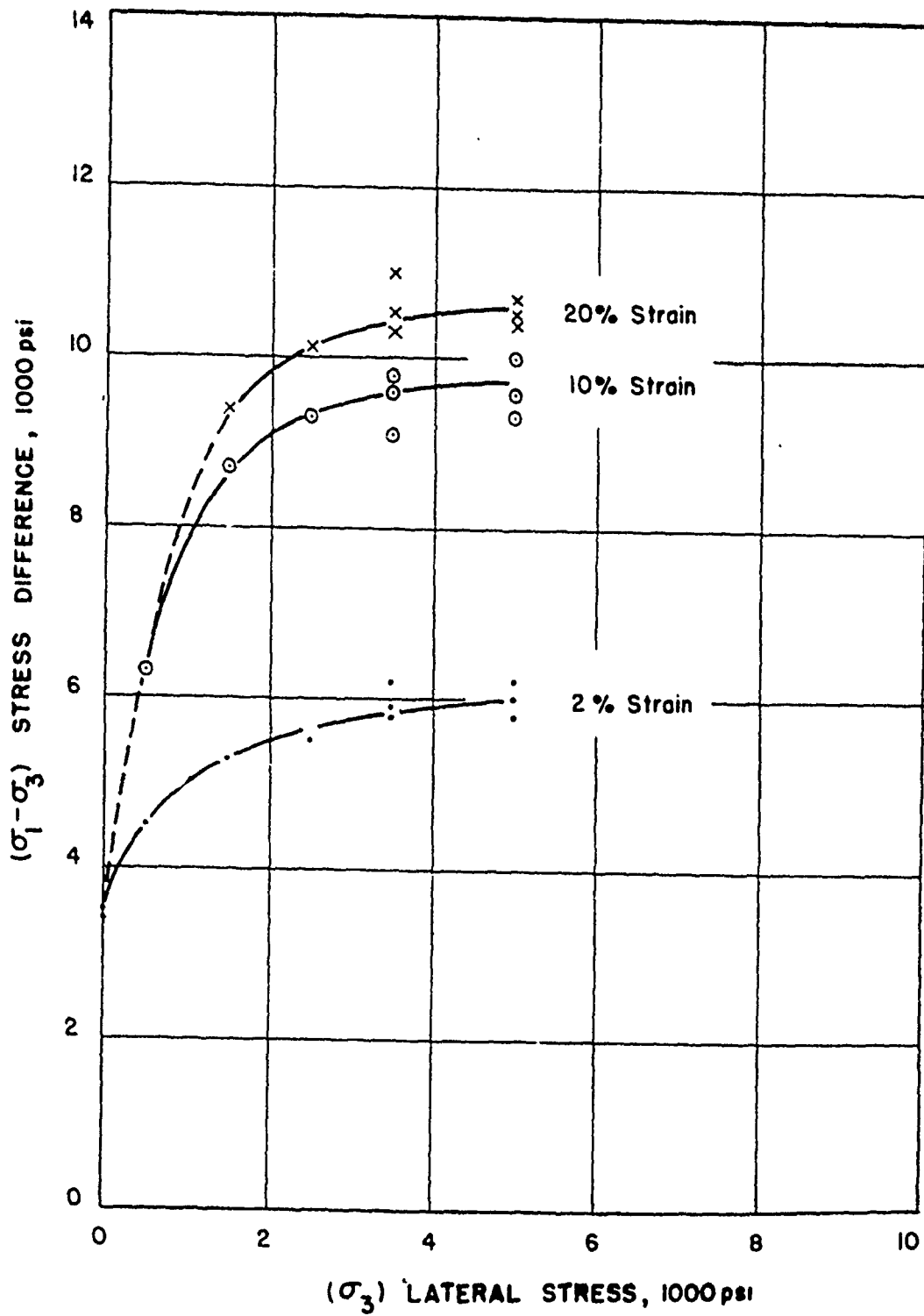
Fig. 14. Yield strength as a function of lateral stress for dome salt at three strain levels [Boresi and Deere, 1963].